Connecting structure and dynamics to rheological performance of complex fluids

by

Abhishek M. Shetty

A dissertation submitted in partial fulfillment
of the requirements for the degree of
Doctor of Philosophy
(Chemical Engineering)
in The University of Michigan
2010

Doctoral Committee:

Professor Michael J. Solomon, Chair
Professor Mark A. Burns
Professor Ronald G. Larson
Assistant Professor Anish Tuteja

2010

Dedication

This dissertation is dedicated to my parents for their unconditional support and innumerable sacrifices.

Table of Contents

Dedication ..... **ii**

List of Figures ..... **vi**

List of Tables ..... **x**

Abstract ..... **xi**

CHAPTER 1 INTRODUCTION **1**

1.1 Complex Fluids 1

1.2 Dynamic Light Scattering 7

1.3 Confocal laser scanning microscopy 9

1.4 Outline of the dissertation 10

1.5 References 13

CHAPTER 2 AGGREGATION IN DILUTE SOLUTIONS OF HIGH MOLAR MASS POLY(ETHYLENE) OXIDE AND ITS EFFECT ON TURBULENT DRAG REDUCTION **17**

2.1 Chapter Summary 17

2.2 Introduction 19

2.3 Experimental Section 24

2.3.1 Materials: 24

2.3.2 Dynamic Light Scattering (DLS) 24

2.3.3 Turbulent drag reduction characterization 26

2.4 Results 28

2.4.1 DLS of dilute aqueous solutions of PEO 28

2.4.2 Manipulation of PEO aggregate structure with addition of salt. 31
2.4.3 Effect of aggregate structure on turbulent drag reduction. 33
2.5 Discussion 36
2.6 Conclusions 41
2.7 References 59

CHAPTER 3 MULTI-ANGLE DEPOLARIZED DYNAMIC LIGHT SCATTERING OF SHORT FUNCTIONALIZED SINGLE-WALLED CARBON NANOTUBES 63

3.1 Chapter Summary 63
3.2 Introduction 64
3.3 Materials and Methods. 66
3.3.1 Materials 66
3.3.2 Depolarized Dynamic Light Scattering of Carbon Nanotubes: Modeling and Experiment 67
3.3.3 Atomic Force Microscopy 70
3.4 Experimental Section. 71
3.4.1 DDLS of dilute functionalized SWNT samples. 71
3.4.2 Atomic force microscopy. 74
3.5 Conclusion 76
3.6 References 84

CHAPTER 4 DIRECT VISUALIZATION OF GLASSY DYNAMICS IN A MODEL POLAYMAIDE ROD SYSTEM 88

4.1 Chapter Summary 88

4.2 Introduction 90
4.3 Experimental Section 92
4.3.1 Materials 92
4.3.2 Methods 93
4.3.2.1 Sample preparation 93
4.3.2.2 Confocal laser scanning microscopy (CLSM) 93
4.3.2.3 Image analysis 93
4.3.2.4 Rheology 95
4.4 Results 96
4.4.1 Arrested dynamics by CLSM and Image correlation analysis 96
4.4.2 Rheological Characterization 98
4.5 Discussion 100
4.6 Conclusion 104
4.7 References 114
CHAPTER 5 CONCLUSIONS AND FUTURE WORK 118
5.1 Conclusions 118
5.2 Future Work 120
5.3 References 123

List of Figures

Figure 1.1: Definition of scattering vector, q and geometry of our dynamic light scattering setup. 11

Figure 1.2: Schematic of the Leica SP2 TCS Confocal laser scanning microscope[52] 12

Figure 2.1: Quiescent rheological characterization of aqueous PEO WSR-301 ($M_w \sim 4 \times 10^6$ g/mole) at $T=25^0$ C in a 2^0 60 mm cone and plate geometry. The viscosity, η, is plotted for a series of PEO concentrations (500-8000 ppm) as a function of shear rate, $\dot{\gamma}$. The dashed curves are best fits to the data for the FENE-P constitutive equation with $\eta_s = 0.001$ Pa-sec and $L^2=1000$. 43

Figure 2.2: Concentration dependence of the viscoelastic relaxation time (ms) of WSR-301 from FENE-P curve fits for the experimental data from Fig. 2.1 at various concentrations. The horizontal line is the dilute solution prediction by Zimm theory. 44

Figure 2.3: Intensity autocorrelation function $g_2(\tau)$ for 20 ppm ($c/c^* \sim 0.03$) PEO WSR-301 as a function of scattering angle, q. 45

Figure 2.4: Probability distribution function of the DLS decay time spectrum for 20 ppm PEO WSR-301, obtained from CONTIN deconvolution of $g_2(\tau)$ reported in Fig. 2.3. 46

Figure 2.5: Prandtl-von Karman plots for different PEO WSR-301 concentrations ranging from 1-25 ppm. As discussed in the text, the lower curve is the Prandtl-Karman (PK) law for a Newtonian solvent and the upper curve is the maximum drag reduction asymptote for polymer turbulent drag reduction. 47

Figure 2.6: Peak relaxation rate, Γ, from CONTIN deconvolution as a function of the scattering vector q for different dilute concentrations (5-50 ppm) of PEO WSR-301. 48

Figure 2.7: Peak relaxation rate, Γ, from CONTIN deconvolution as a function of the scattering vector q for different dilute concentrations (15-150ppm) of monodisperse PEO-1182K ($M_w \sim 1.2 \times 10^6$ g/mole, $M_w/M_n \sim 1.12$). 49

Figure 2.8: The effect of $MgSO_4$ concentration on the q-dependence of the peak relaxation rate Γ at 5 ppm for PEO WSR-301. 50

Figure 2.9: Comparison of the DLS decay time spectrum for 150 ppm monodispersed PEO-1182K (M_w ~ 1.2 x 10^6 g/mole, M_w/M_n~1.12) in deionized water (aqueous) and with guanidine sulfate salt (0.85M GuS) at different scattering angles. 51

Figure 2.10: Peak decay relaxation rate, Γ, as a function of q for the deionized water (aqueous) and guanidine sulfate salt (0.85M GuS) case (150 ppm monodisperse PEO-1182K). 52

Figure 2.11: Effect of guanidine sulfate salt (GuS) concentration and 1M magnesium sulfate ($MgSO_4$) on the q-dependence of Γ for monodisperse aqueous PEO-1182K (150 ppm). 53

Figure 2.12: Effect of magnesium sulfate (0.5M $MgSO_4$) addition on the turbulent drag reduction behavior of dilute PEO WSR-301 solutions. 54

Figure 2.13: Comparison of the onset wall shear stress for turbulent drag reduction, τ_w*, for WSR 301 with 0.5 M $MgSO_4$ and in pure aqueous solution. The horizontal line is the onset stress prediction given by Virk for PEO, based on single molecule physics, computed as discussed in the text. 55

Figure 2.14: Summary of DLS results, plotted as Γ/q^2 to emphasize the deviation from center-of-mass diffusion, for the two polymers and salts studied. The curve is the theoretical prediction for a Gaussian coil[52]. 56

Figure 2.15: Schematic illustration of the hypothesis that small scattering angle DLS measurements of PEO would yield a characterization of the size of the aggregates observed in this study. 57

Figure 3.1: Comparison of the polarized (VV) and depolarized (VH) intensity autocorrelation functions $g_2(\tau)$ of SWCNT-PABS in the concentration range c=0.01-0.1 mg/ml at scattering angle, θ=45°. The inset plot shows the probability distribution function of the DLS decay time spectrum in the VV and VH scattering planes for the above concentrations, obtained from a CONTIN deconvolution of $g_2(\tau)$. 77

Figure 3.2: Comparison of the DLS decay time spectrum of c=0.01 mg/ml of SWCNT-PABS in deionized water (aqueous) and with magnesium chloride salt (5mM $MgCl_2$) at θ=45° as a function of time. 78

Figure 3.3: Peak decay relaxation time, τ, as a function of time of c=0.01 mg/ml of SWCNT-PABS in deionized water (aqueous) and with magnesium chloride salt (5mM $MgCl_2$) at θ=45. 79

Figure 3.4: Comparison of the polarized (VV) and depolarized (VH) intensity autocorrelation functions $g_2(\tau)$ of SWCNT-PABS at c=0.01 mg/ml and at different scattering angles. The inset plot shows the probability distribution function, obtained from a CONTIN deconvolution of the measured VV and VH autocorrelation functions at different scattering angles..... 80

Figure 3.5: Γ Vs q^2 plot of SWCNT-PABS and SWCNT-PEG at c=0.01 mg/ml obtained from VV and VH scattering. Error bars reported are standard error of the mean..... 81

Figure 3.6: AFM micrographs for thin films of dried SWCNTs dispersions. Fig. a) corresponds to PEG functionalized SWCNTs and Fig. b) corresponds to PABS functionalized SWCNTs. We found that theSWCNT-PABS were more stable than the SWCNT-PEG. Dried films of suspensions of PEG-SWCNTs were prone to aggregation as can be seen in Fig. a). The scale bar is 1 μms. Fig. c) and d) show the distribution of CNT lengths for SWCNT-PEG and SWCNT-PABS respectively. Similarly, Fig. e) and f) correspond to the distribution of CNT diameters for SWCNT-PEG and SWCNT-PABS respectively..... 82

Figure 4.1: Representative 2D confocal micrographs of a rod suspension as a function of increasing rod volume fraction, ϕ, for a rod suspension with aspect ration, r = 212. (a) ϕ=0.0005, (b) ϕ=0.001, (c) ϕ=0.0025, (d) ϕ=0.005, (e) ϕ=0.01(f) ϕ=0.03. 105

Figure 4.2: Change of Correlation coefficient, R with volume fraction, ϕ as a function of increasing time intervals between images for a rod suspension with aspect ratio, r =212. 106

Figure 4.3: Plot of onset volume fraction Vs aspect ratio that compares our experimental values with existing rod theory predictions. The solid square symbols are the arrest volume fractions obtained via confocal microscopy and image processing. The top two dashed lines are the ideal glass transition volume fractions for spherocylinders and tangent bead rods obtained from NMCT theory. The dashed upper line is a prediction by Philipse et al., for an arrest volume fraction where one first sees arrest in a rod suspension due to no sideways translation movement possible. The lower solid line is the minimum percolation volume fraction of random homogenous rod network. The dashed lower line is the Edwards and Evans prediction for an arrest volume fraction for a highly

entangled rod system where rotational diffusion of rods is seriously constrained. Error bars in this figure are less than the size of the datum points.....107

Figure 4.4: Elastic (G') and Viscous moduli (G") as a function of percent strain at an angular frequency of 6.28Hz. 108

Figure 4.5: Elastic modulus obtained from the plateau region of G' Vs % strain curves (as shown in Fig. 4.4) plotted as a function of effective volume fraction, (ϕ-ϕ_g).....109

Figure 4.6: Volume fraction dependence of yield strain for the different aspect ratios studied.....110

Figure 4.7: Total interaction potential, $U_{Tot}(r)/k_BT$ between two parallel polyamide rods plotted as a function of interaxial distance between the rods. The surface charge density on the rods, σ=0.00179 C/m^2 used for calculating the electrostatic interactions was estimated from the zeta potential measurement. The zeta potential was measured using a Zetasizer Nano series (Malvern, United Kingdom. The non-retarded Hamaker constant for the polyamide rods was estimated from Lifshitz theory to be 1.29E-20 J. The Debye length used is 2 nm.....111

List of Tables

Table 2.1: Onset stress (τ_w*) and slope increment (δ) values obtained from drag reduction measurements for the different polymer and salt concentrations used in the study. 58

Table 3.1: Summary of translational diffusion coefficient (D_t), rotational diffusion coefficient (D_r), length (L) and diameter (D) values obtained from DDLS and AFM measurements for SWCNT-PABS and SWCNT-PEG samples. Reported uncertainties correspond to the standard error of the mean..... 83

Table 4.1: Aspect ratios of all the rod suspensions synthesized and used in the study, as taken from measurements in Wilkins et al[29]., and confirmed by reflection CLSM imaging. 112

Table 4.2: Onset volume fraction, ϕ_g obtained from Confocal microscopy for all the aspect ratios studied.....113

Abstract

This dissertation reports the development of novel experimental techniques to measure and characterize the microstructure of complex fluids and then link this microstructure to macroscale properties such as rheology and fluid dynamics. This connection between microstructure, dynamics and rheology was studied for the cases of dilute solutions of poly(ethylene) oxide, single-walled carbon nanotubes, and rigid rod colloids of polyamide.

In the complex fluid studied, aqueous solutions of poly(ethylene) oxide (PEO) were found to be in a state of molecular aggregation, which was hypothesized to be the source of their anomalous rheology and high drag reduction capability. We showed that different aggregation states can be generated in dilute solutions of Poly(ethylene) oxide by addition of chaotropic salts. We then simultaneously applied methods of dynamic light scattering (DLS) and fluid mechanics to these different aggregation states and quantitatively established the role of aggregation in turbulent drag reduction. DLS relaxation spectra of high molar mass PEO solutions in the no salt limit showed a power law scaling with exponent three, consistent with internal fluctuations of a large polymer aggregate coil. Addition of salt shifted the DLS relaxation rate scaling from three, one indicative of aggregate dynamics to two, consistent with polymer centre of mass diffusion. Such modulation of aggregate structure in PEO shifted the onset of drag

reduction by a factor of 2.5 and thus was found directly related to its drag reducing behavior.

We introduced a fast, non-invasive and reproducible method based on multi-angle depolarized dynamic light scattering to characterize the length and diameter of single-walled carbon nanotubes. Carbon nanotube dimensions were determined from simultaneous characterization of the mean translational and rotational diffusivities and using a anisotropic rigid rod model. The method was found to have quality comparable to the standard methods such as atomic force microscopy and transmission electron microscopy; however, the scattering method developed required much less time to execute.

We synthesized a simple model system consisting of self-assembled polyamide anisotropic colloids to study and characterize arrested dynamics in rod shaped colloidal particles via methods like confocal laser scanning microscopy and rheology. The glass transition volume fraction (ϕ_g) obtained in this study was found to be aspect ratio dependent, but was slightly lower than the theoretical and simulation scaling predictions for the minimum percolation volume fraction in a random homogenous network of rods. Rheological characterization of these rod suspensions revealed a unique power law scaling with exponent three for the elastic modulus, irrespective of the aspect ratio of the rod suspension studied.

CHAPTER 1
INTRODUCTION

1.1 Complex Fluids

Complex fluids are present everywhere around us. The term complex fluid refers to a class of materials that can neither be classified as a pure liquid nor a solid. Their behavior generally lies between that of a solid and liquid. For instance the mechanical response of solids and liquids under the application of stress or shear is to either maintain its state (solid) or deform continuously (liquid). These mechanical responses characterize a solid and liquid and they are said to exhibit elasticity and viscosity respectively. Complex fluids behave differently in this case since they behave both as solids and liquids at different time scales and hence are viscoelastic in nature. Typical examples of these fluids include polymer solutions, colloidal suspensions, micellar solutions, surfactant monolayers and microemulsions. All these above examples of complex fluids have complex rheological behavior when a stress or strain is applied to them. For example polymer solutions and melts behave differently under different shear rates. At very low shear rates their viscosity is a constant like a liquid (referred to as zero shear viscosity), but then at higher shear rates their viscosity decreases with increasing shear rate (referred to as shear thinning).

Complex fluids have always attracted significant attention in the scientific community due to their practical usefulness in applications such as fast ocean transport[1, 2], tertiary oil recovery[3], coatings[4-6], reinforced composite materials, pulp and paper making[7], wastewater treatment[8], drug delivery[9-11] etc. Complex fluids are loosely defined

as liquid-based materials possessing a characteristic microscopic structural length scale, due to the presence of a self-assembled or colloidal phase. It is this length scale, which plays a very important role in determining its properties for different applications[12]. Super-molecular structures (length scale ~ 0.5μm) present in dilute solutions of high molecular weight water soluble polymers give them unusual hydrodynamic flow properties. Dissolution of water soluble polymers like poly(ethylene) oxide can significantly modify turbulence in a fluid leading to drastic reduction in friction. The dynamic interactions between turbulence and the super molecular structures present in these solutions plays a significant role in drag reduction. It is thus important that we have a detailed understanding of the microscopic structure and dynamics of complex fluids, since knowledge gained can then be fruitfully applied to make advances in their applications.

The field of complex fluids is enormous and this dissertation is a small subset of this area. In my dissertation I have looked into three different types of complex fluids – high molar mass water-soluble polymers, single walled carbon nanotube suspensions and polyamide rod shaped colloidal suspensions. As described before complex fluids are characterized by a microscopic length scale, which determines its usage in applications. In this dissertation by using the above three complex fluids we have tried to probe three different length scales. The length scale of water-soluble polymer was R_g ~100-300 nm, carbon nanotubes was L ~ 0.5-1μm and for polyamide rod suspensions was L ~ 3-20 μm, where R_g. is the radius of gyration of the polymer coil and L is the length of the carbon nanotube or polyamide rod. The major theme of this work has been to understand how these different length scales present in complex fluids interact in solution at the

microscopic level and impact applications at the macroscale. Many of the material properties of these complex fluids in applications are dictated by this structure and dynamics relationship. Some questions which this thesis has been based on are as follows- 1) What is the typical size of a dilute polymer aggregate and how does it matter for applications like drag reduction? 2) Can theories like translational and rotational diffusion that have been canonical to the understanding of rigid rod polymers be applied to characterize the dimensions of carbon nanotubes? 3) How does anisotropy in microstructure affect arrested colloidal suspension dynamics and what parameters does it depend on? In the next paragraphs we discuss each of above-mentioned complex fluids in detail.

Water soluble polymers are an important component of many complex fluid formulations used in applications ranging from tertiary oil recovery[3] to drug delivery[10]. They have been a subject of great scientific and commercial interest, particularly the key water soluble polymer poly(ethylene) oxide (PEO)[13-16]. Interestingly, intrinsic polymer properties such as conformational polymer coil size or the radius of gyration (R_g), intrinsic viscosity ([η]), second virial coefficient (A_2) etc of the polymer depend heavily on the solvent[17]. The nature of poly(ethylene) oxide in solution depends to a great extent on the polymer-solvent interactions. PEO has been used heavily both in industry and academia, but still its dilute solution properties in solution are not very clear. Polymer aggregation even in the dilute limit is a very common condition of aqueous PEO solutions[18]. Due to this aggregation, dilute bead spring models such as Zimm and Rouse, which have been canonical to the understanding of polymer solution dynamics, fail to capture the viscoelastic properties of PEO in solution. Molecular aggregation in aqueous

PEO solutions has been hypothesized to be the source of their anomalous rheology[19] and flow behavior[20]. Most of the unusual properties of PEO have been attributed to the hydrogen bonding between the ether oxygen atom in PEO and hydrogen in the water molecule[16, 21]. One of the most striking applications of PEO is in fast ocean transport where a small amount (ppm) of this polymer when added to a turbulent Newtonian fluid like water can lead to drastic reduction in skin friction. Our main interest (see Chapter 2) was to investigate the relationship between aggregate structure and flow behavior (drag reduction)[1].The major purpose of this work was to improve fundamental understanding of flow effects on dilute water-soluble polymers. The lack of appropriate experimental data in this regard makes it an interesting and challenging problem to study. So an experimental plan to investigate effect of molecular conformation on flow behavior is needed, which can then stimulate the development of a new constitutive polymer model for PEO. We apply methods like dynamic light scattering and fluid mechanics in a single plan to discover the correspondence between the microscopic aggregation state and flow behavior in these solutions. An increased micro level understanding of this sort can benefit areas far removed from polymer science such as oil and ocean transport, tertiary oil recovery, drug delivery etc where use of complex fluid formulations are very common.

Carbon nanotubes (CNTs) have received a great deal of attention since their discovery by Iijima in 1991[22]. Enormous progress has been made towards carbon nanotube applications like composite materials, transistors, logic devices and nanoelectronic devices, and sensors and actuators for molecular imaging[23]. Most often these applications require efficient dispersion or solubilization of CNTs in solution[24]. The

state of aggregation of the nanotubes (or the absence of it) and their dynamic nature in solvents control a number of important physical properties of the composite medium. For instance, the fabrication of nanocomposites and the preparation of nanotube pastes for field emission displays generally require uniform dispersion of CNTs for optimal performance[25]. These dispersions are typically complex fluids where physical interactions of the carbon nanotube in the solvent at the microscale lead to interesting macroscale phenomena. For instance the dispersion quality in carbon nanotubes is highly dependent on concentration where bundling of carbon nanotubes has been seen at high concentration[24]. Understanding of geometrical properties of single walled carbon nanotubes (SWCNTs) such as length, diameter and aspect ratio is crucial for making advances in their commercial applications since most of the properties of SWCNTs such as electrical, mechanical and optical depend on nanotube dimensions[26]. Fagan et al recently showed that the optical response of SWCNTs is highly dependent on carbon nanotube length[27]. Fluorescence microscopy experiments have revealed that the uptake of DNA wrapped SWCNTs by human lung fibroblast cells is also length dependent. A minimum length threshold was determined in their experiments (L< 200nm), above which the SWCNTS were excluded from cell uptake[28]. Therefore precise characterization of single-walled carbon nanotube length and diameter is essential in a number of areas, particularly for optimizing and predicting their phase behavior and rheological properties for applications. Also due to the relative insolubility of SWCNTs in water and organic solvents not much progress has been made in estimating the hydrodynamic properties of SWCNTs in solution. Some recent attempts at understanding the mechanics and dynamics of SWCNTs have been fruitful[29]. There has been a constant drive for

development of techniques, which can help evaluate the dispersion and stability of CNTs[30], determine SWCNT dimensions[26] and dynamics[31] in solution. So there is still scope for development of new techniques for nanotube characterization. Our main motivation (see Chapter 3) was to develop a fast, non-invasive and robust technique to determine SWCNT dimensions and dynamics in solution. The work was aimed at characterization and quantification of dispersions of single walled carbon nanotubes (SWCNTs) in solvent media. Development of such techniques can help improve fundamental understanding of liquid phase behavior of complex fluid dispersions containing carbon nanotubes which can then be applied to develop scalable techniques for directed and self assembly of CNTs.

Colloidal suspensions consist of particles that are of the order from nanometer to micron in size which have been dispersed in a solvent. Colloidal suspensions can be broadly divided into two categories – those in which the particle building block is isotropic (spherical colloids) and those in which the particle is anisotropic (nonspherical colloids). Nonspherical colloids such as rods, discs, dumbbells etc have complex phase behavior compared to spherical colloids[32], which makes them interesting to study. This is due to the higher number of degrees of freedom present in nonspherical colloids due to shape anisotropy[32]. Significant amount of experimental and theoretical work has been done that elucidates how the rheology and dynamics of anisometric colloids differs from that of spherical colloids. Molecular dynamic simulations on packings prepared with the mechanical contraction method reveal significant differences between random packings of spheres and thin rods[33, 34]. A sharp maximum in the contact number distribution for rod packings has been seen[35]. Rod shaped particles also show an interesting phase separation

phenomena called the isotropic-nematic phase transition when their concentration crosses a critical concentration[36]. Rod suspensions depending on their interaction strength, aspect ratio and volume fraction form structures ranging from fractals to heterogeneous networks at much lower volume fractions compared to spherical colloidal suspensions[37]. Although rod suspensions have attracted interest in the soft matter community, not much has been done to investigate the effect of microstructure due to anisotropy on arrested or slow dynamics of rod shaped colloids. So our main motivation was to study arrested dynamics in a model rod system (see Chapter 4). The model system we used comprised of self-assembled polyamide rods dispersed in an aqueous surfactant solution. Confocal microscopy, image processing and rheology were used in this investigation. The results obtained can broadly be applied to develop complex fluid stabilization strategies, which play a key role in the consumer products such as detergents cosmetics etc. Also generating such data can help validate existing rod theories for gelation and vitrification.

We now turn to a brief overview of some of the characterization methods that were used in this work to accomplish the above mentioned goals.

1.2 Dynamic Light Scattering

Dynamic light scattering (DLS), also commonly known as photon correlation spectroscopy, is a powerful tool to study complex fluid properties. Typical applications of DLS include study of translational as well as internal coil motions of a polymer coil in solution[38], measuring rotational diffusion in anisotropic colloidal suspensions[39], investigating arrested dynamics in soft matter systems[40]. DLS typically probes dynamics over a wide range of time scales from 10^{-8} to 10^{3} seconds[41]. In this work we have used DLS effectively to characterize high molar mass PEO solutions in Chapter 2 and

Carbon nanotube suspensions in Chapter 3. In a typical DLS measurement temporal intensity fluctuations in the scattered light are determined as a function of scattering angle, θ. An important parameter in DLS is the wave vector, q which depends on the geometry of the light scattering device as shown in Fig. 1.1. k_{in} and k_{sc} represent the incident and scattered vectors respectively and q is defined as k_{in} - k_{sc}. The magnitude of q is given by

$q = \frac{4\pi n}{\lambda}\sin\left(\frac{\theta}{2}\right)$, where n is the refractive index, λ is the wavelength of the incident laser beam used in the setup and θ is the scattering angle. The significance of q lies in the fact that scattering generated at a particular q is due to structural correlations on a characteristic length scale *l** where $l^* \sim 2\pi/q$. Here *l** represents a size over which spatial correlations are measured. In DLS the time dependent intensity fluctuations for instance from a polymer coil are measured in the form of a normalized intensity autocorrelation function, $g_2(q,t)$. Here, $g_2(q,t) = \langle I(q,0)I(q,t)\rangle/(\langle I(q)\rangle_e)^2$ where I is the intensity of scattered light and $\langle I\rangle_e$ is the ensemble averaged scattered intensity of light. In dilute solutions $g_2(q,t)$ is an exponentially decaying function from which the diffusion coefficient of the polymer coil can be derived. From this diffusion coefficient measurement an effective hydrodynamic coil size of the polymer coil can be calculated via the Stokes Einstein equation[41]. Alternatively, the diffusion coefficient can be used to extract the size of particles diffusing in a colloidal suspension[42].

1.3 Confocal laser scanning microscopy

Confocal laser scanning microscopy (CLSM) is a very widely used technique in biological sciences as well as soft matter physics for direct visualization of 3D structures and dynamics of these systems. CLSM has been used successfully to provide useful insights in colloidal crystallization[43-45], electric field induced rupturing of colloidal gels[46], heterogeneity in colloidal gels[47], interactions in protein assemblies and colloid polymer mixtures[48]etc. It has been used to study arrested dynamics in hard sphere colloidal glasses[49] as well as in mechanical characterization of soft viscoelastic solids such as biofilms[50].

Confocal laser scanning microscopy works on the principle of point by point illumination of an object in a sample volume. Fig. 1.4 shows the schematic of a CLSM. Laser light, after it has been directed by the dichroic mirror, passes through the microscope objective and illuminates the sample. The light scattered (fluoresced light or just scattered and reflected light in case of no flurophores) then reaches the photo multiplier tube (PMT), which acts as a detector. The light on its way back from the sample passes through a pinhole that is placed in the conjugate focal plane of the sample right in front of the PMT. It is this pinhole that rejects all the out of focus light from reaching the PMT and makes it even possible to image dense samples with high solid content.

In a typical CLSM experiment, the computer reconstructs a two dimensional (x-y plane) image from a point by point by illumination of the specimen This is generally called an optical section of the image. A three dimensional reconstruction of the image involves measuring a series of such optical sections at different depths with the help of a

motor which moves the sample in a direction (z-direction) perpendicular to the image plane (x-y direction). It is this sectioning capability, which makes CLSM a great tool for 3D visualization. Recent developments in image processing and synthesis of new model colloidal materials have now extended the use of CLSM in quantification of colloidal suspension dynamics[51]. We use CLSM and image processing in Chapter 4 for studying arrested dynamics in a model rod system.

1.4 Outline of the dissertation

The central goal of this dissertation is to develop novel experimental techniques to study and characterize microstructure in complex fluids and relate this to observable macroscale phenomena. Three different complex fluids have been used in this dissertation namely- high molar mass poly(ethylene) oxide solutions, short functionalized single walled carbon nanotube suspensions and surfactant stabilized polyamide rod suspensions. Chapter 1 presents results of dynamic light scattering and fluid flow of dilute high molar mass poly(ethylene) oxide solutions. In chapter 2 we introduce depolarized dynamic light scattering as a potential tool to characterize carbon nanotube dimensions and dynamics. Study of structural and dynamical transitions in a model rod system via confocal microscopy, image processing and rheology is presented in chapter 4. Finally conclusions from this dissertation and possible areas of future investigation are discussed in chapter 5.

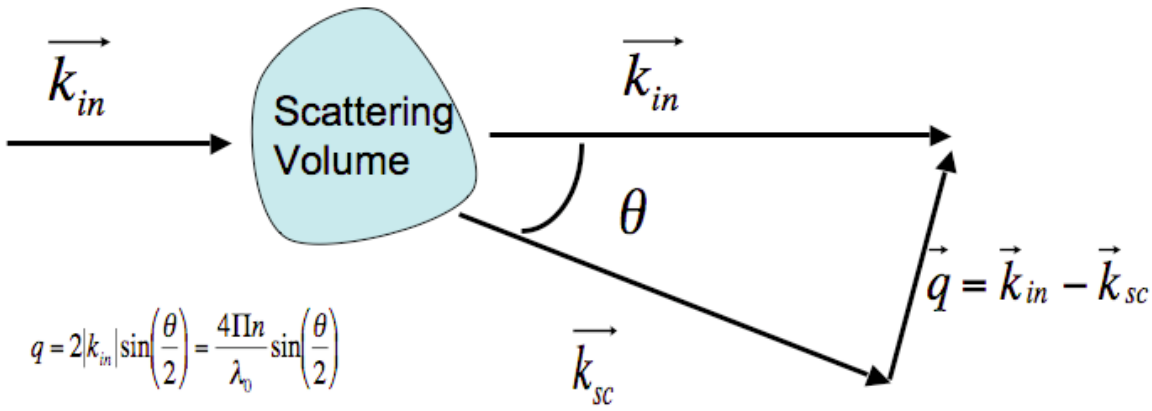

Figure 1.1: Definition of scattering vector, q and geometry of our dynamic light scattering setup.

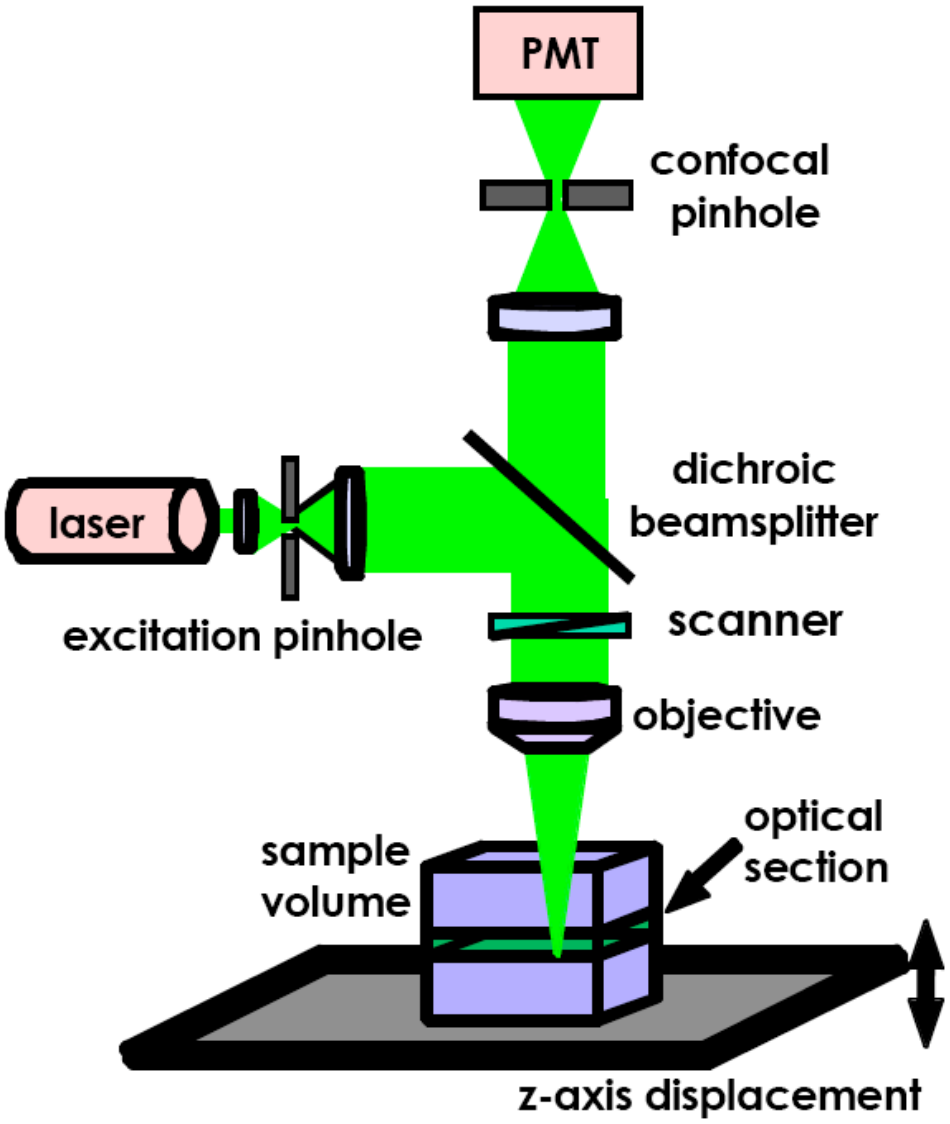

Figure 1.2: Schematic of the Leica SP2 TCS Confocal laser scanning microscope[52].

1.5 References

1. Virk, P. S., Drag reduction fundamentals. *Aiche Journal* **1975,** 21, (4), 625-656.

2. Figueredo, R. C. R.; Sabadini, E., Firefighting foam stability: the effect of the drag reducer poly(ethylene) oxide. *Colloids and Surfaces a-Physicochemical and Engineering Aspects* **2003,** 215, (1-3), 77-86.

3. Morgan, S. E.; McCormick, C. L., Water-soluble polymers in enhanced oil-recovery. *Progress in Polymer Science* **1990,** 15, (1), 103-145.

4. Trancik, J. E.; Barton, S. C.; Hone, J., Transparent and catalytic carbon nanotube films. *Nano Letters* **2008,** 8, (4), 982-987.

5. Green, A. A.; Hersam, M. C., Colored semitransparent conductive coatings consisting of monodisperse metallic single-walled carbon nanotubes. *Nano Letters* **2008,** 8, (5), 1417-1422.

6. Bekyarova, E.; Itkis, M. E.; Cabrera, N.; Zhao, B.; Yu, A. P.; Gao, J. B.; Haddon, R. C., Electronic properties of single-walled carbon nanotube networks. *Journal of the American Chemical Society* **2005,** 127, (16), 5990-5995.

7. Addai-Mensah, J.; Yeap, K. Y.; McFarlane, A. J., The influential role of pulp chemistry, flocculant structure type and shear rate on dewaterability of kaolinite and smectite clay dispersions under couette Taylor flow conditions. *Powder Technology* **2007,** 179, (1-2), 79-83.

8. Rodriguez, S.; Romero, C.; Sargenti, M. L.; Muller, A. J.; Saez, A. E.; Odell, J. A., Flow of polymer-solutions through porous-media. *Journal of Non-Newtonian Fluid Mechanics* **1993,** 49, (1), 63-85.

9. Jia, N. Q.; Lian, Q.; Shen, H. B.; Wang, C.; Li, X. Y.; Yang, Z. N., Intracellular delivery of quantum dots tagged antisense oligodeoxynucleotides by functionalized multiwalled carbon nanotubes. *Nano Letters* **2007,** 7, (10), 2976-2980.

10. Gil, E. S.; Hudson, S. A., Stimuli-reponsive polymers and their bioconjugates. *Progress in Polymer Science* **2004,** 29, (12), 1173-1222.

11. Andrews, R.; Jacques, D.; Rao, A. M.; Rantell, T.; Derbyshire, F.; Chen, Y.; Chen, J.; Haddon, R. C., Nanotube composite carbon fibers. *Applied Physics Letters* **1999,** 75, (9), 1329-1331.

12. Larson, R. G., *The Structure and Rheology of Complex Fluids*. New York: Oxford University Press: 1999.

13. Vlassopoulos, D.; Schowalter, W. R., Steady viscometric properties and characterization of dilute drag-reducing polymer-solutions. *Journal of Rheology* **1994,** 38, (5), 1427-1446.

14. Wolff, C., On the real molecular-weight of polyethylene oxide of high molecular-weight in water. *Canadian Journal of Chemical Engineering* **1980,** 58, (5), 634-636.

15. Toryanik, A. I., A structural model of an aqueous-solution of poly(ethylene oxide). *Journal of Structural Chemistry* **1984,** 25, (3), 385-388.

16. Tasaki, K., Poly(oxyethylene)-water interactions: A molecular dynamics study. *Journal of the American Chemical Society* **1996,** 118, (35), 8459-8469.

17. Rubinstein, M.; Colby, R. H., *Polymer Physics*. Oxford University Press: 2004.

18. Polverari, M.; vandeVen, T. G. M., Dilute aqueous poly(ethylene oxide) solutions: Clusters and single molecules in thermodynamic equilibrium. *Journal of Physical Chemistry* **1996,** 100, (32), 13687-13695.

19. Kalashnikov, V. N., Shear-rate dependent viscosity of dilute polymer-solutions. *Journal of Rheology* **1994,** 38, (5), 1385-1403.

20. Dunlop, E. H.; Cox, L. R., Influence of molecular aggregates on drag reduction. *Physics of Fluids* **1977,** 20, (10), S203-S213.

21. Smith, G. D.; Bedrov, D.; Borodin, O., Molecular Dynamics Simulation Study of Hydrogen Bonding in Aqueous Poly(Ethylene Oxide) Solutions. *Physical Review Letters* **2000,** 85, (26), 5583-5586.

22. Iijima, S., Helical microtubules of graphitic carbon. *Nature* **1991,** 354, (6348), 56-58.

23. Baughman, R. H.; Zakhidov, A. A.; de Heer, W. A., Carbon nanotubes - the route toward applications. *Science* **2002,** 297, (5582), 787-792.

24. Amiran, J.; Nicolosi, V.; Bergin, S. D.; Khan, U.; Lyons, P. E.; Coleman, J. N., High quality dispersions of functionalized single walled nanotubes at high concentration. *Journal of Physical Chemistry C* **2008,** 112, (10), 3519-3524.

25. Meyyappan, M., *Carbon Nantubes Scinece and Applications*. CRC Press LLC: 2005.

26. Badaire, S.; Poulin, P.; Maugey, M.; Zakri, C., In Situ Measurements of Nanotube Dimensions in Suspensions by Depolarized Dynamic Light Scattering. *Langmuir* **2004,** 20, (24), 10367-10370.

27. Fagan, J. A.; Simpson, J. R.; Bauer, B. J.; Lacerda, S. H. D.; Becker, M. L.; Chun, J.; Migler, K. B.; Walker, A. R. H.; Hobbie, E. K., Length-dependent optical effects in single-wall carbon nanotubes. *Journal of the American Chemical Society* **2007,** 129, (34), 10607-10612.

28. Becker, M. L.; Fagan, J. A.; Gallant, N. D.; Bauer, B. J.; Bajpai, V.; Hobbie, E. K.; Lacerda, S. H.; Migler, K. B.; Jakupciak, J. P., Length-dependent uptake of DNA-wrapped single-walled carbon nanotubes. *Advanced Materials* **2007,** 19, (7), 939-945.

29. Duggal, R.; Pasquali, M., Dynamics of individual single-walled carbon nanotubes in water by real-time visualization. *Physical Review Letters* **2006,** 96, (24), 246104.

30. Lee, J. Y.; Kim, J. S.; An, K. H.; Lee, K.; Kim, D. Y.; Bae, D. J.; Lee, Y. H., Electrophoretic and dynamic light scattering in evaluating dispersion and size distribution of single-walled carbon nanotubes. *Journal of Nanoscience and Nanotechnology* **2005,** 5, (7), 1045-1049.

31. Fakhri, N.; Tsyboulski, D. A.; Cognet, L.; Weisman, R. B.; Pasquali, M., Diameter-dependent bending dynamics of single-walled carbon nanotubes in liquids. *Proceedings of the National Academy of Sciences of the United States of America* **2009,** 106, (34), 14219-14223.

32. Glotzer, S. C.; Solomon, M. J., Anisotropy of building blocks and their assembly into complex structures. *Nature Materials* **2007,** 6, (8), 557-562.

33. Wouterse, A.; Luding, S.; Philipse, A. P., On contact numbers in random rod packings. *Granular Matter* **2009,** 11, (3), 169-177.

34. Wouterse, A.; Williams, S. R.; Philipse, A. P., Effect of particle shape on the density and microstructure of random packings. *Journal of Physics-Condensed Matter* **2007,** 19, (40), 406215.

35. Sacanna, S.; Rossi, L.; Wouterse, A.; Philipse, A. P., Observation of a shape-dependent density maximum in random packings and glasses of colloidal silica ellipsoids. *Journal of Physics-Condensed Matter* **2007,** 19, (37), 376108.

36. Onsager, L., The effects of shape on the interaction of colloidal particles. *Annals of the New York Academy of Sciences* **1949,** 51, (4), 627-659.

37. Solomon, M. J.; Spicer, P. T., Microstructural regimes of colloidal rod suspensions, gels and glasses. *Soft Matter* **2010,** 6, (7), 1391-1400.

38. Shetty, A. M.; Solomon, M. J., Aggregation in dilute solutions of high molar mass poly(ethylene) oxide and its effect on polymer turbulent drag reduction. *Polymer* **2009,** 50, (1), 261-270.

39. Shetty, A. M.; Wilkins, G. M. H.; Nanda, J.; Solomon, M. J., Multiangle Depolarized Dynamic Light Scattering of Short Functionalized Single-Walled Carbon Nanotubes. *Journal of Physical Chemistry C* **2009,** 113, (17), 7129-7133.

40. Wilkins, G. M. H.; Spicer, P. T.; Solomon, M. J., Colloidal System To Explore Structural and Dynamical Transitions in Rod Networks, Gels, and Glasses. *Langmuir* **2009,** 25, (16), 8951-8959.

41. Berne, B. J.; Pecora, R., *Dynamic Light Scattering*. J Wiley, New York: 1976.

42. Russel, W. B.; D.A., S.; Schowalter, W. R., *Colloidal Dispersions*. Cambridge University Press: 1989.

43. Gasser, U.; Weeks, E. R.; Schofield, A.; Pusey, P. N.; Weitz, D. A., Real-space imaging of nucleation and growth in colloidal crystallization. *Science* **2001,** 292, (5515), 258-262.

44. Shereda, L. T.; Larson, R. G.; Solomon, M. J., Local stress control of spatiotemporal ordering of colloidal crystals in complex flows. *Physical Review Letters* **2008,** 101, (3), 038301.

45. Solomon, T.; Solomon, M. J., Stacking fault structure in shear-induced colloidal crystallization. *Journal of Chemical Physics* **2006,** 124, (13), 134905.

46. Kogan, M.; Solomon, M. J., Electric-Field-Induced Yielding of Colloidal Gels in Microfluidic Capillaries. *Langmuir* 26, (2), 1207-1213.

47. Dibble, C. J.; Kogan, M.; Solomon, M. J., Structural origins of dynamical heterogeneity in colloidal gels. *Physical Review E* **2008,** 77, (5), 041403.

48. Stradner, A.; Sedgwick, H.; Cardinaux, F.; Poon, W. C. K.; Egelhaaf, S. U.; Schurtenberger, P., Equilibrium cluster formation in concentrated protein solutions and colloids. *Nature* **2004,** 432, (7016), 492-495.

49. Vanblaaderen, A.; Wiltzius, P., Real-space structure of colloidal hard-sphere glasses. *Science* **1995,** 270, (5239), 1177-1179.

50. Hohne, D. N.; Younger, J. G.; Solomon, M. J., Flexible Microfluidic Device for Mechanical Property Characterization of Soft Viscoelastic Solids Such as Bacterial Biofilms. *Langmuir* **2009,** 25, (13), 7743-7751.

51. Crocker, J. C.; Grier, D. G., Methods of digital video microscopy for colloidal studies. *Journal of Colloid and Interface Science* **1996,** 179, (1), 298-310.

52. Solomon, M. J.; Kogan, M., Confocal Optical Microscopy. *Encyclopedia of Condensed Matter Physics* **2005**.

CHAPTER 2
AGGREGATION IN DILUTE SOLUTIONS OF HIGH MOLAR MASS POLY(ETHYLENE) OXIDE AND ITS EFFECT ON TURBULENT DRAG REDUCTION

2.1 Chapter Summary

In this chapter we apply methods of dynamic light scattering (DLS) and fluid mechanics to quantitatively establish the role of aggregation in the turbulent drag reduction of high molar mass poly(ethylene oxide) (PEO) solutions. By means of DLS, we show that the dilute aqueous solutions of high molar mass PEO ($M_w \sim 4 \times 10^6$ g/mole) are aggregated and that this aggregate structure can be manipulated by addition of the chaotropic salt guanidine sulfate (GuS) or the divalent salt magnesium sulfate ($MgSO_4$). In aqueous solution, we find $\Gamma \sim q^{2.8\pm0.1}$, where Γ is the DLS correlation function relaxation rate and q is the scattering vector. This scaling is consistent with internal motions of a large coil or aggregate. Addition of salt progressively decreases the scaling to $\Gamma \sim q^{2.0\pm0.1}$ (at 0.5M of $MgSO_4$) consistent with center of mass diffusion of isolated coils. We further find that manipulating the aggregation state of PEO with $MgSO_4$ shifts the critical condition for onset of turbulent drag reduction at dilute concentrations in pipe flow by a factor of 2.5. Because this critical condition is inversely proportional to the viscoelastic relaxation time of the polymer solution, we conclude that the aggregation state and the turbulent drag reduction behavior of PEO are strongly correlated. This correlation definitively confirms prior speculation (Cox et al. *Nature* 249, 1974; Vlachogiannis et al. *Physics of Fluids*, 15, (12), 2003) that the high molar mass PEO commonly used in literature studies of turbulent drag reduction is in a state of aggregation. Furthermore, the quantitative

differences in quiescent DLS characterization and turbulent flow pressure drop measurements suggest that high molar mass PEO undergoes flow-induced deaggregation in transport systems with shear stresses as low as 0.5 Pa.

2.2 Introduction

Poly(ethylene oxide) (PEO) is an important commodity polymer used as a dilute additive in applications such as turbulent drag reduction, oil drilling and recovery, papermaking, wastewater treatment and drug delivery[1-7]. Fundamental understanding of PEO solution structure, dynamics and rheology may be fruitfully applied to advance these applications. However, the dilute solution properties of PEO have generated controversy because of significant differences between experimental observations and well-established classical theories of polymer science. For example the aqueous solubility of PEO is unexpected: the closest counterparts of PEO in the homologous series of polyethers, poly(methylene) oxide and poly(propylene) oxide, are both practically insoluble in water[8]. Aqueous solutions of PEO display a temperature dependence of solvent quality that is the inverse of typical polymer solvent pairs[9]. The aqueous PEO phase diagram also contains closed loop regions[10-12]. These anomalous solubility properties are a consequence of hydrogen bonding between the ether oxygen atom in PEO and the hydrogen in the water molecule [8, 9, 13-15].

Among the most extensively studied of the anomalous properties of aqueous PEO solutions is its clustering behavior. It has been reported that, above a critical concentration that is molecular weight dependent, polymer clusters (or aggregates) coexist in equilibrium with free polymer coils[16]. Others have found that, at concentrations much below the critical overlap concentration (c*), PEO exists as two phases, each of different polymer concentration. The polymer rich phase of these two has been reported to organize into a liquid-crystalline fibrillar network that leads to properties such as shear thinning and elasticity [17].

Aggregation of PEO in solution has been studied by electron microscopy, dynamic light scattering (DLS), static light scattering (SLS) and small angle neutron scattering (SANS)[16,18,19]. Electron micrographs of dilute solutions PEO in dimethylformamide and water solutions subjected to drying revealed supermolecular structures that were much larger than the molecular dimensions of PEO[18,20]. DLS of dilute solutions of PEO in methanol yielded intensity autocorrelation functions consistent with two relaxation times. The ability of low molecular weight PEO used in the study to form clusters depended on the history of the sample and the temperature used. The fast relaxation mode was attributed to the well-solvated dispersed monomolecular species and the slow relaxation mode was caused by the formation of aggregates in solution[21]. Both relaxation modes (as characterized by a relaxation rate, Γ) scaled with the scattering vector, q, as $\Gamma \sim q^2$, consistent with polymer centre of mass diffusion[22].

Zimm plot analysis of SLS measurements of dilute PEO solutions has revealed curvature at low angles [10, 23]. Such curvature is thought to be a very sensitive indicator of aggregation in solution[24]. Hammouda and coworkers recently concluded from SANS measurements that hydrogen bonding and hydrophobic interactions in PEO/water systems have a primary role in the formation of aggregates[19]. They observed two correlation lengths in the SANS scattering spectrum. The long range correlation was due to clustering and the short range one was due to single polymer chains[19, 25].

The anomalous rheology of dilute aqueous solutions of PEO has also been taken as evidence for presence of aggregates[26, 27]. (Here we define an aggregate in a dilute solution is a polymer structure comprised of more than one molecular chain, but which is not a sample spanning network or gel.) Dilute linear (Zimm and Rouse) and non-linear

bead spring (FENE) constitutive polymer models, which are based on parameters such as the molar mass of a single polymer chain and polymer contour length, fail to capture the rheological behavior of these solutions. For example, from measurements of capillary filament breakup, Tirtaatmadja et al have reported that the structure of high molar mass PEO at ~ 10 - 100 ppm concentrations is not consistent with the prediction of the Zimm model[28].

Measurements reported in Fig. 2.1 support the Tirtaatmadja et al. finding of a significant discrepancy between constitutive equations based on single molecule theory, and the rheology of aqueous PEO. Fig. 2.1 reports the shear-rate dependent viscosity of a common high molar mass PEO, WSR-301 (Dow Chemical, M ~ 4 x 10^6 g/mole; c/c* = 620 ppm). The least squared error fits plotted in Fig. 2.1 are for the shear–rate dependent rheology of the FENE-P (finite extensible, nonlinear elastic dumbbell, pre-averaged) constitutive equation[29]. The constitutive equation relaxation times obtained are much larger than would be predicted by the single molecule Zimm theory, even given extrapolations to low concentrations (Fig. 2.2).

An important feature of dilute aqueous solutions of high molar mass PEO is their ability to reduce friction drag in flow. It is well known that the addition of a small amount of high molar mass polymer to a turbulent Newtonian fluid flow results in drag reduction[30, 31]. High molecular weight PEO is the most commonly used polymer for turbulent drag reduction in aqueous solutions since significant drag reduction can be achieved at very small concentrations[32, 33]. However, the drag reduction capacity of dilute PEO appears to be much greater than predicted by dilute solution constitutive equations[34].

The role of PEO aggregation in turbulent drag reduction can be indirectly inferred from literature measurements. For example, viscoelastic relaxation times extracted from measurements of the onset shear stress of turbulent drag reduction in pipe flow do not agree with estimates for single molecules of PEO, as computed from the Zimm model[34]. (This assignment is possible because the onset condition for turbulent drag reduction is inversely proportional to the solution viscoelastic relaxation time[35].) Second, Dunlop and Cox concluded that molecular aggregates exist in dilute PEO solutions by monitoring the rate of change of torque with time in a spinning disk apparatus. The immediate minima preceding a steady state value in the characteristic torque-time curve was argued to be due to presence of aggregates[36]. Third, Libertore et al and Vlachogiannis et al have inferred the presence of aggregates in PEO solutions by showing that loss of turbulent drag reduction with time in PEO solutions was not related to the reduction in molecular weight of the solutions due to scission[37, 38]. Fourth, by means of small angle light scattering (SALS) and rheoptics, Libertore and coworkers observed signatures of structural heterogeneities in PEO solutions under shear which they attributed to polymer aggregation[39, 40]. Further support for the effect of aggregation on PEO drag reduction comes from direct numerical simulation. Far greater magnitudes of the polymer relaxation time have been required to model the turbulent statistics and onset phenomena of turbulent drag reduction than could be supported by single chain theories of polymer dynamics[41].

However, because experiments have yet to directly probe molecular structure and turbulent flow behavior in the same PEO system, the experimental evidence for a role of aggregation in PEO turbulent drag reduction is indirect. A definitive approach to directly

link aggregation with the anomalous drag reduction behavior of PEO would be to disrupt aggregate structure in a polymer of a particular molar mass through the effect of an additive. Such additives exist: Little and coworkers have studied the effect of salts like magnesium sulfate and potassium carbonate on the turbulent drag reduction of PEO[42, 43]. They show that progressive addition of salt decreases the drag-reducing tendency of these solutions. Yuan and coworkers have likewise demonstrated that such salts can be used as an agent to disrupt hydrogen bonding capability in aqueous soluble polymers such as poly(N-isopropylacrylamide)[44]. Lim and coworkers have found that addition of salts shifts the theta point, T_θ, of polymer-salt mixtures, which in turn has an effect on their drag reduction characteristics[45]. Based on these observations, we hypothesized that divalent and/or chaotropic salts might be a suitable method to disrupt the aggregate structure of PEO. At concentrations ~ 0.1-1M, chaotropic salts disrupt local water structure and are perhaps best known for their role as agents of cell lysis and protein denaturation [46].

Thus, the approach of this work is to systematically create different polymer aggregation states in the same polymer system by addition of the salts discussed above. Subsequently, using these polymer states, we examine the aggregate structure (by DLS) and flow behavior (by drag reduction measurements) of dilute PEO solutions.

The organization of the chapter is as follows. We first present DLS results of high molar mass PEO solutions in deionized water. These results are consistent with the dilute aggregate hypothesis. Next, by means of DLS, we show that the salts magnesium sulfate and guanidine sulfate can indeed be used as a tool to manipulate the aggregate structure of dilute PEO solutions. We finally demonstrate the significant effect of aggregate

structure on the drag-reducing tendency of these solutions by comparing results of the DLS studies with the parallel studies of turbulent drag reduction.

2.3 Experimental Section

2.3.1 Materials:

Two different grades of high molar mass poly(ethylene oxide) (PEO) were used in this study. The first is a polydisperse PEO with manufacturer reported molar mass M_w~ 4 x 10^6 g/mole (WSR-301, Dow Chemicals). The second is a monodisperse PEO with M_w~ 1.2 x 10^6 g/mole (PEO-1182K, Polymer laboratories; M_w/M_n~1.12). The overlap concentrations, c* as determined by the measurement of intrinsic viscosity (data not shown) are 620 ppm and 2600 ppm respectively. Dilute solutions of these polymers were prepared with HPLC grade water (Sigma Aldrich, for light scattering measurements) and with de-ionized water (for turbulent drag reduction experiments) from stock solutions. To prevent shear degradation, polymer solutions were prepared in 0.1L (for light scattering) and 1L (for drag reduction) bottles placed on rollers (Wheaton Science Products) rotating at 3-6 rpm for ~ 24 - 48 hours. The salts guanidine sulfate (GuS, Sigma Aldrich) and magnesium sulfate ($MgSO_4$, Sigma Aldrich) were prepared in the concentration range 0.1M - 1M. Experiments were performed within 3-4 days after dilution to minimize any possible degradation due to aging.

2.3.2 Dynamic Light Scattering (DLS)

DLS was performed on a compact goniometer system (ALV, Langen, Germany) equipped with a multi-tau digital correlator (ALV-5000E, Langen, Germany). The minimum delay time of the correlator used was 12.5 ns. A Laser source with wavelength

of λ_0 = 488 nm (Innova 70C, Coherent Inc., Santa Clara, CA) was used. Measurements were done in the angular range q = 20^0-115^0 (5.94 μm^{-1} < q < 28.86 μm^{-1}) so as to span at least a decade in q, the scattering vector, where $q = \frac{4\pi n \sin\left(\frac{\theta}{2}\right)}{\lambda_0}$. Here n is the refractive index of the solvent, λ_0 is the wavelength of incident light source and θ is the scattering angle. In a typical DLS experiment, the normalized intensity autocorrelation function, $g_2(t) = \langle I(t)I(0)\rangle / \langle I\rangle^2$ is measured. In dilute solution $g_2(t)$ is an exponentially decaying function:

$$g_2(t) = \exp(-2\Gamma t) = \exp(-2t/\tau) \qquad (2\text{-}1)$$

Here Γ is the previously described DLS relaxation rate, inversely related to the DLS relaxation time, τ, of the polymer. Both quantities are q-dependent. Typical measurements of the measured $g_2(\tau)$ for a 20 ppm (c/c* ~ 0.03) aqueous solution of PEO WSR 301 over a range of scattering angles are plotted in Fig. 2.3. The probability distribution of the relaxation time spectra was obtained by a CONTIN (constrained regularization) deconvolution of the correlation functions[47]. (Other means of analysis, such as the method of cumulants, yield analogous results.) Fig. 2.4 reports the probability distribution function of the CONTIN relaxation time spectrum measured for a typical duration of 600 s. All measurements are at T = 298 ± 0.5 K. The sample vials used were cleaned by first sonicating them in acetone for about an hour, drying them overnight and then subjecting them to UV ozone treatment (UVO cleaner, Jelight, Irvine, CA) to ensure that they were free from any organic residue. The polymer and salt solutions prepared were filtered using a 1.5 μm filter (Whatman 25mm GD/X syringe filters) prior to DLS measurements.

2.3.3 Turbulent drag reduction characterization

The pipe flow experiment for characterization of polymer turbulent drag reduction has been previously described [48]. The apparatus has the following capabilities: First, to access the very low wall shear stresses (τ_w ~ 0.5 - 1 Pa) associated with the onset of turbulent drag reduction in high molar mass aggregated PEO solutions, a test section consisting of ½ inch diameter stainless-steel pipe was used. Second, to access the small pressure drops associated with low wall shear rates, a highly sensitive differential pressure transducer (GP50, Grand Island, NY, range 0 – 0.18 psi) was used. Pressure drop measurements were performed across a test section 0.7m long. The pressure transducer responses were acquired via a National Instruments LABVIEW data acquisition system (Model USB-6009). Since fully developed flow is more difficult to realize in polymer solutions than in Newtonian fluids, a large entrance length (L/D=290) was incorporated prior to the test section[49]. We found that no static pressure correction was required in our pressure drop measurements due to the relatively low Reynolds number (~10^4) of the experiments[50].

The standard means to report friction drag reduction for a polymer is the Prandtl-van Karman plot35. The axes of the plot are $\frac{1}{\sqrt{f}}$ (ordinate) and $\mathrm{Re}\sqrt{f}$ (abscissa). Here f is the friction factor, $f = \frac{2\tau_w}{U_{av}^2 \rho}$, where τ_w is the wall shear stress, U_{av} is the mean fluid velocity in the flow direction averaged across the pipe's cross-section. Re is the Reynolds number given by $\mathrm{Re} = \frac{dU_{av}}{\nu_s}$, where d is the pipe diameter and ν_s is the kinematic viscosity of the fluid. Fig. 2.5 reports drag reduction measurements for different

concentrations of WSR-301 as a Prandtl-van Karman plot. The lower solid line is the Prandtl-Karman (PK) curve – the friction drag for a Newtonian fluid - and the upper solid line is the maximum drag reduction asymptote (MDR) – an (empirical) upper bound for friction drag reduction in polymer flows. Functional forms for these two limiting behaviors are given in the reference by Virk[35]. In Fig. 2.5, as the ordinate increases, friction drag decreases. The performance of the device over the conditions of interest ($400 < \mathrm{Re}\sqrt{f} < 1000$) was verified by measurements with water. As shown in Fig. 2.5, the results for water agree well with the Newtonian result, the Prandtl – van Karman line.

At dilute polymer concentrations, pressure drop flow rate measurements in pipe flow follow the Prandtl - Karman (Newtonian) curve until a critical wall shear rate τ_w^* is reached. Above this point, as shown in Fig 2.5 for a dilute solution of the high molar mass polymer PEO, Virk discusses that τ_w^* is determined by a critical Weissenberg number (Wi^*). This critical Weissenberg number for the onset of drag reduction depends on polymer related variables and is given by $Wi^* = \frac{\lambda \tau_w^*}{\mu}$, where λ is the relaxation time of the polymer, τ_w^* is the onset wall stress and μ is the viscosity of the solvent[35]. Further, Virk also shows that this critical Weissenberg number is a constant for all drag reduction flows and is given by $Wi^* = \frac{5.5K_\lambda}{H}$, where K_λ is the width of the relaxation time spectrum for the polymer and H is the heterogeneity index of the polymer. (Note K_λ and H are both phenomenological constants for a particular polymer-solvent combination. For example, Virk lists $K_\lambda = 1$ and H = 3.5 for WSR 301. Thus, Wi* = 1.6 for this polymer.)

This discussion anticipates the potential relationship between onset of turbulent drag reduction and aggregate structure. Aggregation will affect the viscoelastic relaxation

time of the dilute polymer solution. This effect will shift the onset condition for turbulent drag reduction because onset is controlled by a critical Wi*.

A general equation to correlate the drag reduction behavior for a polymer is[35]:

$$\frac{1}{\sqrt{f}} = (4+\delta)\log_{10}\left(\mathrm{Re}\sqrt{f}\right) - 0.4 - \delta\log_{10}\left(\left(\mathrm{Re}\sqrt{f}\right)^*\right) \qquad (2\text{-}2)$$

Here δ is the slope increment, which increases with increasing polymer concentration and polymer molecular weight. $\left(\mathrm{Re}\sqrt{f}\right)^*$ is the value of $\left(\mathrm{Re}\sqrt{f}\right)$ at the onset of drag reduction. It is the point where the polymer drag reduction curve intersects the Prandtl-Karman curve. Note that $\left(\mathrm{Re}\sqrt{f}\right)^*$ is simply related to the onset condition, τ_w^* through the following equations:

$$\left(\mathrm{Re}\sqrt{f}\right)^* = \frac{\sqrt{2}u_\tau^* d}{\nu_s} \text{ where } u_\tau^* = \sqrt{\frac{\tau_w^*}{\rho}} \qquad (2\text{-}3)$$

In the above equations u_τ^* is the onset pipe friction velocity and d is the diameter of the pipe used for the study. Note that knowledge of the onset condition and slope increment specifies the turbulent drag reduction of a polymer in turbulent flow in a pipe of a particular diameter. Generally, τ_w^* and delta are both a function of polymer molar mass (and/or aggregate structure). δ is also a function of the polymer concentration with a typical dependence of $\delta \sim c^{1/2}$ observed[35].

2.4 Results

2.4.1 DLS of dilute aqueous solutions of PEO.

The q-dependence of the DLS relaxation rate at dilute concentrations of PEO WSR-301 as obtained by CONTIN deconvolution is plotted in Fig. 2.6. In particular, CONTIN

analysis of the measured $g_2(t)$ yielded a single-mode relaxation at all conditions. The peak of the CONTIN relaxation spectrum for each scattering vector, q, and polymer concentration, c, studied is plotted. The data show negligible dependence on polymer concentration over the 5 – 50 ppm range studied. Thus, we conclude that these measurements are indeed performed in the dilute regime, consistent with the measured overlap concentration for this system, c* = 620 ppm. All further measurements reported in this paper are in this dilute concentration range.

Interestingly, the power law scaling of the measured relaxation rate Γ with q is not consistent with center-of-mass diffusion of a single-polymer coil (where Brownian motion of the entire polymer coil is measured). For a dilute polymer system, in the limit $qR_h << 1$, $\Gamma = Dq^2$, where D is the self-diffusion coefficient of the polymer coil[22]. Instead, a power law fit to the Fig. 2.6 data yields $\Gamma = 1.47 \times 10^{-18} q^{2.8\pm 0.1}$. The discrepancy between the theoretical and experimental scaling exponents is significant. We conclude that the q range of our instrument, $5.94\ \mu m^{-1} < q < 28.86\ \mu m^{-1}$, is not such that $qR_h < 1$. From published correlations, we predict the single molecule $R_h \sim 85$ nm for the PEO studied in Fig. 2.6, a size for which $qR_h \sim 1$[51] ($qR_h = 0.5$ at $\theta = 20^\circ$).

To explain this puzzling result, we recall that the dynamic response of a polymer chain in the $qR_h >> 1$ limit for the Zimm model in a good solvent is $\Gamma = 0.07kTq^3/\eta$, where η is the viscosity of the solvent, k is the Boltzmann constant and T is the temperature[22]. The predicted $\Gamma \sim q^3$ scaling has been previously observed by Adam and Deslanti for dilute solutions of very large ($M_w = 24 \times 10^6$ g/mole) polystyrene molecules in benzene[52]. The scaling exponent of three reflects internal fluctuations of the polymer coil with inclusion of hydrodynamic interactions.

Based on these previous observations for large single chains, we hypothesize that the unusual scaling reported in Fig. 2.6 is due to the effect of internal fluctuations of large single polymer aggregates. That is, if WSR-301 aggregates to the extent that the Fig. 2.6 measurements are in the regime $qR_{h,agg} >> 1$, then the scaling of Fig. 2.6 could be explained by the Zimm model result $\Gamma \sim q^3$. This hypothesis implicitly assumes that internal fluctuations of large polymer aggregates and large single polymer chains yield comparable DLS relaxation spectra. The plausibility of this point is addressed further in the discussion section.

We now turn to the magnitude of the prefactor, 1.47×10^{-18}, determined from Fig. 2.6 The Zimm model theory predicts a prefactor magnitude of 3.24×10^{-19} and 2.77×10^{-19} for a theta and good solvent, respectively (for the viscosity of H_2O at T = 298 K). Thus, although the q^3 scaling of Fig. 2.6 agrees well with the aggregate hypothesis, the prefactor differs significantly from the Zimm theory. This discrepancy is perhaps not unexpected, since the theory was developed for the dynamics of a single bead-spring chain. This point is further addressed as well in the discussion section. We determined that other potential explanations of the Fig. 2.6 results were not consistent with the data. In particular, the results are not explained by the semi-dilute dynamics of polymer solutions because in the semi-dilute regime bimodal relaxation behavior is observed[22, 53]. Moreover, both relaxation modes in semi-dilute solutions show $\Gamma \sim q^2$ scaling[54, 55]. We also considered the effect of polydispersity. To address this point, we performed DLS of dilute solutions of a high molar mass monodisperse PEO with $M_w \sim 1.2 \times 10^6$ g/mole. In Fig. 2.7 we report the DLS relaxation rate at dilute concentrations of monodisperse PEO ($M_w = 1.2 \times 10^6$ g/mole; 15-150ppm) as obtained by CONTIN deconvolution. The critical overlap

concentration measured for this polymer is c* = 2600 ppm (data not shown). The best-fit relationship to the data in Fig. 2.7 is: $\Gamma = 2.67 \times 10^{-17} q^{2.7\pm0.1}$. Thus, we conclude that the q^3 scaling characteristic of internal dynamics is independent of polydispersity. In addition, it appears that the scaling prefactor is a function of polydispersity and/or molar mass, since it changes by about a factor of ten as the system is varied from the polydisperse WSR-301 to the monodisperse polymer with molecular weight of 1.2×10^6 g/mole.

2.4.2 Manipulation of PEO aggregate structure with addition of salt.

We studied the effect of the salts guanidine sulfate (GuS) and magnesium sulfate ($MgSO_4$) on the DLS relaxation spectra of dilute solutions of aqueous PEO. As in the case of the salt-free solutions, CONTIN deconvolution showed a single, q-dependent peak in the decay spectrum. Fig. 2.8 reports the q-dependence of this relaxation rate of a 5ppm solution of WSR-301 (polydisperse; $M_w \sim 4 \times 10^6$ g/mole) for $MgSO_4$ added at concentrations of 0.25 M, 0.5 M and 1.0 M. Salt free data from Fig. 2.6 are also plotted for reference. The figure shows that the relaxation rates scale as a power law for all $MgSO_4$ concentrations. We find that the magnitude of the scaling exponent monotonically decreases with salt concentration from 2.8 ± 0.1 for salt free solutions to 1.9 ± 0.1 for 1.0 M $MgSO_4$ additives (errors reported are standard error of the mean of three replications of the curves).

Earlier we discussed two limiting cases for the DLS relaxation spectrum of dilute solutions. In the limit $qR_h << 1$, $\Gamma \sim q^2$, reflecting center-of-mass diffusion; for $qR_h >> 1$, $\Gamma \sim q^3$, reflecting internal coil dynamics. Thus, the likely interpretation of the Fig. 2.8 is that the addition of salt shifts the DLS relaxation spectrum between these two limits. To

yield the shift in limits, addition of salt could destroy the aggregate structure found in aqueous solution. As the balance between aggregates and single chains shifts, R_h decreases, and the change in limiting scaling behavior is realized.

A check of this interpretation would be to compute an effective R_h from the diffusive scaling at high salt concentrations, and assess whether this R_h is consistent with the expected dimensions of high molar mass PEO. To perform this calculation, we use the Stokes-Einstein relationship, $R_h = \frac{k_b T}{6\pi\eta D}$. Here η is the viscosity of the salt-solution (measured by capillary viscometry to be 0.00133 Pa-s). By this method, we estimate R_h ~ 290 nm for WSR 301 in 0.5 M $MgSO_4$. This value of R_h is large – corresponding to an effective molar mass ~ 3 x 10^7 g/mole, on the boundary of a physically realistic value and perhaps indicating that PEO in salt solution still comprises some residual aggregate character. Nevertheless, the key finding is that the addition of salt decreases the effective size of WSR301 into a range where its center of mass diffusion can be measured by DLS.

To address whether the Fig. 2.8 observations are specific to the particular polymer/salt pair studied, we performed an additional study with a different polymer (150 ppm monodisperse PEO with M_w~1.2 x 10^6 g/mole) and a different salt (GuS). A comparison of the DLS relaxation spectrum for PEO in salt-free and 0.85 M GuS solution is plotted in Fig. 2.9. Although both solutions yield only a single relaxation peak, the peaks are significantly broader for the aqueous solution than for the salt solution. The shift in the peak location measures the change in polymer fluctuations. The q-dependence of this change is plotted in Fig. 2.10. The results for this polymer/salt pair are consistent with Fig. 2.8: the relaxation rate scaling shifts from one indicative of aggregate dynamics ($\Gamma \sim q^{2.7}$) to one characteristic of polymer center-of-mass diffusion ($\Gamma \sim q^{2.0}$).

Thus, the data of Figs. 2.8, 2.9 & 2.10 are consistent with the hypothesis that the salts GuS and $MgSO_4$ disrupt PEO aggregate structure in dilute solution, thereby yielding a solution of single coils. In additional experiments, we explored the intermediate salt concentration range for GuS at 0.25M and 0.5M. The additional data plotted in Fig. 2.11 display a complex q-dependence that cannot be described by a power law scaling. Thus, the effect of the salt GuS on PEO DLS does not display the monotonic dependence on concentration as observed for $MgSO_4$ in Fig. 2.8. Nevertheless, power law scalings with well-characterized exponents are obtained in the high salt limit of 0.85M GuS and 1M $MgSO_4$.

2.4.3 Effect of aggregate structure on turbulent drag reduction.

In this section we quantify the effect of aggregate structure on the turbulent drag reduction behavior of the PEO polymer WSR-301 in pipe flow. As discussed in the methods section, the two characteristic quantities used to gauge the drag reducing effect in the turbulent flow of a polymer are the condition for onset of drag reduction, τ_w^*, and the slope increment, δ [35]. These quantities can be characterized from the friction factor - Reynolds number measurements reported on the Prandtl-van Karman plot of Fig. 2.12. Fig. 2.12 compares the behavior of the high molar mass polymer WSR 301 in salt-free and 0.5M $MgSO_4$ at the dilute concentrations of 2, 5 and 25 ppm. Based on the DLS results reported in the previous sections these results compare the behavior of aggregated (aqueous) and de-aggregated (0.5M $MgSO_4$) PEO.

The onset wall shear stress, τ_w^*, for polymer drag reduction is estimated by a linear extrapolation of the polymer curve (as per eqn. 2-2) to its intersection with the Newtonian Prandtl-Karman curve. The slope increment, δ, is simply related to the slope

of the least-squared fit to the data, as per eqn 2-2. Table 2.1 reports the onset stress (τ_w^*) and slope increment values for the different polymer and salt concentrations from Fig. 2.8. Errors in the table were estimated by unweighted least square fit analysis. The table shows a significant effect of salt, and thus aggregate structure, on both these quantities.

To better judge the effect of aggregate structure on drag reduction, we plot the onset stress condition for drag reduction obtained from Fig. 2.12 and Table 2.1 as a function of polymer concentration in Fig. 2.13. Plotted also is the predicted onset wall shear stress for WSR 301 given the assumption of unaggregated, single-molecule behavior. (This prediction is computed from the correlation, $R_g^3 \tau_w^* = \Omega_T$, for onset of polymer drag reduction given by Virk[35]. Here R_g is the radius of gyration for the polymer, as estimated from published correlations for PEO[51], and Ω_T is an average onset constant for PEO. As given in Virk $\Omega_T = 4.4 \times 10^6$). Error bars plotted for the onset stress are from the unweighted least square fit analysis, as in Table 2.1.

Fig 2.13 confirms that the pipe flow experiments of aqueous (salt-free) WSR-301 solutions yield anomalous drag reduction behavior relative to the single-molecule prediction. If we were to assume that the salt-free measurements were explained by single-molecule behavior, we would estimate from that the effective molar mass of WSR 301 is ~ 7×10^6 g/mole. Although this effective molar mass, extracted from a turbulent flow experiment, is greater than expected for WSR 301, its magnitude is not physically implausible. However, this effective molar mass is entirely inconsistent with the q^3 scaling of the aqueous DLS relaxation rates reported earlier. That is, if the quiescent molar mass of WSR 301 were indeed ~ 7×10^6 g/mole, then we would predict R_h ~ 117

nm, a value characterizable by DLS, as well as consistent with the observation of a q^2 scaling of the polymer relaxation rate, rather than the measured q^3 dependence.

The difference between the DLS and turbulent drag reduction data is likely explained by a role for flow-induced de-aggregation of WSR-301 in the turbulent pipe flow experiments. If the Re ~10^4 flow breaks down aggregate structure of quiescently aggregated solutions, then the effectively single-molecular behavior of Fig. 2.13. is explained. Because the effect of de-aggregation is apparent in the onset condition, its effect is already significant in the piping system for flows as weak as $\tau_w \sim 0.5$ Pa.

Turning to the drag reduction in the 0.5M $MgSO_4$ solutions, we find that the observed behavior is much closer to the single-molecule prediction. This result is quite consistent with the molecular scale DLS measurements. Could the observed shift in the onset stress for WSR 301 be explained by a change in solvent quality from good (salt free) to theta (0.5M $MgSO_4$), as supposed to a change in the aggregate structure as suggested by the light scattering measurements? To address this possibility, consider the following analysis:

From the Zimm bead spring theory for single polymer chains, the relaxation time $\lambda \sim [\eta]\eta_s M/RT$, where η_s is the solvent viscosity, R is the ideal gas constant, T is the absolute temperature and [η] is the intrinsic viscosity of the polymer. In a good solvent system, [η] ~$M_w^{0.8}$ and for a theta solvent, [η] ~$M_w^{0.5}$ (from Mark-Houwink equation)[56]. Based on the critical Weissenberg number, Wi*[57-59], for onset of polymer drag reduction given by Virk [35], $Wi^* = \frac{\lambda \tau_w^*}{\mu}$, we estimate $\frac{\tau_{w,T}^*}{\tau_{w,G}^*}$, where the subscripts T and G indicate a theta (PEO-0.5M $MgSO_4$) and good solvent (PEO-salt free) respectively. We compute this ratio to be 1.5, which is less than the experimentally observed ratio of 2.5. Thus, we

conclude the differences in Fig. 2.13 are not simply a consequence of solvent quality effects.

Furthermore, the measured slope increments, δ, for both the aqueous polymer and polymer-salt case in our studies have approximately a square root dependence with concentration, which is consistent with Virk's results (based on analysis not shown of the Table 2.1 results). The slope increments observed in the salt case are considerably lower than observed in the aqueous polymer case.

Thus, we conclude that addition of salt modulates the aggregate structure of WSR-301. This modulation is directly correlated to the drag reduction behavior of WSR-301. By linking molecular and macro scale observations, the combination of turbulent drag reduction data (Figs. 2.12 and 2.13) and DLS characterization of the polymer solutions (Figs. 2.6 -2.11) establishes that aggregate structure plays a significant role in the turbulent drag reduction of high molar mass PEO.

2.5 Discussion

The principal result of the DLS studies is that the effective size of high molar mass PEO in aqueous solution is too large for center of mass diffusion to be probed in a wide-angle light scattering device. The scaling of the relaxation rate, Γ, with q^3 observed is reminiscent of the pioneering work of Adam and Deslanti[52], in which internal fluctuations of a large polystyrene chain were probed in benzene. Because the bare hydrodynamic radius of a single molecule of WSR 301 PEO is too small to yield the result $\Gamma \sim q^3$ by itself, we propose that the scaling is due to the effects of aggregation.

However, this hypothesis raises a number of questions. For example, $\Gamma \sim q^3$ is a prediction of the Zimm model for internal coil motions[52] – it is valid for a Gaussian chain

with hydrodynamic interactions. How good is the hypothesized analogy between a large aggregate and single polymer coil? To address this question, we plot in Fig. 2.14 the theoretical curve $\Gamma = 0.07kTq^3/\eta$ for the Zimm model along with the dilute, aqueous PEO data. (These data are as Fig. 2.6 and Fig 2.7; however, they are now replotted as Γ/q^2 to emphasize the deviation from center-of-mass diffusion, which would appear as a horizontal line in the figure.) It is clear from Fig. 2.14 that the PEO relaxation rate data obeys the correct scaling as the internal fluctuation theory but falls below the predicted curve. This discrepancy in prefactor depends on the details of the polymer – we observe a different prefactor for the polydisperse, high molar mass WSR 301 ($A = 1.47 \times 10^{-18}$) than for the monodisperse polymer of 1.2M molar mass ($A = 2.67 \times 10^{-17}$). To our knowledge there is as yet no theory or simulation of dilute aggregate dynamics that would explain the correspondence between our measurements and those of Adam and Deslanti[52]. Yet, the correspondence is reasonable: Just as in a single Gaussian coil, for which the dynamics of the two chain ends contribute negligibly to the internal q^3 dynamics, so would the contacts between the multiple PEO molecules in an aggregated cluster be expected to negligibly affect internal dynamics. Then, because the Zimm model scaling is independent of molar mass, dilute aggregate high q dynamics would be similar to the single molecule prediction.

In considering the results of Fig. 2.6 & 2.7, we note that our measurements appear to disagree with previous DLS studies of dilute PEO dynamics. These previous studies have reported observation of two relaxation rates, both of which scaled as q^2 [16, 21, 60]. In the present study a single dominant relaxation rate scaling as q^3 is observed. Can these

different data sets be reconciled? One difference in the studies is the concentration. Although all these studies are dilute ($c<c^*$), the earlier work of Duval et al ($c/c^*>0.1$) as well as Ho et al ($c/c^*>0.3$) are at greater concentration than our work (for which $0.001 < c/c^* <0.08$). Moreover, Polverari et al observed two peaks in their PEO DLS relaxation spectrum above a molecular weight dependent critical self-association concentration. If the self-association that leads to aggregation is viewed as a phase separation (akin to a micellization transition) in which single chains are in equilibrium with aggregate clusters, it seems likely that the ultra-dilute concentrations of this study render the concentration of single chains so small as to be undetectable by DLS. Thus, the observation of single relaxation behavior here is not inconsistent with the earlier studies, but instead is explained by the ultra-dilute concentration range studied. (Recall that these ultra-dilute concentrations are exactly the ones of interest for applications such as turbulent drag reduction.)

To further test this explanation, we performed DLS experiments at a higher, but still dilute, concentration (100 ppm WSR 301: $c/c^* = 0.16$). We observed two peaks in the DLS relaxation spectrum. Thus, we conclude that at ultra-low concentrations ($c/c^* < 0.1$), PEO quiescent dynamics is dominated by the behavior of aggregate clusters.

Although the quiescent dynamics of high molar mass PEO is dominated by the effect of polymer aggregates, the analysis of the drag reduction measurements of Fig. 2.13 also supports a role for flow-induced de-aggregation in turbulent flow. For example, although the shift in drag reduction onset condition (and therefore viscoelastic relaxation time) upon addition of $MgSO_4$ is too great to be explained as a simple effect of solvent quality, the apparent molar mass for WSR-301 extracted by application of Virk's well-

established phenomenology is ~ 7 x 10^6 g/mole, a number that is reasonably explained by single-molecule ideas. A probable explanation of the difference between the quiescent DLS and the turbulent results is the effect of flow-induced degradation. Here two possibilities should be considered. The first is single-chain scission due to covalent bond breakage. The second is PEO aggregate degradation due to rupture of intermolecular associations mediated by, for example, hydrogen bonding[61].

Polymer chain scission is typically apparent in Prandtl-van Karman plots such as Fig. 2.12 as deviation at high $Re f^{0.5}$ from eqn. (2-2). The deviation results in a maximum in $f^{0.5}$ with further decline as $Re f^{0.5}$ increases[48,62]. Furthermore, the onset of these deviations can be quantitatively predicted by the Kolmogorov cascade theory of turbulent chain scission by Vanapalli et al[63]. By considering these two effects below, we conclude that the measurements here are not affected by single chain scission.

First, we observe no deviation from eqn (2-2) in the Prandtl-Karman plots (Fig. 2.5 and Fig. 2.12). Indeed, Vanapalli et al have shown that for PEO with mean molar mass of about 4 x 10^6 g/mole, polymer scission affects the drag reduction curves only for $\left(\mathrm{Re}\sqrt{f}\right)$ values greater than ~ 1000[48], much larger than the values probed in this study. Second, application of the Kolmogorov cascade scission theory given the covalent bond strength of PEO (~ 4.1 nN[63]) yields an expected onset of covalent scission for $\left(\mathrm{Re}\sqrt{f}\right)$ ~ 2300, well above the range of our measurements. This estimate is given by $F_{\max} \sim \frac{\pi\mu^2 \mathrm{Re}^{\frac{3}{2}} L^2}{4\rho d^2 \ln(L/a)}$ where F_{max} = 4.1nN, μ is the viscosity, Re is the Reynolds number, ρ is the fluid density, d is a characteristic geometric dimension of the flow, a is a characteristic radius of the polymer chain and L is the contour length of the polymer

chain[63]. Thus, we also conclude that the 7 x 10^6 g/mole estimate of the effective molar mass of PEO in the drag reduction experiment is not a consequence of polymer chain scission. Instead, the quiescent aggregate structure quantified by the DLS does not appear to fully survive the turbulent flow.

Even though some flow-induced de-aggregation is observed, because the addition of salt significantly reduces the measured turbulent drag reduction in a way that cannot be explained by simple solvent effects, we conclude that the differences in Figs. 2.12 and 2.13 are due to the effect of salt on residual aggregate structure. If the aggregate hypothesis is correct, can we estimate from these data a lower bound on the size of the PEO aggregates studied? This question is addressed by Fig. 2.15, which plots schematically the transition from low q to high q behavior that would be observed for different aggregate sizes. The DLS data reported in Fig. 2.6 & 2.7 must fall on the right hand side of Fig. 2.15. What size range is consistent with the $qR_h >> 1$ constraint and the q-range of our instrument? For guidance, we return to the earlier work of Adam and Delsanti[52], who found q^3 scaling for measurements on single chains provided $qR_g > 4.4$. If we apply this constraint, we conclude that a lower bound for $R_{g,agg} \sim 740$ nm for the polymers studied here. Improving this estimate should be a principal aim of future work.

We conclude the discussion by suggesting a way in which small-angle dynamic light scattering[64] could be applied to definitively characterize the size of PEO aggregates at ultra-dilute conditions. As discussed earlier, the dynamic response of a dilute polymer solution can be divided into different regimes based on the magnitude of the dimensionless scale qR_h, where R_h is the hydrodynamic radius of the polymer and q is the scattering wave vector, as schematically plotted in Fig 2.15. In a sufficiently small q

limit, the dynamic light scattering spectra of dilute PEO solutions should be consistent with centre of mass diffusion of multi-molecule aggregates with an effective hydrodynamic radius that is many times greater than the hydrodynamic response of a single molecule of PEO. In the high q limit internal dynamics are probed, as per Fig. 2.6 & 2.7. The transition between the two dynamical regimes occurs at $qR_{agg} \sim 1$. Given estimates from this study, R_{agg} could be as large as 740 nm. Thus a DLS device that can probe $q << 1.33\ \mu m^{-1}$ is required, corresponding to $\theta << 6°$. Such small-angle DLS instruments have recently become available[64, 65].

2.6 Conclusions

This work addresses the problem of PEO aggregation in aqueous solution by building upon the earlier work of Polverari et al, Hammouda et al, and Liberatore et al [16, 19, 25, 39, 40]. The current study uses a unique chaotropic/inorganic salt and simultaneous dynamic light scattering/fluid dynamics methodology to study dilute PEO aggregate flow properties. We find:

1) The DLS relaxation spectra of high molar mass dilute aqueous PEO solutions show a single peak that scales as $\Gamma \sim q^3$, where Γ is the relaxation rate and q is the scattering vector. This scaling is consistent with DLS detection of internal fluctuations of a polymer aggregate of size at least 740 nm.

2) Addition of an inorganic ($MgSO_4$) or chaotropic salt (GuS) decreases the power law scaling of the relaxation rate scaling from q^3 to q^2. This shift from a scaling indicative of aggregate dynamics ($\Gamma \sim q^3$) to one characteristic of polymer center-of-mass diffusion ($\Gamma \sim q^2$) shows that these salts are effective de-aggregation agents for PEO.

3) The DLS results are predictive of the behavior of PEO in turbulent flow. Addition of $MgSO_4$ significantly decreases the effectiveness of PEO as a drag reduction agent. The effect is greater than can be explained by single molecular solvent quality effects. The level of drag reduction observed when compared to the DLS measurements suggests that turbulent flow de-aggregates high molar mass PEO, even in mild flow systems with shear stresses ~ 0.5 Pa.

These results improve our fundamental understanding of the behavior of dilute solutions of high molar mass PEO by placing bounds on the size of quiescent aggregates, by demonstrating the effect of salt on aggregate structure and by linking aggregate structure to flow behavior of PEO.

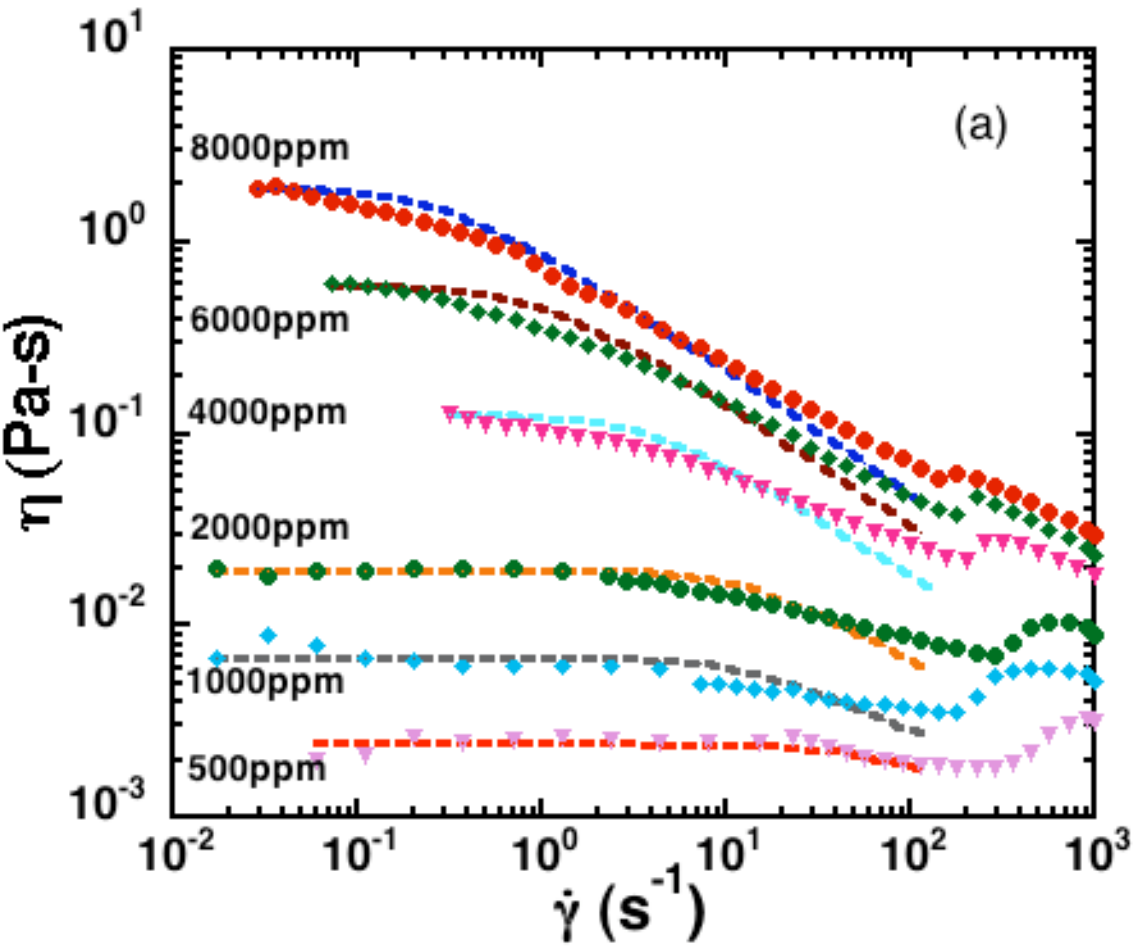

Figure 2.1: Quiescent rheological characterization of aqueous PEO WSR-301 (M_w~ 4 x 10^6 g/mole) at T=25^0 C in a 2^0 60 mm cone and plate geometry. The viscosity, η, is plotted for a series of PEO concentrations (500-8000 ppm) as a function of shear rate, $\dot{\gamma}$. The dashed curves are best fits to the data for the FENE-P constitutive equation with η_s= 0.001 Pa-sec and L^2=1000.

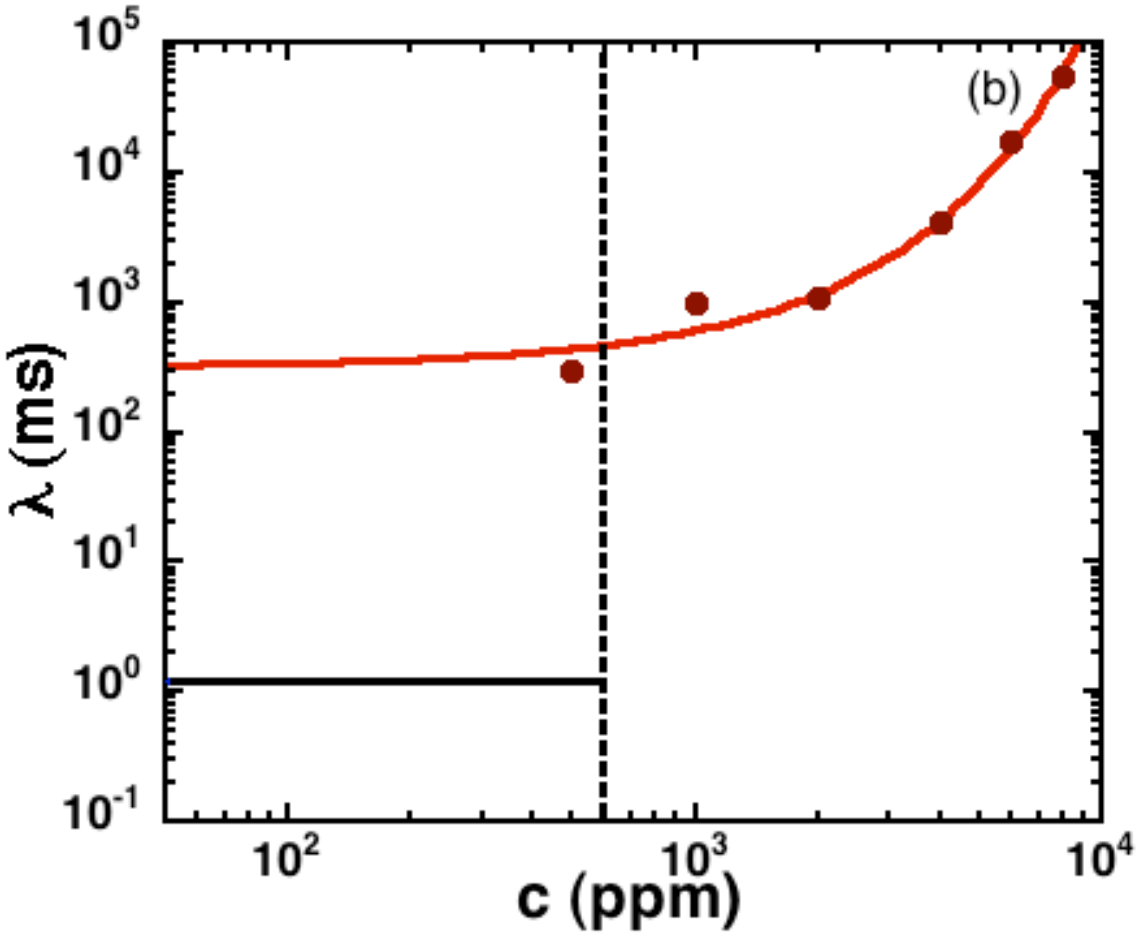

Figure 2.2: Concentration dependence of the viscoelastic relaxation time (ms) of WSR-301 from FENE-P curve fits for the experimental data from Fig. 2.1 at various concentrations. The horizontal line is the dilute solution prediction by Zimm theory.

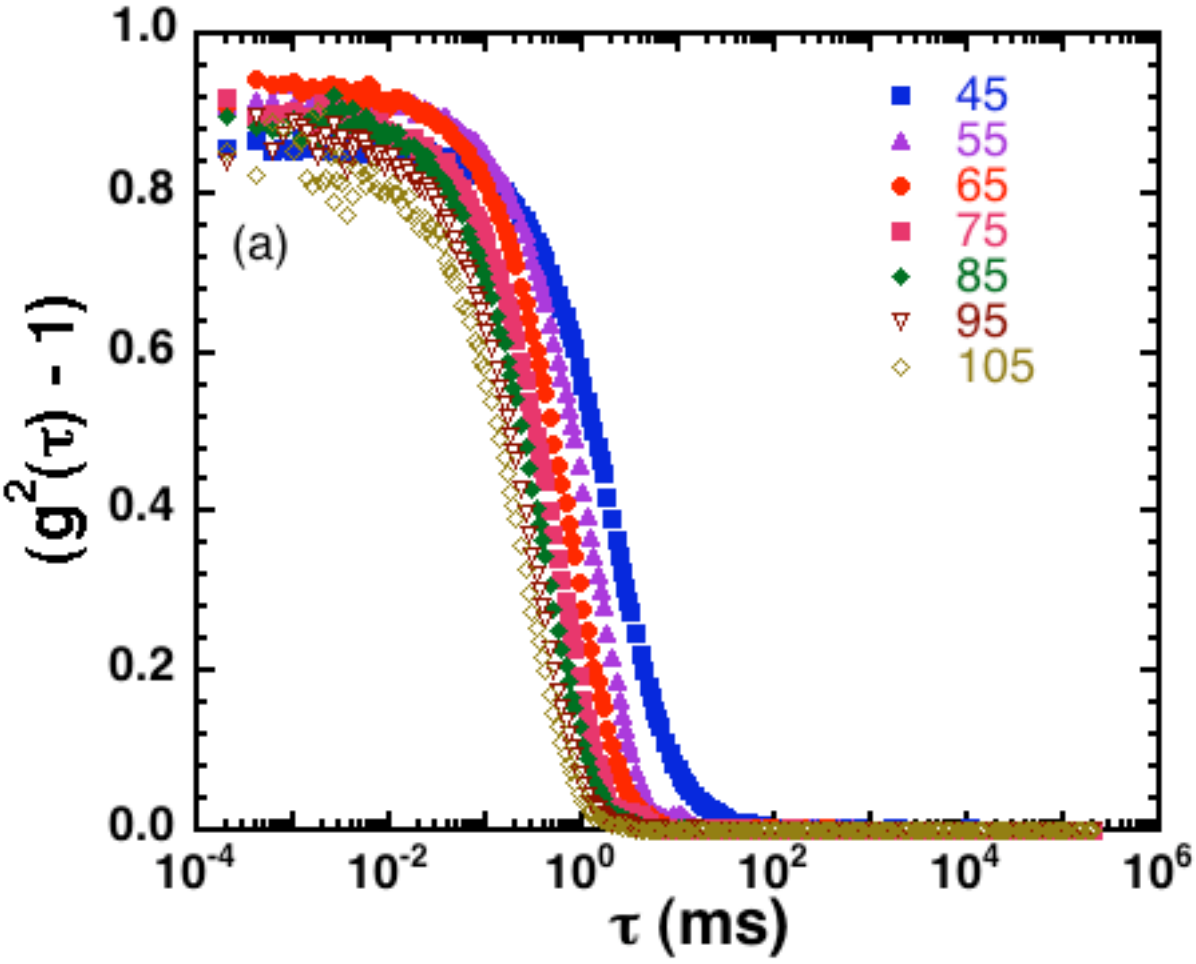

Figure 2.3: Intensity autocorrelation function $g_2(\tau)$ for 20 ppm ($c/c^* \sim 0.03$) PEO WSR-301 as a function of scattering angle, q.

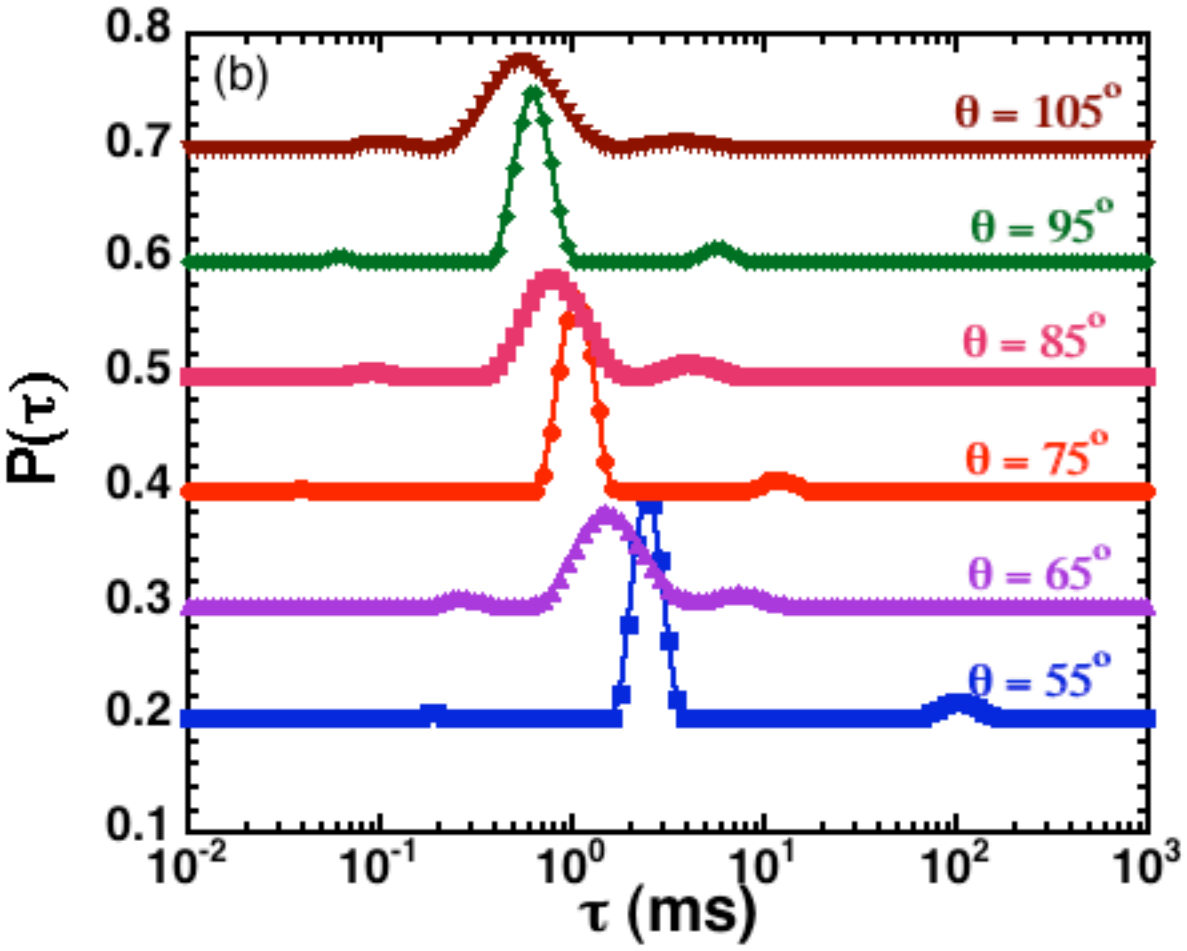

Figure 2.4: Probability distribution function of the DLS decay time spectrum for 20 ppm PEO WSR-301, obtained from CONTIN deconvolution of $g_2(\tau)$ reported in Fig. 2.3.

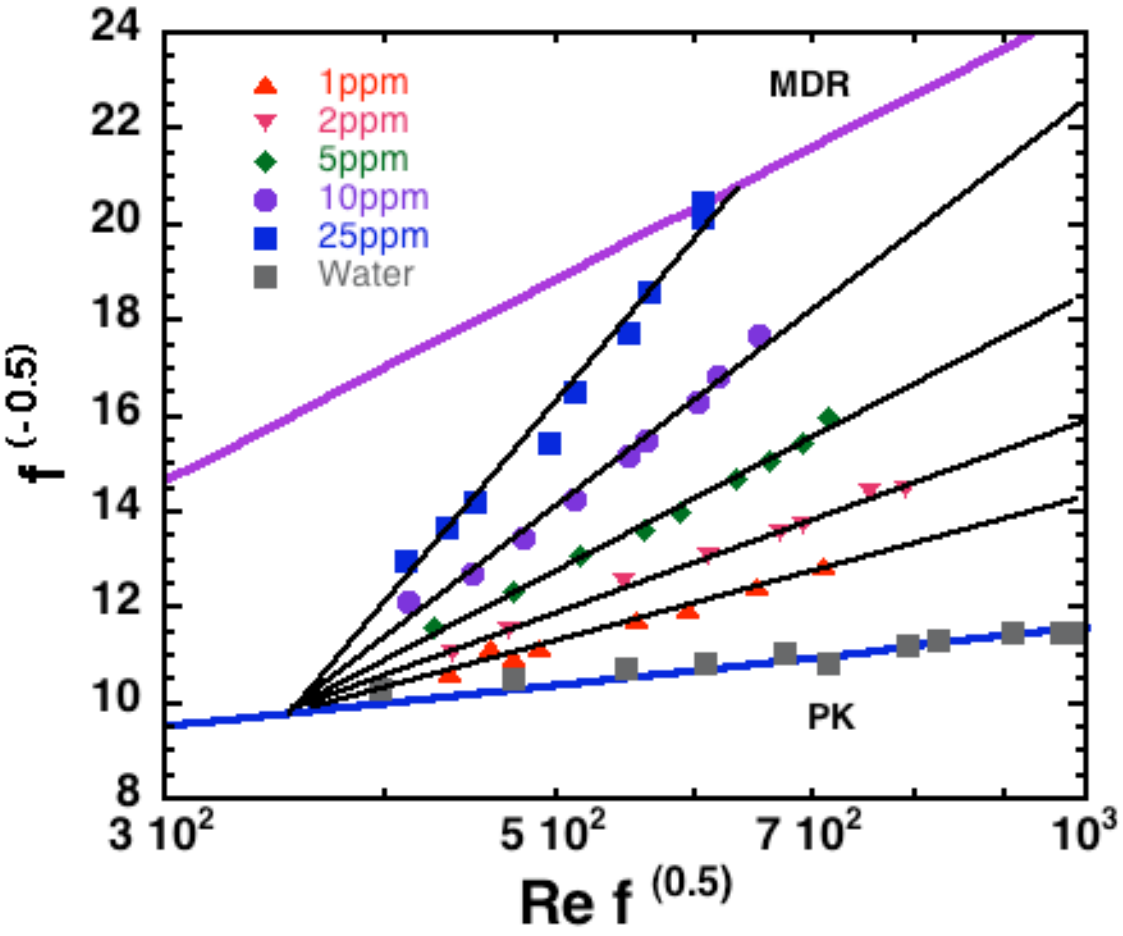

Figure 2.5: Prandtl-von Karman plots for different PEO WSR-301 concentrations ranging from 1-25 ppm. As discussed in the text, the lower curve is the Prandtl-Karman (PK) law for a Newtonian solvent and the upper curve is the maximum drag reduction asymptote for polymer turbulent drag reduction.

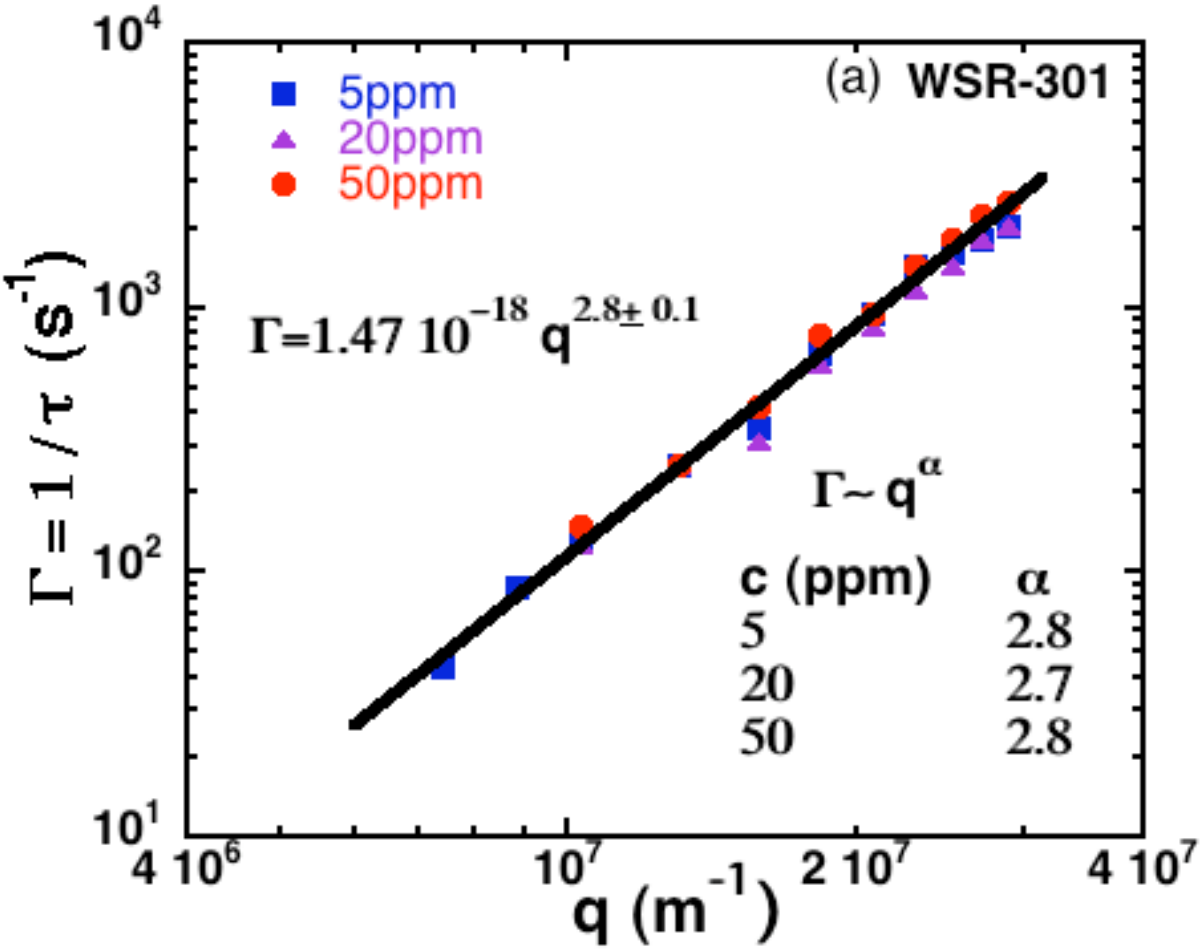

Figure 2.6: Peak relaxation rate, Γ, from CONTIN deconvolution as a function of the scattering vector q for different dilute concentrations (5-50 ppm) of PEO WSR-301.

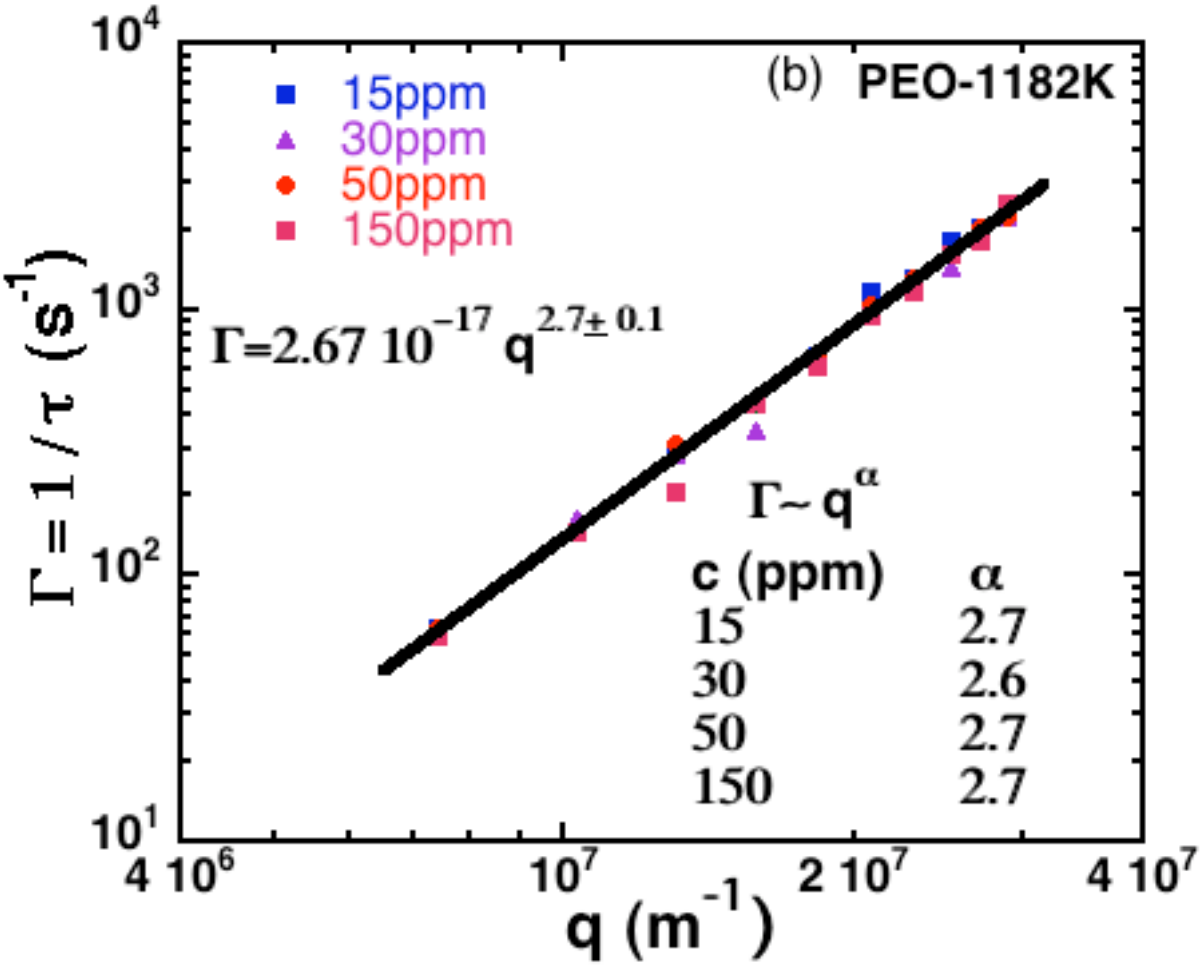

Figure 2.7: Peak relaxation rate, Γ, from CONTIN deconvolution as a function of the scattering vector q for different dilute concentrations (15-150ppm) of monodisperse PEO-1182K (M_w ~ 1.2 x 10^6 g/mole, M_w/M_n~1.12).

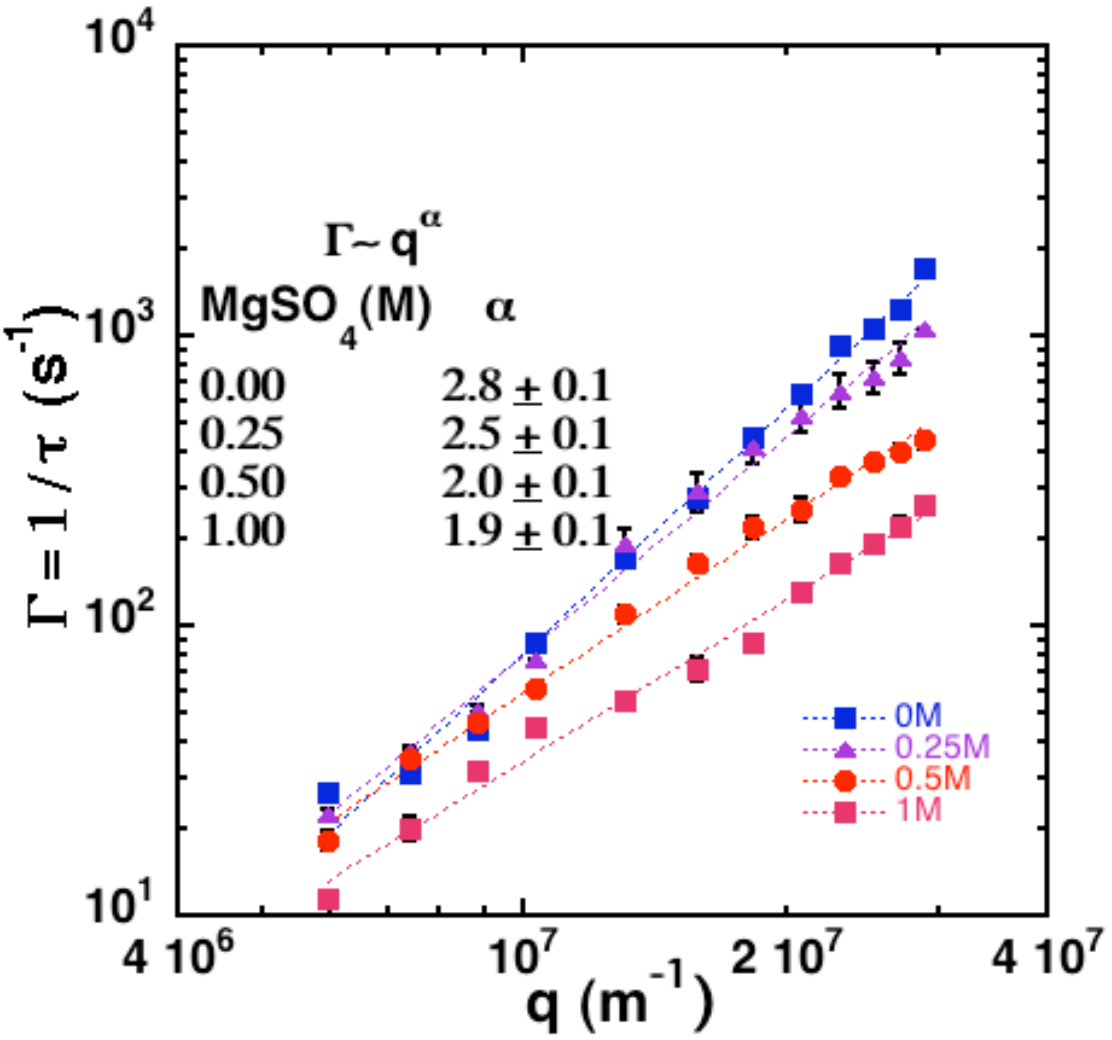

Figure 2.8: The effect of $MgSO_4$ concentration on the q-dependence of the peak relaxation rate Γ at 5 ppm for PEO WSR-301.

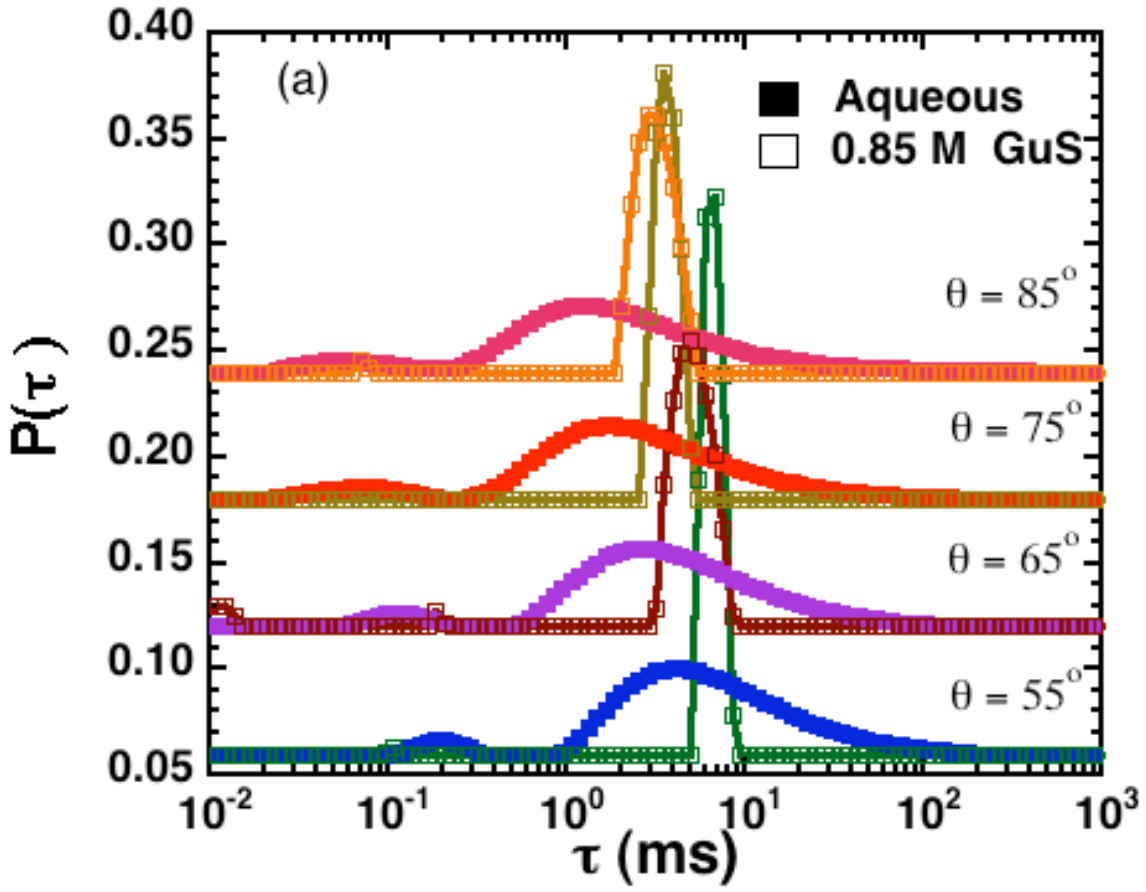

Figure 2.9: Comparison of the DLS decay time spectrum for 150 ppm monodispersed PEO-1182K (M_w ~ 1.2 x 10^6 g/mole, M_w/M_n~1.12) in deionized water (aqueous) and with guanidine sulfate salt (0.85M GuS) at different scattering angles.

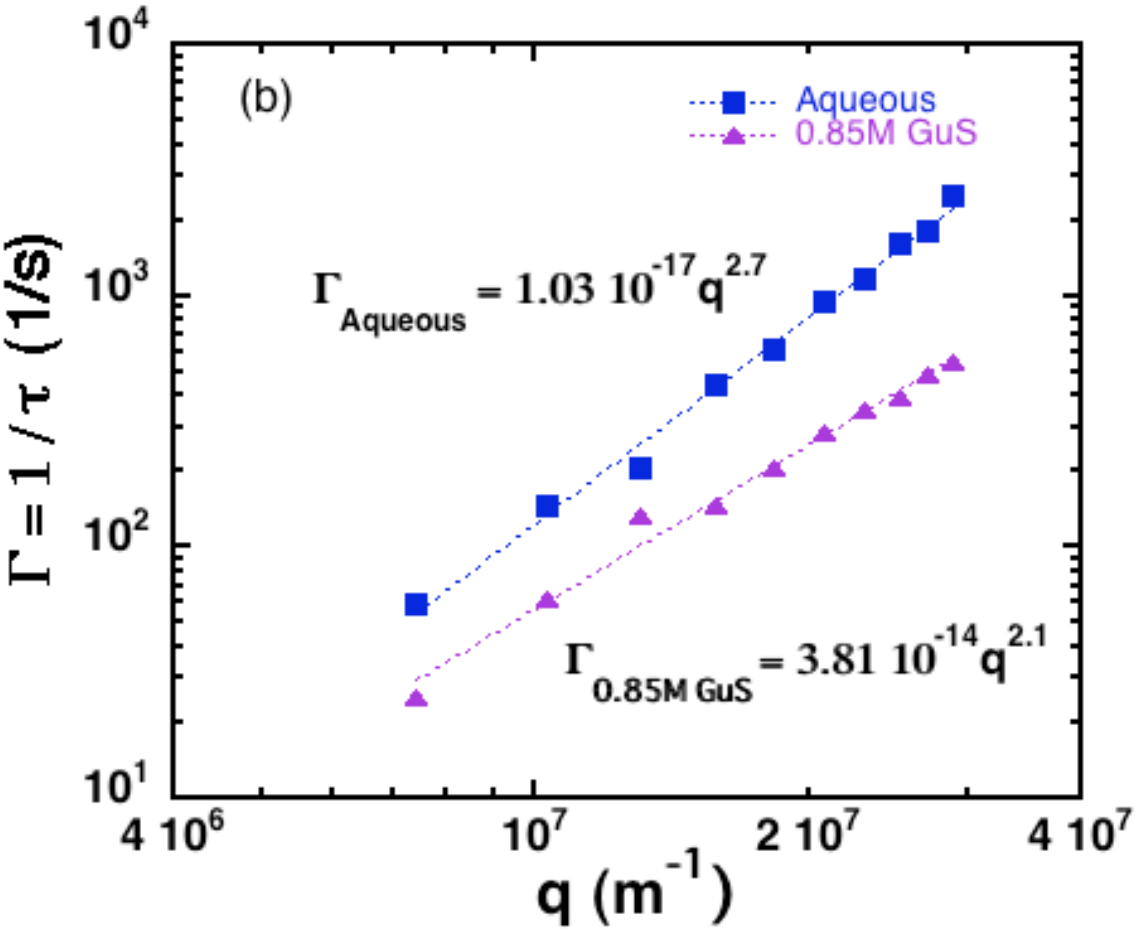

Figure 2.10: Peak decay relaxation rate, Γ, as a function of q for the deionized water (aqueous) and guanidine sulfate salt (0.85M GuS) case (150 ppm monodisperse PEO-1182K).

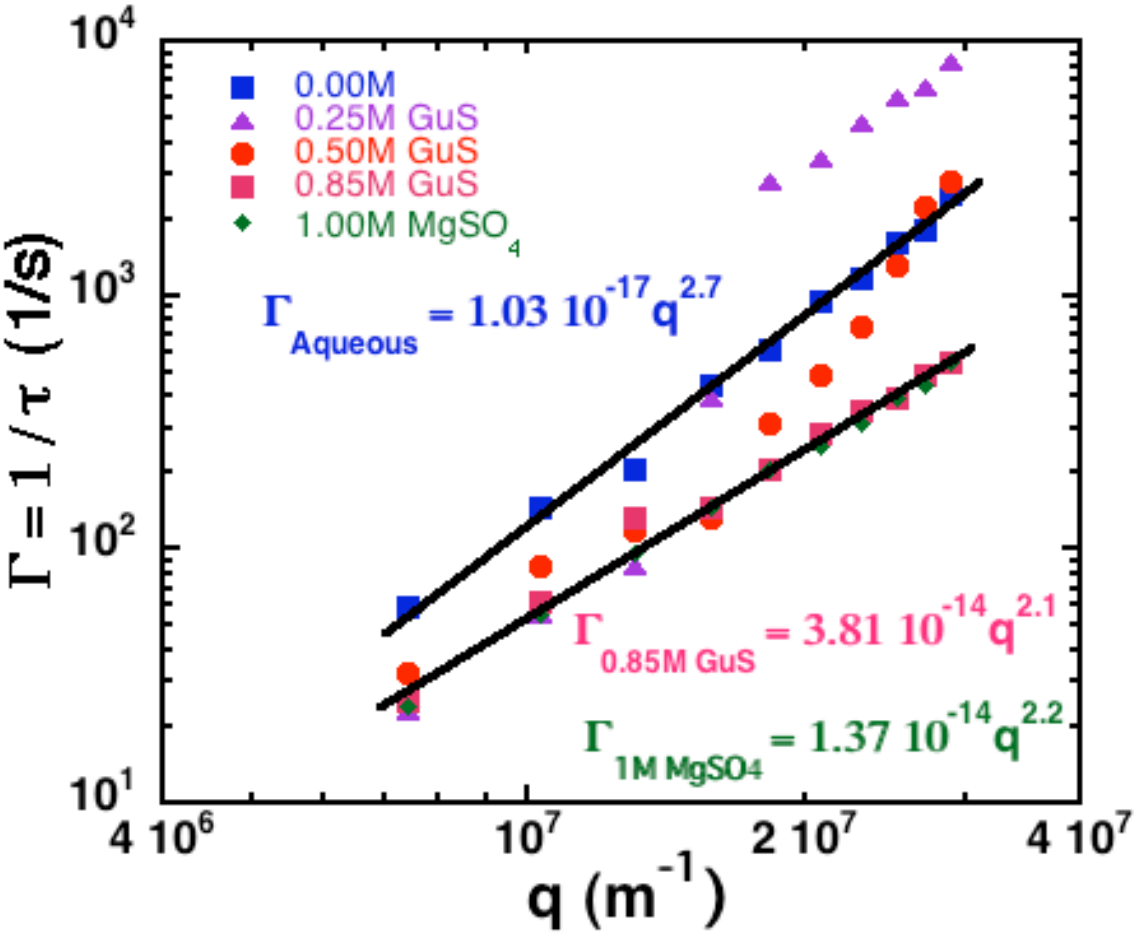

Figure 2.11: Effect of guanidine sulfate salt (GuS) concentration and 1M magnesium sulfate ($MgSO_4$) on the q-dependence of Γ for monodisperse aqueous PEO-1182K (150 ppm).

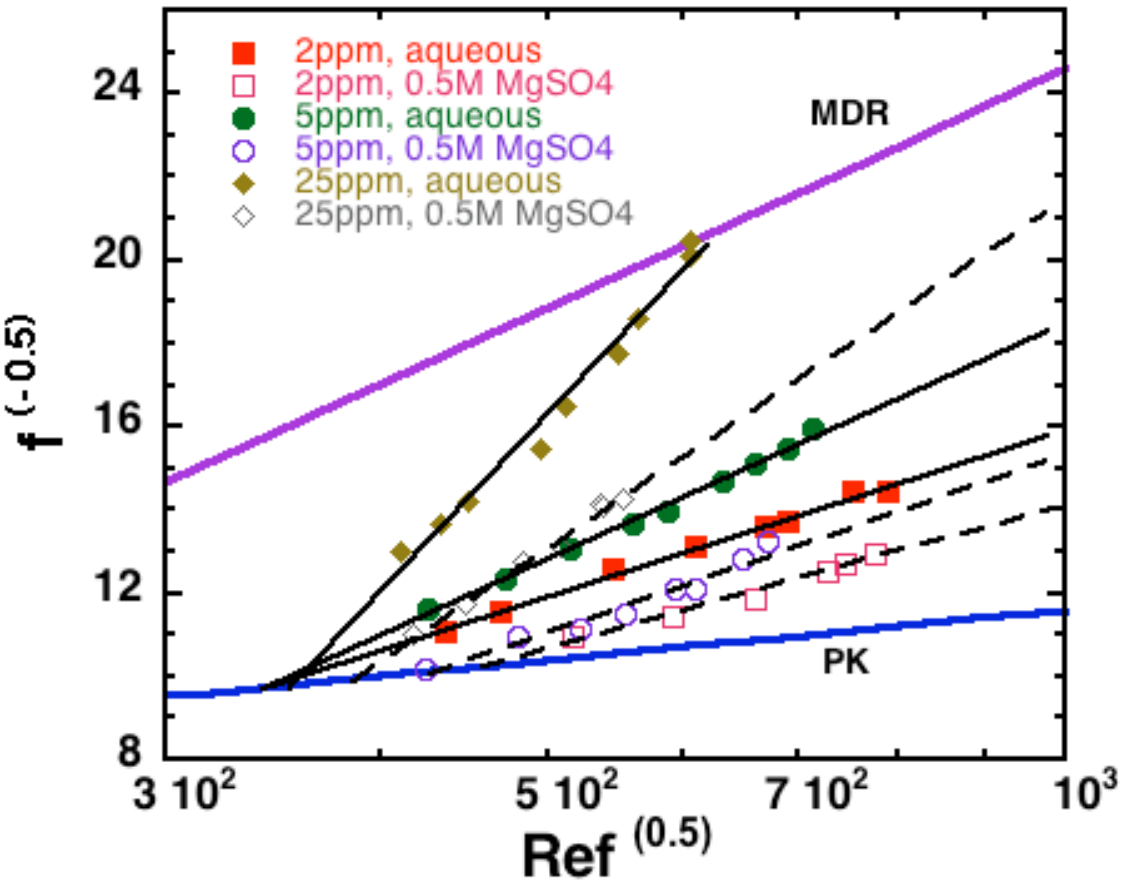

Figure 2.12: Effect of magnesium sulfate (0.5M $MgSO_4$) addition on the turbulent drag reduction behavior of dilute PEO WSR-301 solutions.

.

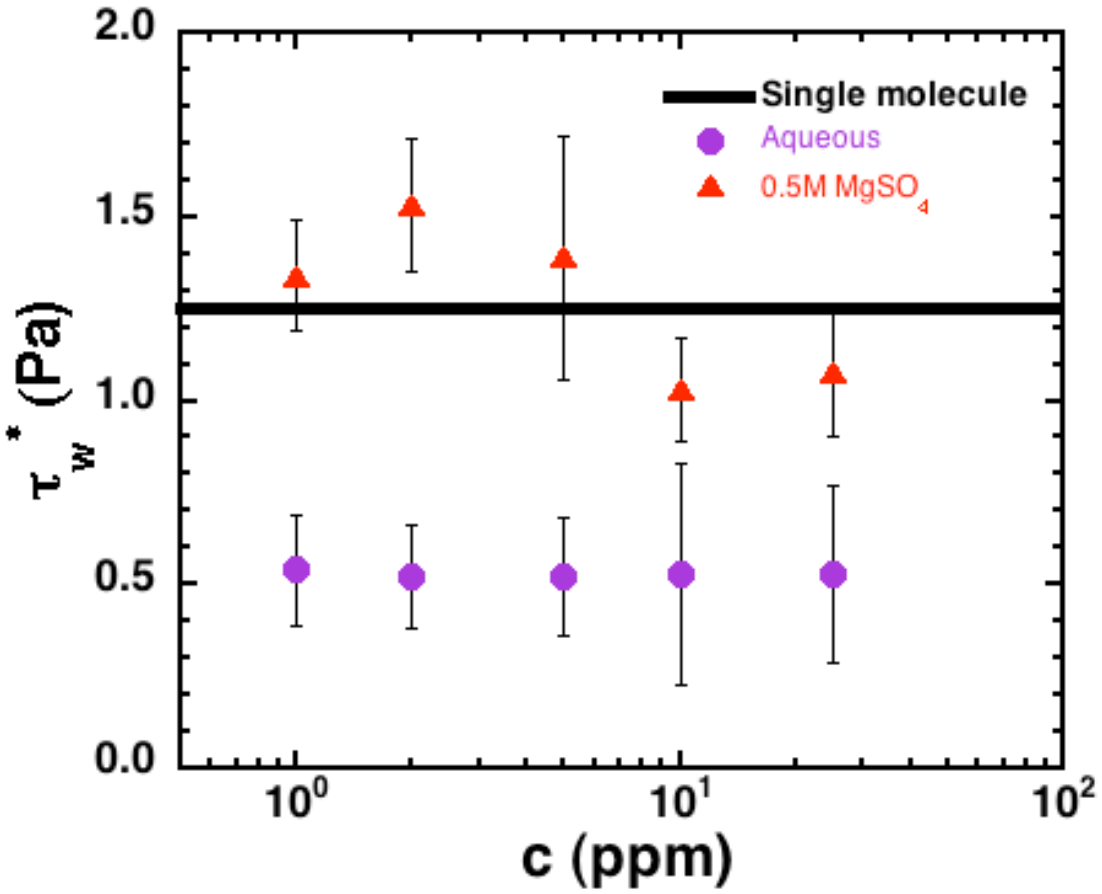

Figure 2.13: Comparison of the onset wall shear stress for turbulent drag reduction, τ_w^*, for WSR 301 with 0.5 M $MgSO_4$ and in pure aqueous solution. The horizontal line is the onset stress prediction given by Virk for PEO, based on single molecule physics, computed as discussed in the text.

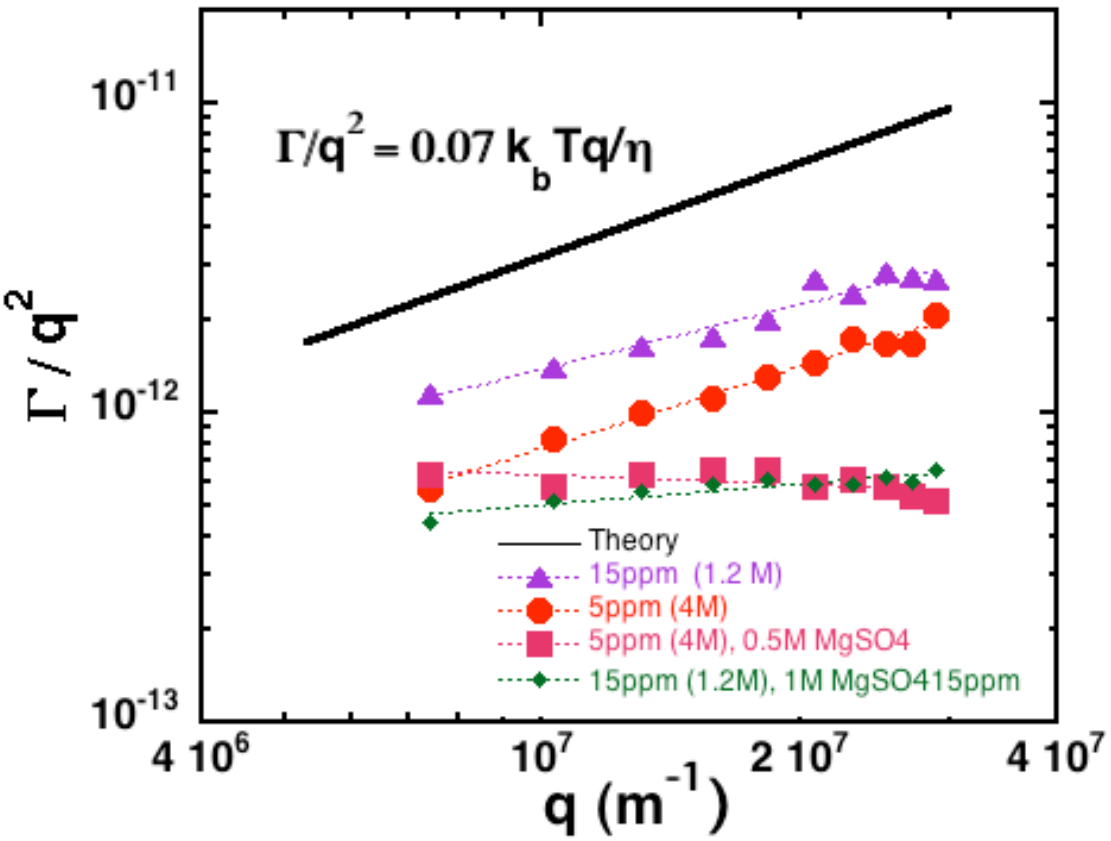

Figure 2.14: Summary of DLS results, plotted as Γ/q^2 to emphasize the deviation from center-of-mass diffusion, for the two polymers and salts studied. The curve is the theoretical prediction for a Gaussian coil[52].

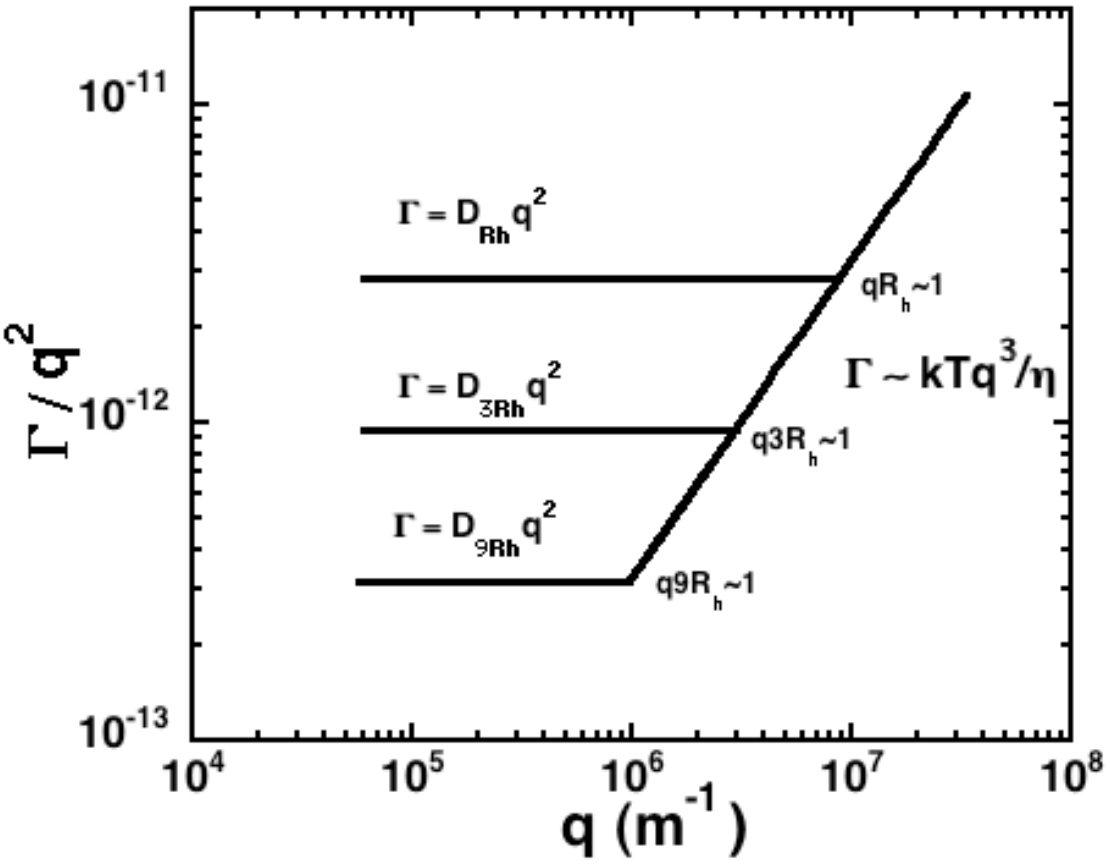

Figure 2.15: Schematic illustration of the hypothesis that small scattering angle DLS measurements of PEO would yield a characterization of the size of the aggregates observed in this study.

Concentration (ppm) WSR-301	Onset Stress, τ_w* (Aqueous)	Onset Stress, τ_w* (0.5 M $MgSO_{4)}$	Slope increment, δ (Aqueous)	Slope increment, δ (0.5 M $MgSO_{4)}$
1	0.54±0.15	1.34±0.15	9.9	8.4
2	0.52±0.14	1.53±0.18	13.4	11.4
5	0.52±0.16	1.39±0.33	19	14.6
10	0.53±0.3	1.03±0.14	28.1	18.2
25	0.53±0.24	1.08±0.18	44	28

Table 2.1: Onset stress (τ_w*) and slope increment (δ) values obtained from drag reduction measurements for the different polymer and salt concentrations used in the study.

.

2.7 References

1. Baghdadi, H. A.; Sardinha, H.; Bhatia, S. R. *Journal of Polymer Science Part B-Polymer Physics* **2005,** 43, (2), 233-240.

2. Morgan, S. E.; McCormick, C. L. *Progress in Polymer Science* **1990,** 15, (1), 103-145.

3. Gil, E. S.; Hudson, S. A. *Progress in Polymer Science* **2004,** 29, (12), 1173-1222.

4. Figueredo, R. C. R.; Sabadini, E. *Colloids and Surfaces a-Physicochemical and Engineering Aspects* **2003,** 215, (1-3), 77-86.

5. Kauser, N.; Dos Santos, L.; Delgado, M.; Muller, A. J.; Saez, A. E. *Journal of Applied Polymer Science* **1999,** 72, (6), 783-795.

6. Rodriguez, S.; Romero, C.; Sargenti, M. L.; Muller, A. J.; Saez, A. E.; Odell, J. A. *Journal of Non-Newtonian Fluid Mechanics* **1993,** 49, (1), 63-85.

7. Addai-Mensah, J.; Yeap, K. Y.; McFarlane, A. J. *Powder Technology* **2007,** 179, (1-2), 79-83.

8. Toryanik, A. I. *Journal of Structural Chemistry* **1984,** 25, (3), 385-388.

9. Dormidontova, E. E. *Macromolecules* **2002,** 35, (3), 987-1001.

10. Straziel.C. *Makromolekulare Chemie-Macromolecular Chemistry and Physics* **1968,** 119, (DEC), 50-63.

11. Saeki, S.; Kuwahara, N.; Nakata, M.; Kaneko, M. *Polymer* **1976,** 17, (8), 685-689.

12. Malcolm, G. N.; Rowlinson, J. S. *Transactions of the Faraday Society* **1957,** 53, (7), 921-931.

13. Dormidontova, E. E. *Macromolecules* **2004,** 37, (20), 7747-7761.

14. Smith, G. D.; Bedrov, D.; Borodin, O. *Physical Review Letters* **2000,** 85, (26), 5583.

15. Tasaki, K. *Journal of the American Chemical Society* **1996,** 118, (35), 8459-8469.

16. Polverari, M.; vandeVen, T. G. M. *Journal of Physical Chemistry* **1996,** 100, (32), 13687-13695.

17. Kalashnikov, V. N. *Journal of Polymer Science Part B-Polymer Physics* **1999,** 37, (22), 3208-3216.

18. Cunibert.C; Ferrando, R. *Polymer* **1972,** 13, (8), 379-382.

19. Hammouda, B.; Ho, D.; Kline, S. *Macromolecules* **2002,** 35, (22), 8578-8585.

20. Cuniberti, C. *Polymer* **1975,** 16, (4), 306-307.

21. Duval, M.; Sarazin, D. *Polymer* **2000,** 41, (7), 2711-2716.

22. Berne, B. J.; Pecora, R., *Dynamic Light Scattering*. J Wiley, New York: 1976.

23. Polik, W. F.; Burchard, W. *Macromolecules* **1983,** 16, (6), 978-982.

24. McIntyre, D.; Gornick, F., *Light scattering from dilute polymer solutions.* Gordon and Breach Science publishers, New York: 1964.

25. Hammouda, B.; Ho, D. L.; Kline, S. *Macromolecules* **2004,** 37, (18), 6932-6937.

26. Vlassopoulos, D.; Schowalter, W. R. *Journal of Rheology* **1994,** 38, (5), 1427-1446.

27. Kalashnikov, V. N. *Journal of Rheology* **1994,** 38, (5), 1385-1403.

28. Tirtaatmadja, V.; McKinley, G. H.; Cooper-White, J. J. *Physics of Fluids* **2006,** 18, (4), 043101.

29. Purnode, B.; Crochet, M. J. *Journal of Non-Newtonian Fluid Mechanics* **1998,** 77, (1-2), 1-20.

30. Choi, H. J.; Jhon, M. S. *Industrial & Engineering Chemistry Research* **1996,** 35, (9), 2993-2998.

31. Berman, N. S. *Annual Review of Fluid Mechanics* **1978,** 10, 47-64.

32. Berman, N. S. *Physics of Fluids* **1977,** 20, (5), 715-718.

33. White, C. M.; Mungal, M. G. *Annual Review of Fluid Mechanics* **2008,** 40, 235-256.

34. Larson, R. G. *Journal of Rheology* **2005,** 49, (1), 1-70.

35. Virk, P. S. *Aiche Journal* **1975,** 21, (4), 625-656.

36. Dunlop, E. H.; Cox, L. R. *Physics of Fluids* **1977,** 20, (10), S203-S213.

37. Vlachogiannis, M.; Liberatore, M. W.; McHugh, A. J.; Hanratty, T. J. *Physics of Fluids* **2003,** 15, (12), 3786-3794.

38. Liberatore, M. W.; Baik, S.; McHugh, A. J.; Hanratty, T. J. *Journal of Non-Newtonian Fluid Mechanics* **2004,** 123, (2-3), 175-183.

39. Liberatore, M. W.; Pollauf, E. J.; McHugh, A. J. *Journal of Non-Newtonian Fluid Mechanics* **2003,** 113, (2-3), 193-208.

40. Liberatore, M. W.; McHugh, A. J. *Journal of Non-Newtonian Fluid Mechanics* **2005,** 132, (1-3), 45-52.

41. Shin, M.; Shaqfeh, E. S. G. *Centre for Turbulence Research: Annual Research Briefs* **2005,** 389.

42. Little, R. C. *Journal of Applied Polymer Science* **1971,** 15, (12), 3117-3125.

43. Little, R. C.; Patterso.Rl. *Journal of Applied Polymer Science* **1974,** 18, (5), 1529-1539.

44. Yuan, G. C.; Wang, X. H.; Han, C. C.; Wu, C. *Macromolecules* **2006,** 39, (18), 6207-6209.

45. Lim, S. T.; Hong, C. H.; Choi, H. J.; Lai, P. Y.; Chan, C. K. *Epl* **2007,** 80, (5).

46. Boom, R.; Sol, C. J. A.; Salimans, M. M. M.; Jansen, C. L.; Wertheimvandillen, P. M. E.; Vandernoordaa, J. *Journal of Clinical Microbiology* **1990,** 28, (3), 495-503.

47. Provencher, S. W. *Computer Physics Communications* **1982,** 27, (3), 229-242.

48. Vanapalli, S. A.; Islam, M. T.; Solomon, M. J. *Physics of Fluids* **2005,** 17, (9), 095108.

49. Draad, A. A.; Kuiken, G. D. C.; Nieuwstadt, F. T. M. *Journal of Fluid Mechanics* **1998,** 377, 267-312.

50. McKeon, B. J.; Smits, A. J. *Measurement Science & Technology* **2002,** 13, (10), 1608-1614.

51. Devanand, K.; Selser, J. C. *Macromolecules* **1991,** 24, (22), 5943-5947.

52. Adam, M.; Delsanti, M. *Macromolecules* **1977,** 10, (6), 1229-1237.

53. Sun, T.; King, H. E. *Macromolecules* **1996,** 29, (9), 3175-3181.

54. Amis, E. J.; Han, C. C. *Polymer* **1982,** 23, (10), 1403-1406.

55. Eisele, M.; Burchard, W. *Macromolecules* **1984,** 17, (8), 1636-1638.

56. Rubinstein, M.; Colby, R. H., *Polymer Physics*. Oxford University Press: 2004.

57. Sureshkumar, R.; Beris, A. N.; Handler, R. A. *Physics of Fluids* **1997,** 9, (3), 743-755.

58. Sreenivasan, K. R.; White, C. M. *Journal of Fluid Mechanics* **2000,** 409, 149-164.

59. Dimitropoulos, C. D.; Sureshkumar, R.; Beris, A. N. *Journal of Non-Newtonian Fluid Mechanics* **1998,** 79, (2-3), 433-468.

60. Ho, D. L.; Hammouda, B.; Kline, S. R. *Journal of Polymer Science Part B-Polymer Physics* **2003,** 41, (1), 135-138.

61. Horn, A. F. *Nature* **1984,** 312, (5990), 140-141.

62. Elbing, B. R.; Winkel, E. S.; Solomon, M. J.; Ceccio, S. L. *Experiments in Fluids* **2008,** 47, (6), 1033-1044.

63. Vanapalli, S. A.; Ceccio, S. L.; Solomon, M. J. *Proceedings of the National Academy of Sciences of the United States of America* **2006,** 103, (45), 16660-16665.

64. Cipelletti, L.; Weitz, D. A. *Review of Scientific Instruments* **1999,** 70, (8), 3214-3221.

65. Ferri, F. *Review of Scientific Instruments* **1997,** 68, (6), 2265-2274.

CHAPTER 3
MULTI-ANGLE DEPOLARIZED DYNAMIC LIGHT SCATTERING OF SHORT FUNCTIONALIZED SINGLE-WALLED CARBON NANOTUBES

3.1 Chapter Summary

Here we introduce the method of multi-angle depolarized dynamic light scattering (MA-DDLS) to characterize the length and diameter of covalently functionalized single-walled carbon nanotubes (SWCNTs). MA-DDLS yields simultaneous characterization of the mean translational and rotational diffusivities of dilute solutions of SWCNTs. Using an anisotropic rigid rod model, we uniquely determine the length and diameter of the SWCNTs from the independent measurements of rotational and translational diffusion. The multi-angle depolarized light scattering technique is found to be a fast, non-invasive and reproducible method for identifying the average length and diameter of SWCNTs in solution.

3.2 Introduction

Carbon nanotubes (CNTs) have attracted tremendous attention over the past decade due to their potential applications in areas ranging from sensors[1-5], coatings[6-8], molecular nanoelectronic devices[9, 10], reinforced composite materials[11] and heat transfer media[12, 13] to biological applications like drug delivery[14], molecular markers[15] and probes[16]. Steps necessary for such applications, including processing and purification of carbon nanotubes (CNTs), as well as final device fabrication/assembly often involve the dispersion or solubilization of CNTs in a variety of solvents[17]. Most often, applications demand the control of length and diameter of nanotubes as they are critical for the wide tuning of electrical[18], mechanical[11] and optical properties[19] of CNTs. In addition, dimensions of nanotubes are critical in predicting the phase behavior and rheology of CNTs in suspensions[20]. Thus, many applications rely on the effective dispersion of CNTs in solution as well as the knowledge of the dimensions of the CNTs at any given state of dispersion[20].

The morphology and microscopic structure of CNTs in solution has been studied by various techniques including small angle neutron scattering[21-26], small angle light scattering[27, 28], ultra small angle X-ray scattering[21, 27, 28] and size exclusion chromotagraphy[29] but there are few techniques which are able to characterize the dimensions of the constituent nanotubes themselves. Currently, direct imaging techniques like transmission electron microscopy (TEM) and atomic force microscopy (AFM) are most commonly used to characterize the average dimensions of carbon nanotubes[30, 31]. Although these measurements are broadly successful, they suffer from certain disadvantages. First, AFM and TEM are ex-situ; a droplet of the CNT solution is dried

typically on a silicon surface or a TEM grid and then imaged. The results obtained thus do not necessarily reflect the in situ morphology and state of aggregation of tubes in solution. In particular, aggregation of the CNTs[32] could cause difficulty in imaging individual tubes. Second, there is a strong possibility of interaction between the sample and the substrate (grid) that can affect aggregation and resolvability. Third, the sample volume that can be probed by TEM or AFM is relatively small. Thus, multiple images are required to generate the good statistics necessary to measure average CNT dimensions. Further, microscopy methods require significant time for characterization with often requiring extensive sample preparation. (For example, imaging 200-2000 rods of a nanotube sample by AFM might require as many as 8-10 hours of instrument time[33].)

In addition to direct imaging methods like microscopy, recently, Parra-Vasquez and coworkers introduced a viscosity-based method for the determination of the length of dilute single walled carbon nanotube (SWCNT) suspensions[33]. Their method relies on analysis of the zero shear viscosities of the SWCNT dispersions. General application of this method in dilute systems requires precise measurement of dispersion viscosities that are only a few percent more than the solvent viscosity[34]**.** Recently, Badaire et al. showed that depolarized dynamic light scattering (DDLS) performed at a single angle could be used to identify the dimensions of carbon nanotubes[35]. The data analysis procedure, involving non-linear fitting of a 3-parameter model, complicates the wide applicability of this method.

In this chapter we introduce a simple and fast method based on DDLS performed at multiple scattering angles (MA-DDLS) to characterize the mean length and diameter of functionalized SWCNTs dispersed in solution. Since the rotational and translational

diffusion display different functional dependencies on rod length and diameter, CNT dimensions can be uniquely determined from these two measurements. The technique provides independent characterization of the rotational and translational diffusion of aqueous dispersions of SWCNTs without the computational complexity of single scattering angle measurements. The method is of broad interest because it reduces the need to perform time-consuming microscopy methods like TEM or AFM. It also yields the dimensions of SWCNTs in solution without the complicating affects of drying and adsorption. This method could be coupled with size exclusion based separation methods designed to fractionate SWCNTs[36].

In this chapter we report the light scattering dynamics of SWCNTs solubilized in water using functionalized groups such as poly(amino benzene sulfonic acid) (PABS) and poly(ethylene glycol) (PEG). These functional moieties attach covalently to the nanotube surface making them soluble in aqueous media. Synthesis of such covalently functionalized, well-dispersed and water-soluble SWCNTs has been reported in the literature previously[37, 38]. In dilute solutions we find that the nanotubes exhibit dynamics consistent with the Brownian motion of a rigid rod. Using an anisotropic rigid rod model we determine the length and diameter of SWCNT from the translational and rotational diffusion coefficient of the SWCNTs measured by DDLS and compare to the results obtained from atomic force microscopy (AFM) measurements.

3.3 Materials and Methods.

3.3.1 Materials

SWCNTs functionalized with PABS and PEG were purchased from Carbon Solutions Inc. and were dispersed in de-ionized water to the required concentrations. The samples

were prepared by dispersing the functionalized nanotube samples using a bath sonicator for 2 hours. Samples were first prepared at a typical concentration of 1 mg/ml and then diluted to test concentrations in the range 0.01 - 0.1 mg/ml. Both PABS and PEG functionalized SWCNTs form stable aqueous dispersions as per ref[39] and our own observations. Therefore a dilute solution of such functionalized tubes are ideal for testing the performance of multi-angle DDLS for characterization of SWNT dimensions.

3.3.2 Depolarized Dynamic Light Scattering of Carbon Nanotubes: Modeling and Experiment

Multi-angle polarized (VV) and depolarized (VH) dynamic light scattering were performed on a compact goniometer (ALV, Langen, Germany) equipped with a multi-tau digital correlator (ALV-5000E, Langen, Germany). The addition of a Glan-Thompson prism polarizer (Newport Corporation), positioned between the sample and the detector, enabled selective collection of either the vertically (polarized scattering, VV) and horizontally (depolarized scattering, VV) polarized light scattering. The minimum delay time of the correlator used was 12.5 ns. The laser source (λ_0= 488 nm, Innova 70C, Coherent Inc., Santa Clara, CA) was vertically polarized. Now as seen in the Chapter 2, dynamic light scattering (DLS) quantifies time-dependent fluctuations of light scattered from a specimen. Because these fluctuations are generated by random motion of the scatterers, diffusion coefficients can be obtained from analysis of the intensity-intensity autocorrelation of the time-dependent scattering, $g_2(q,t) = \langle I(q,t)I(q,0)\rangle / \langle I(q)\rangle^2$ where $q = \frac{4\pi n \sin\left(\frac{\theta}{2}\right)}{\lambda_0}$ is the scattering wave vector. Here n is the refractive index of the solvent (n=1.33 for deionized water), λ_0 is the wavelength of the incident light source, and θ is

the scattering angle. In the dilute limit, the measurement yields the self-diffusivity, which can be converted to an effective hydrodynamic size using the Stokes-Einstein equation[40]. Although in standard DLS only light scattered with polarization parallel to the incident beam is measured (VV scattering), with depolarized dynamic light scattering (DDLS) additional information about rotational diffusion can be obtained if there is anisotropy in the particle's polarizability, as is the case for carbon nanotubes[41]. In DDLS, light scattered with polarization perpendicular to the incident light (VH scattering) is measured. Thus in a DDLS experiment, the polarized (VV), $g_{2,VV}(q,t)$ and depolarized (VH), $g_{2,VH}(q,t)$ intensity autocorrelation functions are independently measured at different scattering angles, q,. Here the polarized (VV), $g_{2,VV}(q,t)$ and depolarized (VH), $g_{2,VH}(q,t)$ intensity autocorrelation functions are defined as follows,

$$g_{2,VV}(q,t) = \langle I_{VV}(q,t)I_{VV}(q,0)\rangle / \langle I_{VV}\rangle^2 \qquad (3\text{-}1a)$$

$$g_{2,VH}(q,t) = \langle I_{VH}(q,t)I_{VH}(q,0)\rangle / \langle I_{VH}\rangle^2 \qquad (3\text{-}1b)$$

I(q,t) is the time-dependent intensity of scattered light and subscripts VV and VH represent polarized and depolarized scattering respectively. q in these expressions denotes that these quantities are angularly dependent. The brackets denote the time-average. All correlation functions were collected for duration at least 1000 times longer than the longest relaxation time of the sample studied. In the dilute limit both $g_{2,VV}(q,t)$ and $g_{2,VH}(q,t)$ are exponentially decaying functions.

$$g_{2,VV}(q,t) = \exp(-2\Gamma_{VV}t) = \exp(-2t/\tau_{VV}) \qquad (3\text{-}2a)$$

$$g_{2,VH}(q,t) = \exp(-2\Gamma_{VH}t) = \exp(-2t/\tau_{VH}) \qquad (3\text{-}2b)$$

Here Γ is the DLS relaxation rate, ($\Gamma=1/\tau$), which is inversely related to the relaxation time (τ) of the sample. Experimental relaxation time distributions were extracted from the

measured $g_{2,VV}(q,t)$ and $g_{2,VH}(q,t)$ by a CONTIN deconvolution of the respective correlation functions. CONTIN is a constrained regularization algorithm widely used to obtain relaxation time information from the intensity autocorrelation function[42].

Using equations 3-2a and 3-2b, relaxation rates can be obtained from polarized (Γ_{VV}) and depolarized (Γ_{VH}) dynamic light scattering for each of the scattering angles studied.

The relaxation rate ($\Gamma=1/\tau$), obtained from polarized (Γ_{VV}) and depolarized (Γ_{VH}) dynamic light scattering are related to the translational (D_t) and rotational (D_r) diffusion coefficient respectively by the simple expressions: [43]

$$\Gamma_{VV} = D_t q^2, \qquad (3\text{-}3)$$

and

$$\Gamma_{VH} = D_t q^2 + 6D_r. \qquad (3\text{-}4)$$

The power of the MA-DDLS method stems from the fact that the VH autocorrelation function for optically anisotropic particles such as carbon nanotubes is sensitive to rotational diffusion, particularly at low scattering vectors q. Eqns. (3-3) and (3-4) are explicitly developed for the case of optically anisotropic rods and assume decoupling of rotational and translational diffusion. Depolarized dynamic light scattering has been well studied in solutions of rigid rod macromolecules[44], colloids[43, 45] and viruses[46]. The origin of these equations and their application to the study of rotational diffusion has been reviewed before[47, 48].

Measurements of the relaxation rate at a range of scattering angles yield both the translational (D_t) and rotational (D_r) diffusivity. Further, D_t and D_r obtained from DDLS are related to the hydrodynamic dimensions of the SWCNTs by slender body theory[49].

For an anisotropic rigid cylindrical rod, the coefficients are given by the simple expressions:

$$D_t = \frac{k_B T}{6\pi\eta_s a}\left[\ln\left(\frac{2a}{b}\right) + \ln 2 - 1\right] \qquad (3\text{-}5)$$

and

$$D_r = \frac{3k_B T}{8\pi\eta_s a^3}\left[\frac{\left(\frac{a}{b}\right)^2 (\ln\left(\frac{a}{b}\right))^2}{\left(\frac{a}{b}\right)^2\left(\ln\left(\frac{a}{b}\right) + \ln 2 - 1\right) + 0.651(\ln\left(\frac{a}{b}\right))^2}\right] \qquad (3\text{-}6)$$

Here a and b are the half-length and half-diameter of the cylinder, k_B is the Boltzmann constant, T is the temperature and η_s is the solvent viscosity.

Because the characterization of D_t and D_r from eqns. 3-5 and 3-6 requires DDLS measurements at several q values, we refer to the method as multi-angle DDLS (MA-DDLS). As we will see, characterization of DDLS at multiple angles yields a simple method, and thereby distinguishes it from the initial results of Badaire et al[35]. To test the MA-DDLS method, PABS and PEG functionalized SWCNT in the concentration range c=0.01-0.1 mg/ml were used.

3.3.3 Atomic Force Microscopy

In order to compare the sizes estimated from DDLS experiments for the nanotubes, we independently characterized the length and diameter of the SWCNTs by Atomic Force Microscopy (AFM). A Nanoscope IIIa phase microscope (Veeco Instruments Inc., Plainview, NY, USA) coupled with a J scanner at a scan speed of 1 Hz was used. A silicon cantilever (NSC15/no Al, MikroMasch, San Jose, CA, USA) with drive frequency f=275.94 Hz probed the sample. The samples were prepared by placing a droplet of the

aqueous dispersions of the carbon nanotubes on a silicon wafer and allowing the sample to dry.

3.4 Experimental Section.

3.4.1 DDLS of dilute functionalized SWNT samples.

Fig. 3.1 shows the experimentally measured polarized (VV) and depolarized (VH) correlation functions, $g_{2,VV}(q,t)$ and $g_{2,VH}(q,t)$ measured at the scattering angles, $\theta=45^0$ ($q=13.09\ \mu m^{-1}$) for the SWNT-PABS samples in the concentration range c=0.01-0.1 mg/ml. The data show that the depolarized correlation function for all the SWCNT dispersions decays faster than the polarized correlation function. This observation is consistent with the functional forms of eqns. 3-3 and 3-4. The inset of Fig. 3-1 shows the relaxation rate distributions obtained by CONTIN[48] deconvolution of the VV and VH correlation functions. The CONTIN analysis yielded a single mode peak in the relaxation spectrum of both polarized and depolarized scattering. Further, the data showed negligible change in the peak value of the CONTIN relaxation spectrum in the concentration range studied with dilution, indicating that these measurements are indeed performed in a dilute regime. Note that the VV relaxation time distributions in the c= 0.1 mg/ml and c=0.025 mg/ml are broad compared to the c=0.01 mg/ml case. Thus, all further measurements on the SWCNT samples reported are at a concentration of c= 0.01 mg/ml where both the VV and VH relaxation peak widths at c= 0.01mg/ml are narrow (half-width relative to peak maximum ~ 5%). This narrow width is a qualitative indication that the samples studied were not aggregated.

As a quantitative test that the specimens were free of aggregates, we studied the effect of adding magnesium chloride ($MgCl_2$) on the polarized relaxation spectra of a

dilute SWCNT solution. Salts like $MgCl_2$ have been used to induce aggregation in monodisperse colloidal rod systems[49]. If our test samples were indeed aggregated, then we would expect similar relaxation spectra to that of samples with $MgCl_2$ added (negative control). Fig. 3-2 shows the effect of the addition of 5mM $MgCl_2$ on the polarized (Γ_{VV}) DLS relaxation rate spectrum of SWCNT-PABS, sequentially after addition of salt. The addition of salt progressively changed the relaxation rate distribution from a strictly monomodal to a more bimodal distribution. The bimodal distribution consists of fast and slow modes, interpreted as the response of individual and aggregated SWCNT rods, respectively.

In Fig. 3.3 we plot the characteristic relaxation times obtained from Fig. 3.2 by CONTIN deconvolution as a function of time. The magnitude of the fast mode relaxation times obtained was time independent. The peak relaxation time of the fast mode is also equal to the relaxation time of a salt free aqueous SWCNT-PABS dispersion (as reported in Fig. 3.1). This agreement implies that the fast relaxation mode can be attributed to the well-dispersed individual rods, as is found in salt-free aqueous SWCNT-PABS dispersions. Fig. 3.3 also clearly reveals that the slow mode progressively grows with time until it reaches a steady state after 70 minutes. The slow mode is clearly an indication of the formation of SWNCT-PABS aggregates in solution. Comparing Figs. 3.1, 3.2 and 3.3 we notice that the salt-free SWCNT solutions show no features of aggregation as observed in the SWCNT solutions with added $MgCl_2$. These data indicate that solutions of SWCNT comprise well-dispersed individual nanotubes. These measurements also indirectly support the efficacy of covalent functionalization as a means to achieve stable dispersion of short SWCNTs. Finally, comparison of MA-DDLS

results against a control experiment with added $MgCl_2$ can serve as a general test of aggregation of functionalized SWCNTs dispersed in aqueous solution.

From eqn. (3-1) and (3-2), both Γ_{VV} and Γ_{VH} are expected to be q-dependent. In order to extract translational and rotational diffusion coefficients of SWCNT samples we linearly extrapolated Γ_{VV} and Γ_{VH} in q^2. Multiple VV and VH measurements were performed on dilute SWCNT-PABS and SWCNT-PEG samples over the angular range $\theta=45^0$-115^0 (13.09 μm^{-1} < q < 28.86 μm^{-1}). In Fig. 3.4 we report the VV and VH correlation functions for a SWCNT-PABS sample studied at these scattering angles. The inset of Fig. 3.4 reports the probability distribution function of the CONTIN relaxation time spectrum for both VV and VH correlation functions. Similar results were obtained with SWCNT-PEG dispersions (data not shown).

In anticipation of data reduction as per eqns. (3-3) and (3-4) the relaxation rates, Γ_{VV} and Γ_{VH} from both SWCNT-PABS and SWCNT-PEG were plotted as a function of q^2 in Fig. 3.5. The slope of Γ_{VV} versus q^2 corresponds to the translational diffusion coefficient of the SWCNTs in solution. The intercept of the plot of Γ_{VH} versus q^2 is six times the rotational diffusion coefficient of the SWCNTs, as per eqn 3-4. Linear fits to the data were used to estimate the rotational and translational coefficients of the samples. Table 1 reports the translational and rotational diffusion coefficient values for both the SWCNT-PABS and SWCNT-PEG samples. Errors reported in the table are the standard error of the mean of three independent measurements for each sample. From equations (3-3) and (3-4) the rotational diffusion coefficients are D_r, PABS = 44 ± 9 s^{-1} and $D_{r,\,PEG}$ = 170 ± 5 s^{-1} and the translational diffusion coefficients are $D_{t,\,PABS}$ = 3.58 ± 0.03 $\mu m^2/s$ and $D_{t,\,PEG}$ = 4.09 ± 0.03 $\mu m^2/s$ for SWCNT-PABS and SWCNT-PEG samples respectively.

Using eqns (3-1)-(3-4), we computed the length and diameter of the SWCNTs consistent with the two independent measurements of D_r and D_t. We find that the SWCNT-PABS sample has an average length of 949±70 nm and an average diameter of 0.8±0.3 nm. The SWCNT-PEG sample has an average length of 541±6 nm and an average diameter of 4.4±0.2 nm. Table 1 also reports the sensitivity of the slender body theory (eqns 3-5 and 3-6) in estimating the length and diameter of the SWCNT-PABS and SWCNT-PEG samples from the experimentally measured translational and rotational diffusion coefficients. Diameter estimation is a factor of five times more sensitive than length estimation.

3.4.2 Atomic force microscopy.

For comparison with the results obtained from DDLS, we also performed AFM studies on the diluted CNTs samples as shown in Fig. 3.6a and 3.6b. These figures show thin films of dried SWCNT-PEG and SWCNT-PABS samples, respectively, used for statistical analysis of average SWCNT dimensions. We measured the average length of 50 nanotubes from the SWCNT-PEG system to be 458 ± 29 nm and average length from the SWCNT-PABS system to be 408 ± 50 nm. (Uncertainties in the measurements correspond to the standard error of the mean of the measurements from 50 SWCNTs. The diameters of the SWCNTs were measured using the height profile registered during acquisition of the AFM image.) The average diameter of the SWCNT-PEG system was 6.8 ± 0.7 nm and average diameter of the SWCNT-PABS system was 8.4 ± 0.8 nm. The diameters of the SWCNTs were measured using the height profile registered during acquisition of the AFM image.) The average diameter of the SWCNT-PEG system was 6.8 ± 0.7 nm and average diameter of the SWCNT-PABS system was 8.4 ± 0.8 nm. The

statistical distributions of the dimensions of the carbon nanotubes are shown in the histogram plot of Fig. 3-6c-f.

Although the AFM and MA-DDLS derived dimensions agree qualitatively, there are quantitative differences between the methods especially for the result obtained for SWCNT-PABS. In this case, the lengths of the SWCNT-PABS measured by AFM are up to a factor of 2 larger and the diameters are up to a factor of 4 larger than the dimensions reported for solutions of the same SWCNTs as measured by MA-DDLS.

Other methods have also found quantitative disagreement between AFM and bulk solution characterization methods. For example, Parra-Vasquez and coworkers compared viscosity-based measurements of the length of nanotubes to results obtained from AFM[33]. They reported differences in the lengths of the nanotubes of up to 30% between independently prepared samples. They also found that relative to their viscosity-based characterization of the nanotube length, AFM was dependent on sample preparation, sample sizes and wafer surfaces. Their finding is consistent with our results that the dimensions measured by AFM differ from the measurements of the nanotube dimensions by MA-DDLS. Reasons for the discrepancy between solution based methods like MA-DDLS and microscopy methods such as AFM might include the following: First, AFM measurements were done at much higher concentrations when compared to MA-DDLS measurements (to sample enough SWCNTs for statistical analysis). Higher concentrations might promote aggregation that would interfere with the single tube characterization that is of interest here. Second, AFM requires dry films of the CNT suspensions. Drying of the suspensions might induce complications such as aggregation and bundling in the CNTs. These reasons likely contribute to the observation apparent in Table 3.1, that the relative error in the MA-DDLS characterization is less than that observed for the AFM studies.

3.5 Conclusion

To conclude, we discuss bounds of applicability of the MA-DDLS method and thereby explore its scope for broader application. First, the data analysis procedure used assumes that the SWCNTs are rigid. Recent work of Duggal et al. suggests that SWCNTs up to about 1 μm in length can be treated as rigid[50]. (For longer rods, adaptation of eqns. 3-5 and 3-6 to include the effects of finite flexibility would be feasible.) Second, the theoretical framework of MA-DDLS assumes that the SWCNT are subject to Brownian motion. As the SWCNTs become longer, or for the case of multi-walled tubes, the system would likely crossover into a limit for which the CNT dynamics would not be significantly affected by Brownian motion. However, from previous studies of colloidal rod rotational diffusion, the rod length required to reach this non-Brownian limit would be no less than about 4 μm[51]. Third, the nanotubes must not be so small that additional higher order relaxation modes appear in the DLS correlation functions[52]. From literature work, this limit imposes the constraint $qL <\sim 10$. For the angular range of typical wide-angle light scattering devices, we thus conclude that the SWCNT tube length ought to be $L \sim 300$ nm or greater. Thus, the MA-DDLS method is appropriate for the rapid characterization of SWCNT dimensions for tubes of length in the approximate range 300 nm < L < 4 μm. This range is consistent with the dimensions of SWCNTs of interest for many different applications, including sensing[1], conduction[53] and molecular marking[15]. Thus, we have shown that multi-angle DDLS is a simple, non-invasive tool to determine the average length and diameter of SWCNT. The length and diameter of the nanotubes are determined from the translational and rotational diffusion coefficient measurements, with considerable advantages relative to other sizing techniques.

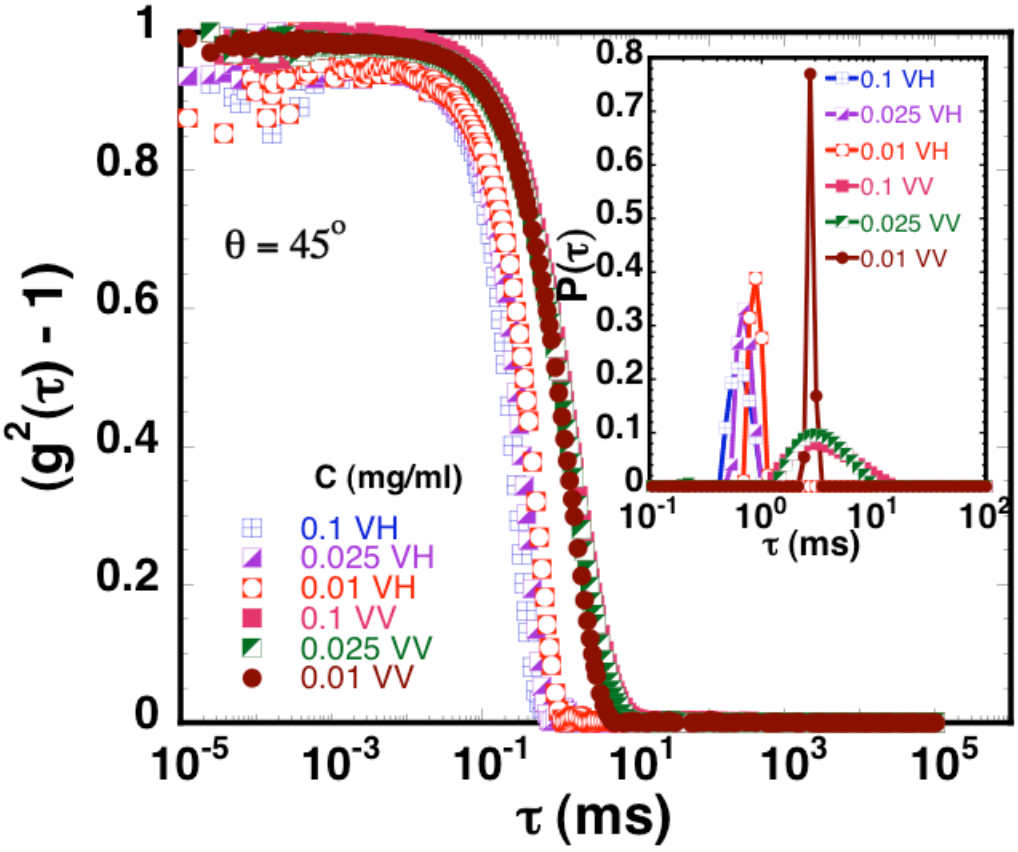

Figure 3.1: Comparison of the polarized (VV) and depolarized (VH) intensity autocorrelation functions $g_2(\tau)$ of SWCNT-PABS in the concentration range c=0.01-0.1 mg/ml at scattering angle, θ=45°. The inset plot shows the probability distribution function of the DLS decay time spectrum in the VV and VH scattering planes for the above concentrations, obtained from a CONTIN deconvolution of $g_2(\tau)$.

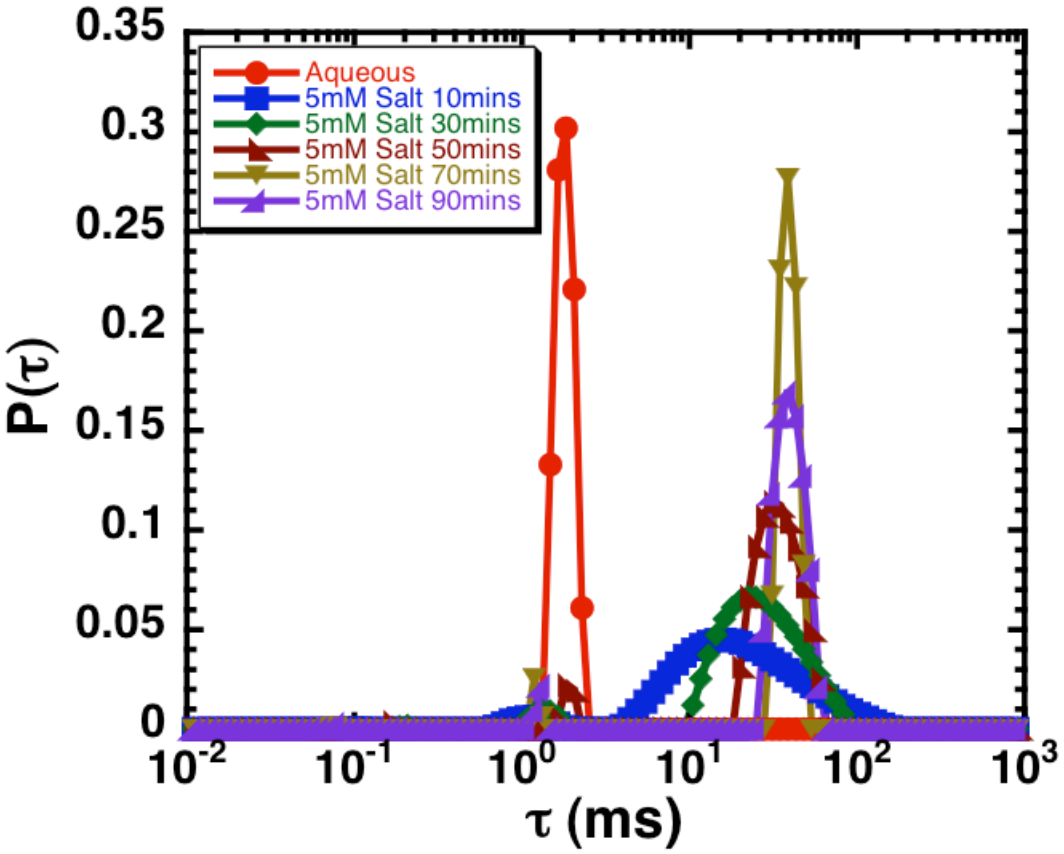

Figure 3.2: Comparison of the DLS decay time spectrum of c=0.01 mg/ml of SWCNT-PABS in deionized water (aqueous) and with magnesium chloride salt (5mM $MgCl_2$) at θ=45° as a function of time.

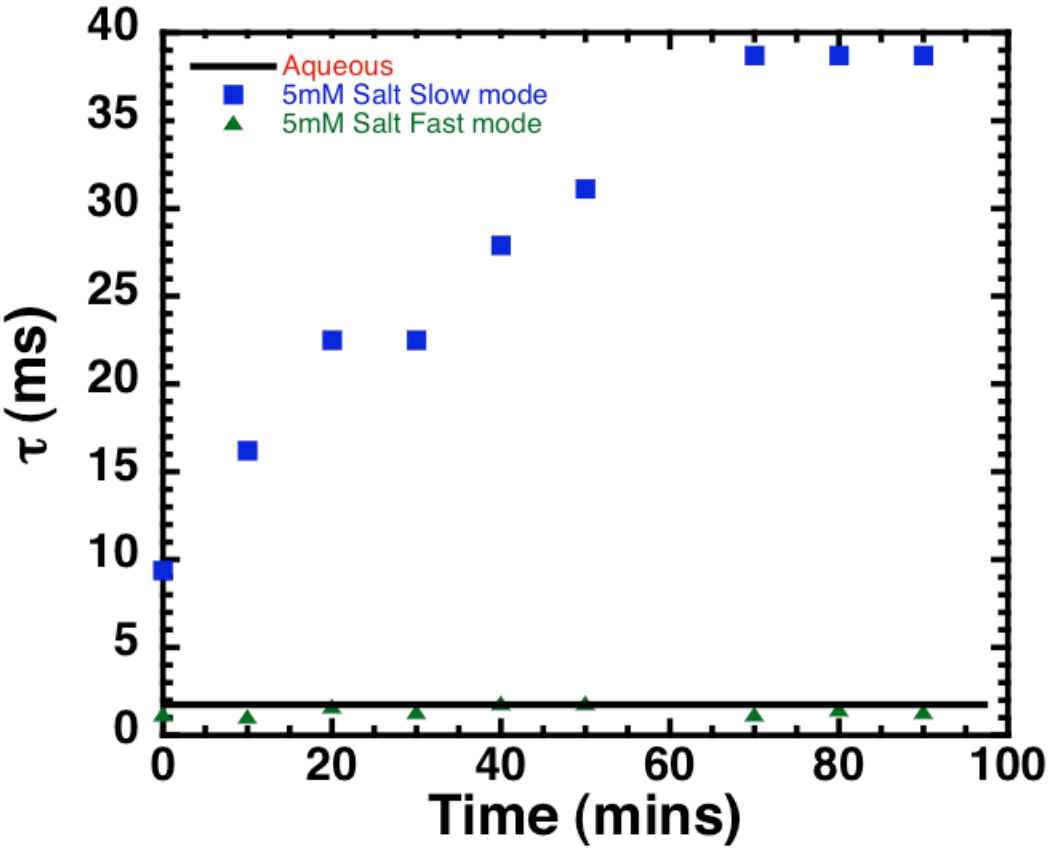

Figure 3.3: Peak decay relaxation time, τ, as a function of time of c=0.01 mg/ml of SWCNT-PABS in deionized water (aqueous) and with magnesium chloride salt (5mM $MgCl_2$) at θ=45.

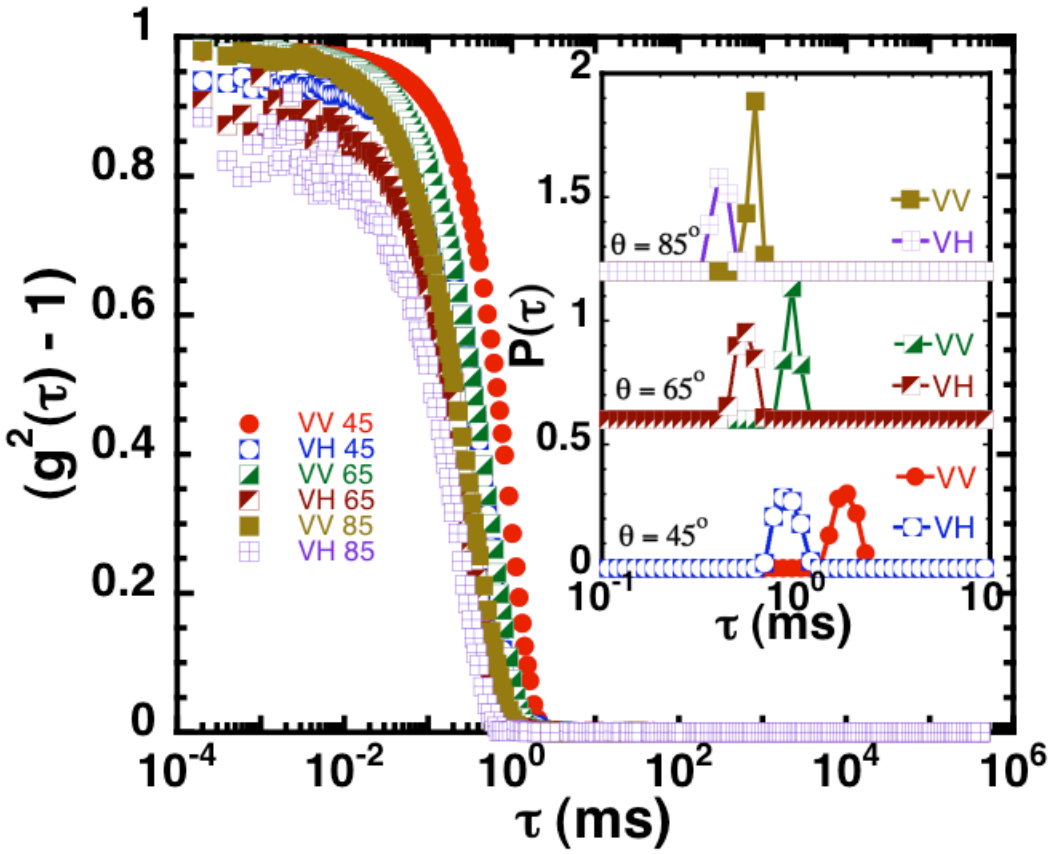

Figure 3.4: Comparison of the polarized (VV) and depolarized (VH) intensity autocorrelation functions $g_2(\tau)$ of SWCNT-PABS at c=0.01 mg/ml and at different scattering angles. The inset plot shows the probability distribution function, obtained from a CONTIN deconvolution of the measured VV and VH autocorrelation functions at different scattering angles.

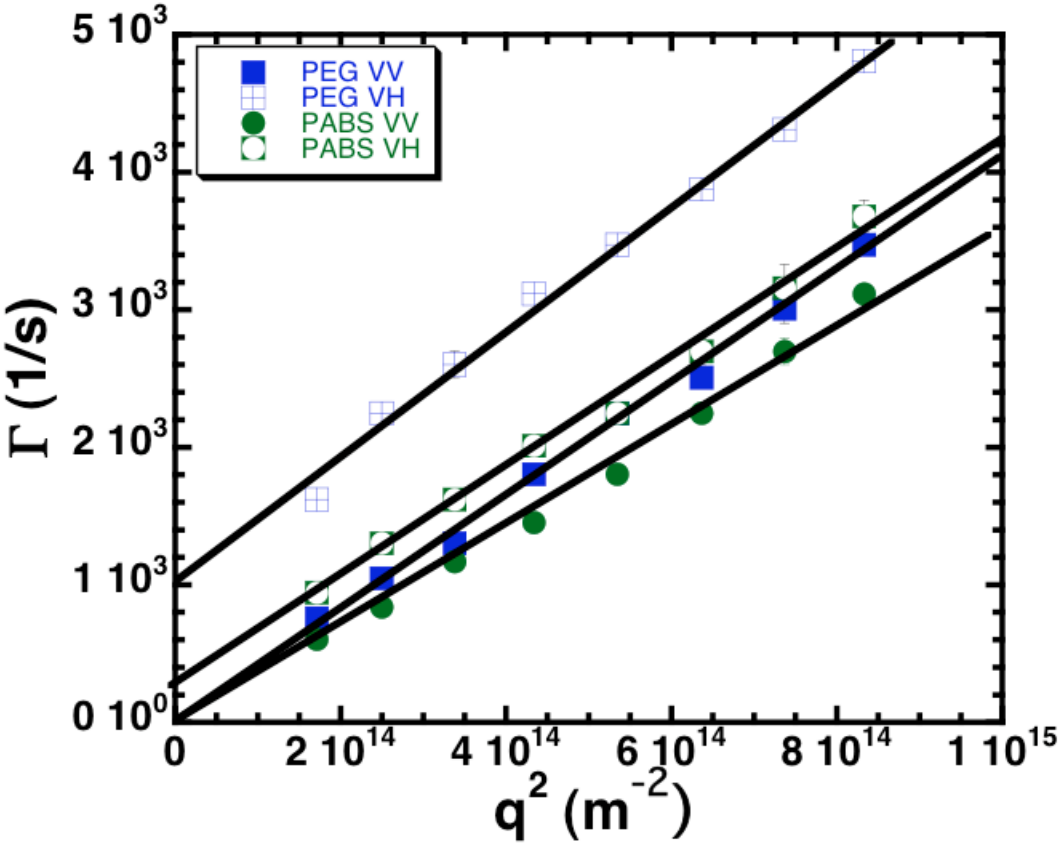

Figure 3.5: Γ Vs q^2 plot of SWCNT-PABS and SWCNT-PEG at c=0.01 mg/ml obtained from VV and VH scattering. Error bars reported are standard error of the mean.

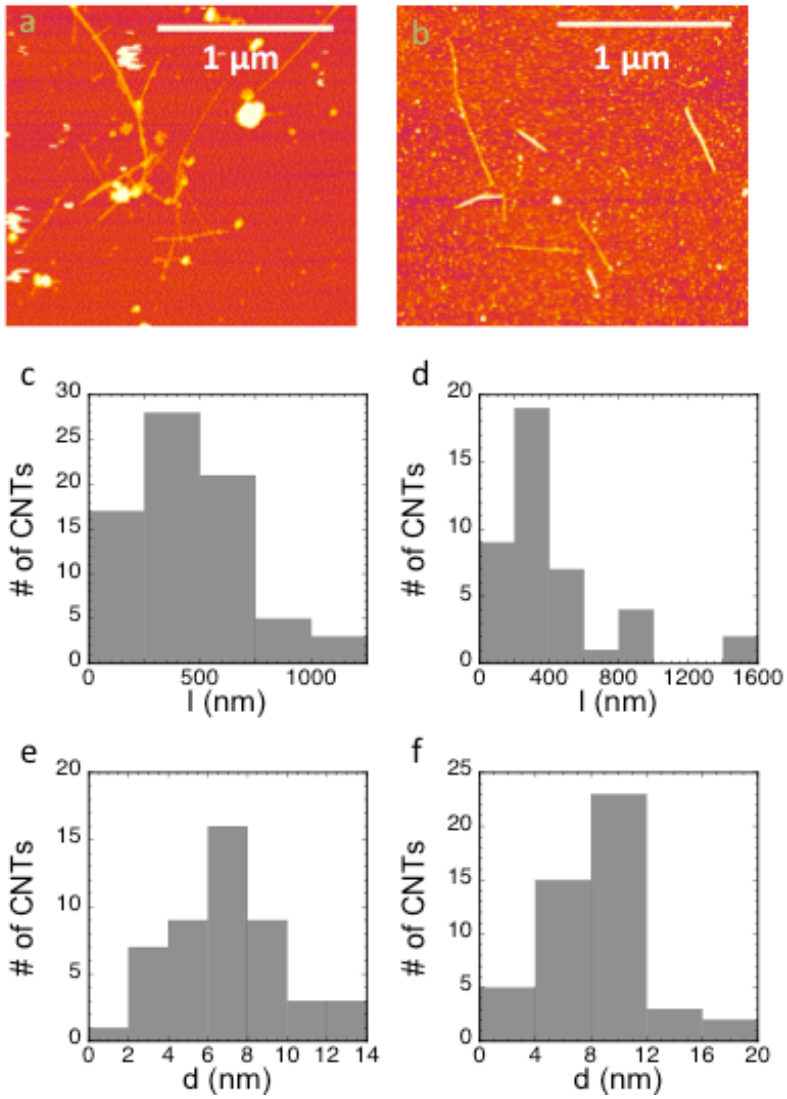

Figure 3.6: AFM micrographs for thin films of dried SWCNTs dispersions. Fig. a) corresponds to PEG functionalized SWCNTs and Fig. b) corresponds to PABS functionalized SWCNTs. We found that theSWCNT-PABS were more stable than the SWCNT-PEG. Dried films of suspensions of PEG-SWCNTs were prone to aggregation as can be seen in Fig. a). The scale bar is 1 µms. Fig. c) and d) show the distribution of CNT lengths for SWCNT-PEG and SWCNT-PABS respectively. Similarly, Fig. e) and f) correspond to the distribution of CNT diameters for SWCNT-PEG and SWCNT-PABS respectively.

Functionality	D_t ($\mu m^2/s$)	D_r (1/s)	L (nm) DDLS	D (nm) DDLS	L (nm) AFM	D (nm) AFM
PEG	4.09 ± 0.03	170 ± 5	541±6	4.4±0.2	458±29	6.8 ± 0.7
PABS	3.58 ± 0.03	44 ± 9	949±70	0.8±0.3	408±50	8.4 ± 0.8

Table 3.1: Summary of translational diffusion coefficient (D_t), rotational diffusion coefficient (D_r), length (L) and diameter (D) values obtained from DDLS and AFM measurements for SWCNT-PABS and SWCNT-PEG samples. Reported uncertainties correspond to the standard error of the mean.

3.6 References

1. Dai, L. M.; Soundarrajan, P.; Kim, T., Sensors and sensor arrays based on conjugated polymers and carbon nanotubes. *Pure and Applied Chemistry* **2002,** 74, (9), 1753-1772.

2. Modi, A.; Koratkar, N.; Lass, E.; Wei, B. Q.; Ajayan, P. M., Miniaturized gas ionization sensors using carbon nanotubes. *Nature* **2003,** 424, (6945), 171-174.

3. Heller, I.; Janssens, A. M.; Mannik, J.; Minot, E. D.; Lemay, S. G.; Dekker, C., Identifying the mechanism of biosensing with carbon nanotube transistors. *Nano Letters* **2008,** 8, (2), 591-595.

4. Bekyarova, E.; Kalinina, I.; Itkis, M. E.; Beer, L.; Cabrera, N.; Haddon, R. C., Mechanism of ammonia detection by chemically functionalized single-walled carbon nanotubes: In situ electrical and optical study of gas analyte detection. *Journal of the American Chemical Society* **2007,** 129, (35), 10700-10706.

5. Bekyarova, E.; Davis, M.; Burch, T.; Itkis, M. E.; Zhao, B.; Sunshine, S.; Haddon, R. C., Chemically functionalized single-walled carbon nanotubes as ammonia sensors. *Journal of Physical Chemistry B* **2004,** 108, (51), 19717-19720.

6. Green, A. A.; Hersam, M. C., Colored semitransparent conductive coatings consisting of monodisperse metallic single-walled carbon nanotubes. *Nano Letters* **2008,** 8, (5), 1417-1422.

7. Trancik, J. E.; Barton, S. C.; Hone, J., Transparent and catalytic carbon nanotube films. *Nano Letters* **2008,** 8, (4), 982-987.

8. Bekyarova, E.; Itkis, M. E.; Cabrera, N.; Zhao, B.; Yu, A. P.; Gao, J. B.; Haddon, R. C., Electronic properties of single-walled carbon nanotube networks. *Journal of the American Chemical Society* **2005,** 127, (16), 5990-5995.

9. Appenzeller, J.; Martel, R.; Derycke, V.; Radosavjevic, M.; Wind, S.; Neumayer, D.; Avouris, P., Carbon nanotubes as potential building blocks for future nanoelectronics. *Microelectronic Engineering* **2002,** 64, (1-4), 391-397.

10. LeMieux, M. C.; Roberts, M.; Barman, S.; Jin, Y. W.; Kim, J. M.; Bao, Z. N., Self-sorted, aligned nanotube networks for thin-film transistors. *Science* **2008,** 321, (5885), 101-104.

11. Andrews, R.; Jacques, D.; Rao, A. M.; Rantell, T.; Derbyshire, F.; Chen, Y.; Chen, J.; Haddon, R. C., Nanotube composite carbon fibers. *Applied Physics Letters* **1999,** 75, (9), 1329-1331.

12. Nanda, J.; Maranville, C.; Bollin, S. C.; Sawall, D.; Ohtani, H.; Remillard, J. T.; Ginder, J. M., Thermal conductivity of single-wall carbon nanotube dispersions: Role of interfacial effects. *Journal of Physical Chemistry C* **2008,** 112, (3), 654-658.

13. Biercuk, M. J.; Llaguno, M. C.; Radosavljevic, M.; Hyun, J. K.; Johnson, A. T.; Fischer, J. E., Carbon nanotube composites for thermal management. *Applied Physics Letters* **2002,** 80, (15), 2767-2769.

14. Jia, N. Q.; Lian, Q.; Shen, H. B.; Wang, C.; Li, X. Y.; Yang, Z. N., Intracellular delivery of quantum dots tagged antisense oligodeoxynucleotides by functionalized multiwalled carbon nanotubes. *Nano Letters* **2007,** 7, (10), 2976-2980.

15. Welsher, K.; Liu, Z.; Daranciang, D.; Dai, H., Selective Probing and Imaging of Cells with Single Walled Carbon Nanotubes as Near-Infrared Fluorescent Molecules. *Nano Lett*. **2008,** 8, (2), 586-590.

16. Wong, S. S.; Joselevich, E.; Woolley, A. T.; Cheung, C. L.; Lieber, C. M., Covalently functionalized nanotubes as nanometre-sized probes in chemistry and biology. *Nature* **1998,** 394, (6688), 52-55.

17. Moore, V. C.; Strano, M. S.; Haroz, E. H.; Hauge, R. H.; Smalley, R. E.; Schmidt, J.; Talmon, Y., Individually Suspended Single-Walled Carbon Nanotubes in Various Surfactants. *Nano Lett*. **2003,** 3, (10), 1379-1382.

18. Wu, Z. C.; Chen, Z. H.; Du, X.; Logan, J. M.; Sippel, J.; Nikolou, M.; Kamaras, K.; Reynolds, J. R.; Tanner, D. B.; Hebard, A. F.; Rinzler, A. G., Transparent, conductive carbon nanotube films. *Science* **2004,** 305, (5688), 1273-1276.

19. Rajan, A.; Strano, M. S.; Heller, D. A.; Hertel, T.; Schulten, K., Length-dependent optical effects in single walled carbon nanotubes. *Journal of Physical Chemistry B* **2008,** 112, (19), 6211-6213.

20. Davis, V. A.; Ericson, L. M.; Parra-Vasquez, A. N. G.; Fan, H.; Wang, Y. H.; Prieto, V.; Longoria, J. A.; Ramesh, S.; Saini, R. K.; Kittrell, C.; Billups, W. E.; Adams, W. W.; Hauge, R. H.; Smalley, R. E.; Pasquali, M., Phase Behavior and rheology of SWNTs in superacids. *Macromolecules* **2004,** 37, (1), 154-160.

21. Hough, L. A.; Islam, M. F.; Hammouda, B.; Yodh, A. G.; Heiney, P. A., Structure of semidilute single-wall carbon nanotube suspensions and gels. *Nano Letters* **2006,** 6, (2), 313-317.

22. Dror, Y.; Pyckhout-Hintzen, W.; Cohen, Y., Conformation of polymers dispersing single-walled carbon nanotubes in water: A small-angle neutron scattering study. *Macromolecules* **2005,** 38, (18), 7828-7836.

23. Wang, H.; Zhou, W.; Ho, D. L.; Winey, K. I.; Fischer, J. E.; Glinka, C. J.; Hobbie, E. K., Dispersing single-walled carbon nanotubes with surfactants: A small angle neutron scattering study. *Nano Letters* **2004,** 4, (9), 1789-1793.

24. Zhou, W.; Islam, M. F.; Wang, H.; Ho, D. L.; Yodh, A. G.; Winey, K. I.; Fischer, J. E., Small angle neutron scattering from single-wall carbon nanotube suspensions: evidence for isolated rigid rods and rod networks. *Chemical Physics Letters* **2004,** 384, (1-3), 185-189.

25. Yurekli, K.; Mitchell, C. A.; Krishnamoorti, R., Small-angle neutron scattering from surfactant-assisted aqueous dispersions of carbon nanotubes. *Journal of the American Chemical Society* **2004,** 126, (32), 9902-9903.

26. Fagan, J. A.; Landi, B. J.; Mandelbaum, I.; Simpson, J. R.; Bajpai, V.; Bauer, B. J.; Migler, K.; Walker, A. R. H.; Raffaelle, R.; Hobbie, E. K., Comparative measures of single-wall carbon nanotube dispersion. *Journal of Physical Chemistry B* **2006,** 110, (47), 23801-23805.

27. Schaefer, D. W.; Zhao, J.; Brown, J. M.; Anderson, D. P.; Tomlin, D. W., Morphology of dispersed carbon single-walled nanotubes. *Chemical Physics Letters* **2003,** 375, (3-4), 369-375.

28. Schaefer, D.; Brown, J. M.; Anderson, D. P.; Zhao, J.; Chokalingam, K.; Tomlin, D.; Ilavsky, J., Structure and dispersion of carbon nanotubes. *Journal of Applied Crystallography* **2003,** 36, 553-557.

29. Bauer, B. J.; Becker, M. L.; Bajpai, V.; Fagan, J. A.; Hobbie, E. K.; Migler, K.; Guttman, C. M.; Blair, W. R., Measurement of single-wall nanotube dispersion by size exclusion chromatography. *Journal of Physical Chemistry C* **2007,** 111, (48), 17914-17918.

30. Terrones, M., Science and technology of the twenty-first century: Synthesis, properties and applications of carbon nanotubes. *Annual Review of Materials Research* **2003,** 33, 419-501.

31. Dong, Q.; Gregory, J. W.; Wing Kam, L.; Min-Feng, Y.; Rodney, S. R., Mechanics of carbon nanotubes. *Applied Mechanics Reviews* **2002,** 55, (6), 495-533.

32. Li, Q. W.; Zhu, Y. T.; Kinloch, I. A.; Windle, A. H., Self-organization of carbon nanotubes in evaporating droplets. *Journal of Physical Chemistry B* **2006,** 110, (28), 13926-13930.

33. Parra-Vasquez, A. N. G.; Stepanek, I.; Davis, V. A.; Moore, V. C.; Haroz, E. H.; Shaver, J.; Hauge, R. H.; Smalley, R. E.; Pasquali, M., Simple length determination of single-walled carbon nanotubes by viscosity measurements in dilute suspensions. *Macromolecules* **2007,** 40, (11), 4043-4047.

34. Solomon, M. J.; Boger, D. V., The rheology of aqueous dispersions of spindle-type colloidal hematite rods. *Journal of Rheology* **1998,** 42, (4), 929-949.

35. Badaire, S.; Poulin, P.; Maugey, M.; Zakri, C., In Situ Measurements of Nanotube Dimensions in Suspensions by Depolarized Dynamic Light Scattering. *Langmuir* **2004,** 20, (24), 10367-10370.

36. Heller, D. A.; Mayrhofer, R. M.; Baik, S.; Grinkova, Y. V.; Usrey, M. L.; Strano, M. S., Concomitant length and diameter separation of single-walled carbon nanotubes. *Journal of the American Chemical Society* **2004,** 126, (44), 14567-14573.

37. B. Zhao, H. H. R. C. H., Synthesis and Properties of a Water-Soluble Single-Walled Carbon Nanotube-Poly(aminobenzene sulfonic acid) Graft Copolymer. *Advanced Functional Materials* **2004,** 14, (1), 71-76.

38. Zhao, B.; Hu, H.; Yu, A.; Perea, D.; Haddon, R. C., Synthesis and Characterization of Water Soluble Single-Walled Carbon Nanotube Graft Copolymers. *J. Am. Chem. Soc.* **2005,** 127, (22), 8197-8203.

39. Amiran, J.; Nicolosi, V.; Bergin, S. D.; Khan, U.; Lyons, P. E.; Coleman, J. N., High quality dispersions of functionalized single walled nanotubes at high concentration. *Journal of Physical Chemistry C* **2008,** 112, (10), 3519-3524.

40. Berne, B. J.; Pecora, R., *Dynamic Light Scattering*. J Wiley, New York: 1976.

41. Hobbie, E. K., Optical anisotropy of nanotube suspensions. *Journal of Chemical Physics* **2004,** 121, (2), 1029-1037.

42. Provencher, S. W., Contin - a general-purpose constrained regularization program for inverting noisy linear algebraic and integral-equations. *Computer Physics Communications* **1982,** 27, (3), 229-242.

43. Matsuoka, H.; Morikawa, H.; Yamaoka, H., Rotational diffusion of ellipsoidal latex particles in dispersion as studied by depolarized dynamic light scattering. *Colloids and Surfaces a-Physicochemical and Engineering Aspects* **1996,** 109, 137-145.

44. Drogemeier, J.; Eimer, W., Polarized and depolarized dynamic light-scattering study on f-actin in solution - comparison with model-calculations. *Macromolecules* **1994,** 27, (1), 96-101.

45. Lehner, D.; Lindner, H.; Glatter, O., Determination of the translational and rotational diffusion coefficients of rodlike particles using depolarized dynamic light scattering. *Langmuir* **2000,** 16, (4), 1689-1695.

46. Cush, R.; Dorman, D.; Russo, P. S., Rotational and translational diffusion of tobacco mosaic virus in extended and globular polymer solutions. *Macromolecules* **2004,** 37, (25), 9577-9584.

47. Pecora, R., *Dynamic Light Scattering: Applications of Photon Correlation Spectroscopy*. Plenum Press, New York and London: 1985.

48. Doi, M.; Edwards, S. F., *The Theory of Polymer Dynamics* Clareendon Press, Oxford: 1986.

49. Brenner, H., Rheology of a dilute suspension of axisymmetric brownian particles. *Int. J. Multiphase Flow* **1973,** 1, 195-341.

CHAPTER 4
DIRECT VISUALIZATION OF GLASSY DYNAMICS IN A MODEL POLAYMAIDE ROD SYSTEM

4.1 Chapter Summary

We study arrested dynamics in a model colloidal rod system by means of confocal microscopy. By means of image processing of acquired image series we show that arrested dynamics in these rod suspensions occurs at a critical volume fraction (ϕ_g), which depends sensitively on the aspect ratio of the rod suspension. The arrest volume fraction was identified by measuring the volume fraction dependence of an average correlation coefficient (R) that compares intensity values between two different images in a confocal microscopy image series as a function of the delay time between images. The arrest volume fractions, ϕ_g, obtained for the different aspect ratios used in this study are slightly lower than the theoretical scaling and simulation predictions for the minimum percolation volume fraction in a random homogenous network of rods. We explain this result as a consequence of the presence of repulsive interactions in our system. We quantify this effect of repulsive interactions by calculating the value of constant C to be 2.58 ± 0.18 on the lines of Edwards and Evans prediction[1]. Furthermore, we also investigate the elasticity and yielding behavior of these rod suspensions above their critical volume fraction (ϕ_g) by means of oscillatory shear experiments. We find that for all the rod suspensions studied, the elastic modulus monotonically increases with rod volume fraction and follows a power law given by $G' \sim (\phi-\phi_g)^{1.9\pm0.1}$, independent of the aspect ratio of the rod. This scaling is explained on the basis of 3D central force

percolation theory where rods form a rod network of freely jointed rods, which resist stretching but are amenable to bending motions in the network.

4.2 Introduction

Colloidal suspensions containing rod shaped particles find wide usage in applications such as functional ceramics[2], polymer nanocomposites[3], magnetic recording[4, 5] and pulp and papermaking[6]. Rod shaped particles are also key components of many industrial products such as paints[7], inks[8], cosmetics[7] and greases[9] and they also possess potentially valuable optical properties[10]. Depending on their interaction strength, aspect ratio and volume fraction, rod suspensions form microscopic structures ranging from fractals[11] to bundles to homogeneous networks[12]. Rod shaped particles are also of intense interest due to their ability to modify rheology at much lower volume fractions than their spherical counterparts[13].

The dynamics and microstructure of rod suspensions have been studied by the techniques of confocal microscopy[14], fluorescence video microscopy[15], dynamic light scattering[16], small angle light scattering[11], depolarized light scattering[17] and rheology[12, 18, 19]. Although many studies have considered the behavior of rod suspensions with fluid-like rheology, comparatively little experimental work has been done on arrested or slow dynamics of rod shaped colloids. One obstacle to studies of this kind has been the lack of a good model system in which properties such as aspect ratio and interaction potential may be independently tuned and thus the effect of these variables on network or gel structures probed. Although experimental data in the literature are limited, theoretical and simulation studies[20-26] are available. Monte Carlo simulations performed by Schilling et al., to study the effect of depletion on percolation threshold of nanorod networks revealed that the percolation threshold depended both on the depletion force and the aspect ratio of the rod suspension[26]. Recently Yatsenko et al., developed a theory which predicts that the

kinetic glass transition volume fraction for an isotropic suspension of hard rods is aspect ratio dependent[22]. Dynamical slowing down in rod suspensions can occur via two ways, one is due to excluded volume interactions and packing constraints and the second one is due to attractive interactions and bonding[19]. The structures formed correspondingly are called rod glasses and rod gels respectively. For spheres, a sequence of states spanning from glassy-like to gel-like exist[27] and a similar possibility exists for rod suspensions[28].

The aim of this chapter is to probe arrested dynamics and rheology in a model rod system and then compare our results with existing theories of the rod glass transition and rheological response. Recently Wilkins et al. introduced a model system comprising of self-assembled polyamide rods dispersed in an aqueous surfactant solution, which can be synthesized in sufficient quantities to study rod networks and glasses[29]. The system is of interest for fundamental studies because the aspect ratios and interaction potentials of the rods can be tuned over a wide range. Moreover, the rods can be synthesized via this method in sufficient quantities for investigation by scattering, microscopy and rheology.

In this work we have used confocal microscopy to visualize arrested dynamics in the Wilkins et al. model rod colloidal system. We apply an image processing method that allows us to characterize the change in system dynamics as a rod suspension progresses from liquid to glassy dynamics as the volume fraction is increased. Interestingly, we find that the volume fraction at which arrested dynamics occurs is highly aspect ratio dependent. In addition, shear rheology of these rod suspensions revealed a power law scaling close to two for the elastic shear modulus. The scaling exponent obtained in rheology was independent of the aspect ratio of the rod suspension.

The organization of this paper is as follows. We first briefly explain the confocal microscopy and rheological methods in section 2. We also discuss the image analysis procedure applied to characterization of suspension dynamics in section 2. In section 3 we present our results and then discuss them in section 4.

4.3 Experimental Section

4.3.1 Materials

Rod suspensions were synthesized as described in Wilkins et al[29]. Briefly, rod suspensions were prepared by stirring polyamide powder (Disparlon 6650, King Industries, Norwalk, CT) dispersed in an aqueous surfactant solution (16 wt% sodium dodecyl-benzenesulphonate obtained from Aldrich Chemical Company) using a 1cm magnetic stir bar in a 25 ml glass vial. The vial was sealed with a Teflon cap and kept in a temperature-controlled vat, which was placed on a hot plate. During the synthesis procedure it was ensured that the stirrer in the vial was always under constant mechanical agitation.

As described in Wilkins et al., depending on the solution preparation temperature, monodisperse rods (standard deviation in aspect ratio ~ 6%) of different aspect ratios were obtained. Table 4.1 reports the aspect ratios of all the rod suspensions prepared by the above method and used in this study, characterized as per results of Wilkins et al[29]., and confirmed by reflection confocal microscopy of the synthesized specimens. The volume fraction of rods in the synthesized suspensions was $\phi = 0.03$.

4.3.2 Methods

4.3.2.1 Sample preparation

Colloid rods synthesized as described above were diluted to different volume fractions using HPLC grade water for both confocal microscopy and rheological measurements ($0.0005<\phi< 0.03$). Dilute solutions of these rod suspensions were prepared with HPLC grade water (Sigma Aldrich) and placed on rollers (Wheaton Science Products) rotating at 3-6 rpm for about 30-45 minutes. The slow tumbling on the rollers dispersed the rod particles effectively as evidenced by Fig. 4.1(b)-(f).

4.3.2.2 Confocal laser scanning microscopy (CLSM)

Imaging was performed using the reflection (scattering) mode of an inverted Leica TCS SP2 confocal microscope using a 100x oil-immersion objective with a numerical aperture of 1.4 and laser excitation at $\lambda = 488$ nm. For rod suspension dynamics measurement, an image stack comprising of 40 images (2D slices) were taken with time interval between two consecutive images fixed at 1.635s. For rods with the high aspect ratios of 212 and 101, all images collected were of dimension 150 um by 150um with corresponding pixel sizes of 292.29nm by 292.29 nm in the x and y axes. Alternatively, for rods with lower aspect ratio 50 and 28, the images collected were of dimension 75um by 75um with corresponding pixel sizes of 147 nm by 147nm. Imaging was performed at least 25-30 um from the cover slip to avoid wall effects.

4.3.2.3 Image analysis

Image analysis was performed on CLSM images to extract quantitative information about the Brownian motion of the rods in the concentrated suspensions. Ideally, such analysis can yield the positions and orientations of all the rods in the specimen per a method such

as that of Mohraz and Solomon[14]. This work used CLSM coupled with quantitative image processing to visualize fluorescent colloidal rods and study jamming and order/disorder transitions in rod sediments. Recently Mukhija and Solomon used CLSM to quantify single-particle translational and rotational diffusion of fluorescent colloidal rods[30]. We could not use the above techniques in this work for the following reasons. First, rods synthesized in our method were not fluorescent. Second, because of the small diameter of our rods (~ 90 nm, much smaller than the wavelength of laser light used in CLSM), such direct methods could not be successfully applied to our model system. Instead, we developed a method based on correlating the spatially dependent image intensity values between images separated by a delay time Δt. As rods undergo Brownian displacements, cross-correlation statistics applied to pairs of images will become progressively less correlated, thereby facilitating differentiations between suspensions with fluid-like and glass-like dynamics.

This correlation image analysis was performed with the Image Correlation plugin[31] available in the Image J software made available by National Institute of Health (http://rsb.info.nih.gov/ij). The statistic used to correlate two images was the Pearson correlation coefficient, calculated for two images I_1 and I_2 separated by some delay time Δt according to the following equation:

$$R = \frac{\sum_{i=1}^{m}\sum_{j=1}^{n}(I_1(m_i,n_j)-\bar{I}_1)(I_2(m_i,n_j)-\bar{I}_2)}{(mn-1)\sigma_{I_1}\sigma_{I_2}}$$

where m and n are the number of pixels in the x and y directions respectively, $I_1(m_i,n_j)$ and $I_2(m_i,n_j)$ are the intensity values at the pixel location (m_i,n_j), of the images 1 and 2 respectively. Here, $\bar{I}_1$ and $\bar{I}_2$ are the mean intensity values for the entire image and σ_{I_1}

and σ_{I_2} are their standard deviations. The image series, comprising 40 images was cross correlated for a range of delay times varying from Δt =1.6s to Δt = 63.8s. More details can be obtained from the following documentation:

(http://www.gsca.net/IJ/ImageCorrelationJ.html).

An average correlation coefficient was obtained for each of these intervals as described above. This average correlation coefficient was then plotted as function of volume fraction of the rod suspension to indirectly characterize dynamics. In the past DLS has been the principle method used to study arrested dynamics in colloidal rod suspensions[29], particularly low-volume fraction gels[16]. However, in the case of the polyamide rod suspensions, DLS failed due to multiple scattering, which is a common condition for the high volume fraction rod suspensions used in our study[32].

4.3.2.4 Rheology

Rheological measurements were performed on an ARG2 stress controlled rheometer, TA instruments. A 2°, 60mm cone and plate geometry was used. All measurements were performed at a constant temperature of 25° C. A solvent trap around the sample minimized solvent evaporation during the experiment. To avoid effects from loading and shear history on our measurements, a specific protocol was followed. All measurements were pre-sheared at a low steady shear 10(1/s) for 30 s followed by sample equilibration on the rheometer plate for 2 minutes. A similar protocol to minimize shear history effects has been used in a study of the glassy rheology of hard spheres[33].

4.4 Results

4.4.1 Arrested dynamics by CLSM and Image correlation analysis

Fig. 4.1 reports the effect of increasing volume fraction on the microstructure of rod suspensions with aspect ratio, r =212. Qualitatively, as shown in the images of Fig. 4.1, all the volume fractions studied showed amorphous structure with no ordering or bundling. For rod dynamics, cross correlation analysis of the images was performed as described in the methods section for each of the image series acquired. The average correlation coefficient for each of the delay times studied is plotted as a function of volume fraction in Fig. 4.2 for a rod suspension with aspect ratio, r = 212. The error bars reported in Fig. 4.2 are standard error of the mean of three replications. The inset plot in Fig. 4.2 shows the same plot on a linear scale. It is clear that the plot can be divided into two regions, one with very high correlation (R>0.90) and second a region, at lower volume fraction, where the correlation increases linearly with increasing volume fraction. A high correlation value means that the intensity values of the pixels do not show much variation over the time interval studied. This small variation is indication of the relative immobility of the rods under these conditions. That is, for such high correlation coefficients, the rod suspension is in an arrested state where the rod particles are trapped by their neighbors and displacements are thereby limited. The lack of dependence of the correlation coefficient on the delay time is further evidence for the arrested dynamics of the rod system – such time-independence of correlations is characteristic of both gel[34] and glass[35] arrested dynamics. We note that $R \neq 1$ either because of small residual motion of the rods, or because of a small level of noise and instrument vibration that is recorded by the measurement.

In Fig. 4.2, the region where the correlation value decreases linearly with volume fraction means that there is a significant change in the intensity values of the pixels for the delay times studied. This behavior implies that the rods in the suspension have significant mobility, indicative of a suspension with fluid-like dynamics. The significant effect of delay time on the correlation coefficient is further evidence of the fluid-like dynamics of the rods in this volume fraction range (Recall that for single-particle diffusion, characteristic displacements grow as the square root of time). Linear extrapolation from the liquid phase region into the arrested phase region gives the onset volume fraction (ϕ_g) for arrested dynamics. Such an analysis for the r=212 rod suspension studied in Fig. 4.2 gives $\phi_g = 0.0029 \pm 0.0002$. Similar analysis was performed for the suspensions comprised of rods of other aspect ratio. These results are reported in Table 4.2.

In Fig. 4.3, we plot the onset volume fraction, henceforth referred to as a glass transition volume fraction, ϕ_g, as a function of aspect ratio (solid squares). Also plotted in Fig. 4.3 are the naïve mode coupling theory (NMCT) ideal glass transition volume fractions for tangent bead rods and spherocylinders[22]. The two upper dashed lines are the NMCT predictions for the spherocylinders and tangent bead respectively (For these theoretical results, behavior is only available for r < 40). The dashed upper line is a prediction by Philipse et al., for an arrest volume fraction in a rod suspension when all translation motions of a rod perpendicular to its long axis are blocked. Edwards and Evans using self-consistent mean field theory predict an arrest volume fraction in a rod suspension, which is aspect ratio dependent. They found the following relation, $\phi_{arrest}=0.785C/r$, where r=L/d is the aspect ratio of the rod[1] and C is a numerical constant which has been set to unity for plotting this prediction[1]. The dashed lower line in Fig. 4.3 is this Edwards and

Evans prediction. The solid line plotted in Fig. 4.3 is the minimum percolation volume fraction of a random homogenous network of rods which is given as follows: $\phi_{percolation}=0.7/r$. This percolation prediction of $\phi_{percolation}=0.7/r$ represents a lower boundary for the hard rod glass regime and is also in suitable agreement with the Edwards and Evans prediction ($\phi_{arrest}=0.785/r$). Our experimental results are slightly lower than these predictions. The most plausible explanation for this result is that our rod system has significant interactions. Modeling our data on the lines of Edwards and Evans ($\phi_{arrest}=0.785C/r$) yields a value of $C=2.58 \pm 0.18$. A higher C value obtained compared to unity explains the experimental data being below the theoretical and simulation scaling predictions. It also indicates that non-idealities such as interactions might be present in the rod system, which is causing this discrepancy. To further confirm this it is required that we estimate the interaction potential for our model rod system. This is addressed further in the discussion section.

4.4.2 Rheological Characterization

In Fig. 4.4 we show the elastic and viscous moduli, G' and G'' at a frequency, $\omega = 6.28$ (1/s) as a function of % strain for two different volume fractions (ϕ=0.04 and 0.03) in the glassy regime (above ϕ_g for that rod suspension). These measurements are for a rod suspension with an aspect ratio, L/D = 28. Results are in close agreement with the strain dependence of the elastic moduli seen in other soft glassy systems[36-39]. At low percent strains both elastic modulus, G' and storage modulus, G" are independent of % strain reflecting the linear behavior. In the linear regime G' is about an order of magnitude higher than G". With further increase in % strain, G' decreases while G" passes through a maximum before decreasing. The decrease is characteristic of yielding and liquid-like

behavior. The point at which G" crosses G' signals the transition from a viscoelastic solid to a viscoelastic liquid which is also termed as the yield point of the sample.

In Fig. 4.5 we plot the values of elastic modulus corresponding to the linear region or the plateau region versus effective volume fraction, $(\phi-\phi_g)$ for different aspect ratio rod suspensions. (Here ϕ_g is obtained from confocal microscopy and image processing as described before and $(\phi-\phi_g)$ signifies the volume fraction contribution above the arrested volume fraction for all the aspect ratios studied). Note that here we do not subtract the liquid phase contribution to the elastic modulus because oscillatory shear experiments showed that it could not be measured. The data show no dependence on the aspect ratio of the rod. The most plausible explanation for this result is that the rod suspensions investigated here all form a network structure. The viscoelasticity of such a network structure is dictated by number of contact points in the network and the average length of the rod between the contact points[40], rather than the aspect ratio of the rod building blocks. Given the lack of aspect ratio dependence we collect all the data together to characterize a power law scaling exponent. A power law fit to the data reveals that G' scales as $(\phi-\phi_g)^{1.9\pm0.1}$. We address the magnitude of the power law scaling seen here later in the discussion section. Lastly we would like to comment on the yield strain, ε_y, obtained from the nonlinear rheological characterization (See Fig. 4.4). Yield strain values for each of the rod suspensions studied were obtained from the maximum in the viscous loss modulus (G'')[37]. The dependence of ε_y on volume fraction for the different aspect ratios is shown in Fig. 4.6. It is evident from Fig. 4.6. that the yield strain shows no volume fraction dependence. In this regard our measurements appear to disagree with viscoelastic measurements performed by Hough et al., on surfactant stabilized single

walled carbon nanotubes where a ϕ dependent ε_y was found[49]. So no comparison to their ϕ dependent yield strain theory was possible.

4.5 Discussion

In Fig. 4.3, we observed that our experimental results are lower than the theoretical and scaling predictions for the minimum volume fraction for percolation. Now these theoretical and scaling predictions have been developed for rigid rods where the principle mode of pair interactions between the rods is the excluded volume repulsion[1, 41]. Therefore probable explanations for this discrepancy could be attributed to deviations of the polyamide rods from hard rod behavior. Such deviations might include some flexibility of the rods and/or potential interactions between the rods. We have addressed both these issues below.

The effect of stiffness on our measurements can be quantified by calculating the persistence length, L_p, for the rods. In this case we use a model of an inextensible elastic beam where the ratio of bending stiffnes, κ, to the thermal energy (k_BT) yields a characteristic persistence length $L_p = \kappa/k_BT$[42]. Bending stiffness can be calculated by the following expression $\kappa=EI$, where E is the elastic modulus and I is the moment of inertia about the rods axis. Such estimates have been used previously to estimate the Brownian bending dynamics of single walled carbon nanotubes[15]. Based on this the persistence length of the polyamide rods used in this study (L ~ 2.5 - 19 μm) is estimated to be ~ 0.009 - 0.072 m, a value more than three orders of magnitude greater than the rod length. From these estimates, one would conclude that that the polyamide rods are rigid since L << Lp. However, we include the observation that this estimate does not seem consistent with observations of the rods by CLSM in the dilute limit. For example, for the high

aspect ratio rod suspension, L/D = 212, used in the study we observed apparent shape fluctuations along the rods major axis when the rods are undergoing thermal undulations in solution. This uncertainty would support future direct measurements of the persistence length of the rods. Recently Duggal et al developed a fluorescence video microscopy based method to analyze shape fluctuations of single walled carbon nanotubes in solution to estimate their persistence lengths[15]. Using such a method for the high aspect ratio rods in our case could in principle provide an independent estimate for the persistence length.

Interactions between colloidal rod particles can play a significant role in determining their behavior in solution[43]. Here we have attempted to calculate the interaction potential between two polyamide rods. There are two major contributions to the interaction potential between the polyamide rods in our case: 1) repulsive electrostatic interactions (U_{Charge}) due to negative charges on the rods (independently measured via a electrophoretic measurement) and 2) attractive van der Waals interactions (U_{VdW}) due to the random rod contacts present in our rod system. Therefore the total interaction potential normalized by thermal energy, k_BT, can be described as follows:

$$\frac{U_{Tot}}{k_BT} = \frac{U_{VdW}}{k_BT} + \frac{U_{Charge}}{k_BT}.$$

The interaction is of course a function of the mutual orientation of the rods. Two limiting cases can be identified in which the rods are either in parallel or perpendicular orientations. Due to the complicated calculations for the general case of arbitrary orientation, we restrict our calculations to the case of the two rods orientated in parallel, since this case will yield the strongest interaction. Formulae for the van der Waals interaction potential between two similar parallel rods has been derived and are given by

$U_{VdW}(r) = \frac{-AL\sqrt{R}}{24r^{\frac{3}{2}}}$, where A is the non retarded Hamaker constant, L is the length of the rod, R is the radius of the rod and r is interaxial separation distance between the two rods[44]. The above expression holds for small interaxial separations r < 2R. The Coulombic or electrostatic interaction between two parallel rods has been analytically developed by solving the linear Poisson-Boltzmann equation. The screened electrostatic potential between two parallel rods of linear line charge density ξ is given by

$U_{Charge}(r) = \frac{2\xi^2}{\varepsilon_r \varepsilon_0} K_0(\frac{r}{\lambda_D})$, where r is the interaxial distance between the rods, λ_D is the Debye length, ε_r is the dielectric constant of the medium (in our case water), ε_0 is the permittivity in vaccum and K_0 is the zeroth-order modified Bessel function of the second kind[45-48]. The linear line charge density ξ is related to the surface charge density σ on a rod with radius R as follows $\xi = \frac{2\pi\sigma\lambda_D}{K_1(\frac{R}{\lambda_D})}$, where K_1 is the zeroth- order modified Bessel function of the first kind[45-48]. The total interaction potential between two parallel rods was calculated by using the above expressions for the van der Waal and electrostatic interactions. Parameters used above in the estimating the potentials were obtained from the following measurements and calculations: The surface charge density on the rods, σ=0.00179 C/m^2 used for calculating the electrostatic interactions was estimated from the zeta potential measurement. The zeta potential was measured using a Zetasizer Nano series (Malvern, United Kingdom) in a high salt limit (0.001 M KCl) where the Smoluchowski equation can be applied. The non-retarded Hamaker constant for the polyamide rods was estimated from Lifshitz theory[44] to be 1.29E-20 J. The Debye length

used was 2nm, which was calculated based on the conductivity measurement of free ions in the rod suspension.

Fig. 4.7. shows the curve for the total interaction potential for the various aspect ratios used in this study as a function of interaxial distance between the rods. We conclude from the plot that the interaction potential in this system is not long ranged since the total potential in this system decays to zero for r about 1/10 of the rod diameter. The plot also shows strong support for repulsive interactions indicating that the surface charge on the rods likely contributes to their stability in solution. Lower glass transition volume fractions obtained in this study when compared to the theoretical and simulation predictions can be attributed to the presence of these repulsive interactions in our model rod system. As described before, modeling our experimental data on the lines of Edwards and Evans yielded a higher value for the constant C, which is consistent with the presence of interactions in our system.

In Fig. 4.5, the elastic modulus, G' plotted as a function of effective volume fraction, $(\phi-\phi_g)$ for all the aspect ratio rod suspensions showed a power law scaling with an exponent of 1.9. Now similar power law scaling of 2.3 has been observed for the percolation threshold in the case of surfactant stabilized single wall carbon nanotube suspensions[49]. In this case the low frequency elastic modulus, G' exhibited a power law of the form $G' \sim (\phi-\phi^*)^{2.3}$, where ϕ^* is the percolation volume fraction. In addition, an exponent of 1.94 has been found for semiflexible protein assemblies, where G' scales as $(\phi-\phi_p)^{1.94}$ near the percolation threshold concentration[50]. Interestingly, bond percolation simulations have reported two different scaling exponents for physical and chemical gels. In chemical gels, a percolation exponent of 2.1±0.2 has been reported where the percolating bonds resist

stretching but are free to rotate under effect of strain. While for physical gels a scaling exponent of 3.75±0.11 has been found where the percolating bonds are amenable to both stretching and rotating[51]. In contrast, experimental investigation of volume fraction dependence of the elastic moduli in case of colloidal silica gels have revealed a exponent of 3±0.5 which is in between the two bond percolation predictions. The similarity of the exponent obtained in our experiments with the central force percolation theory obtained for chemical gels suggest that our rods form a rod network of freely jointed rods which resist stretching but are amenable to bending motions in the network.

4.6 Conclusion

In this work we have reported a study of the microstructure and rheology of a model rod colloidal system in the vicinity of glass transition. We have developed a method based on image correlation of spatial pixel intensity values to investigate the onset of arrested dynamics in a rod suspension. The glass transition volume fractions obtained By CLSM and image processing are found to be highly aspect ratio dependent and are lower than the scaling and simulation predictions for minimum volume fraction for percolation. We explain this discrepancy on the basis of repulsive attractions present in the model rod system. Oscillatory shear experiments revealed an unique power law dependence for the elastic modulus with volume fraction, irrespective of the aspect ratio of the rod. The power law exponent obtained can be explained on the basis of a 3D percolation theory where the major contribution to rod elasticity comes from bending of rods.

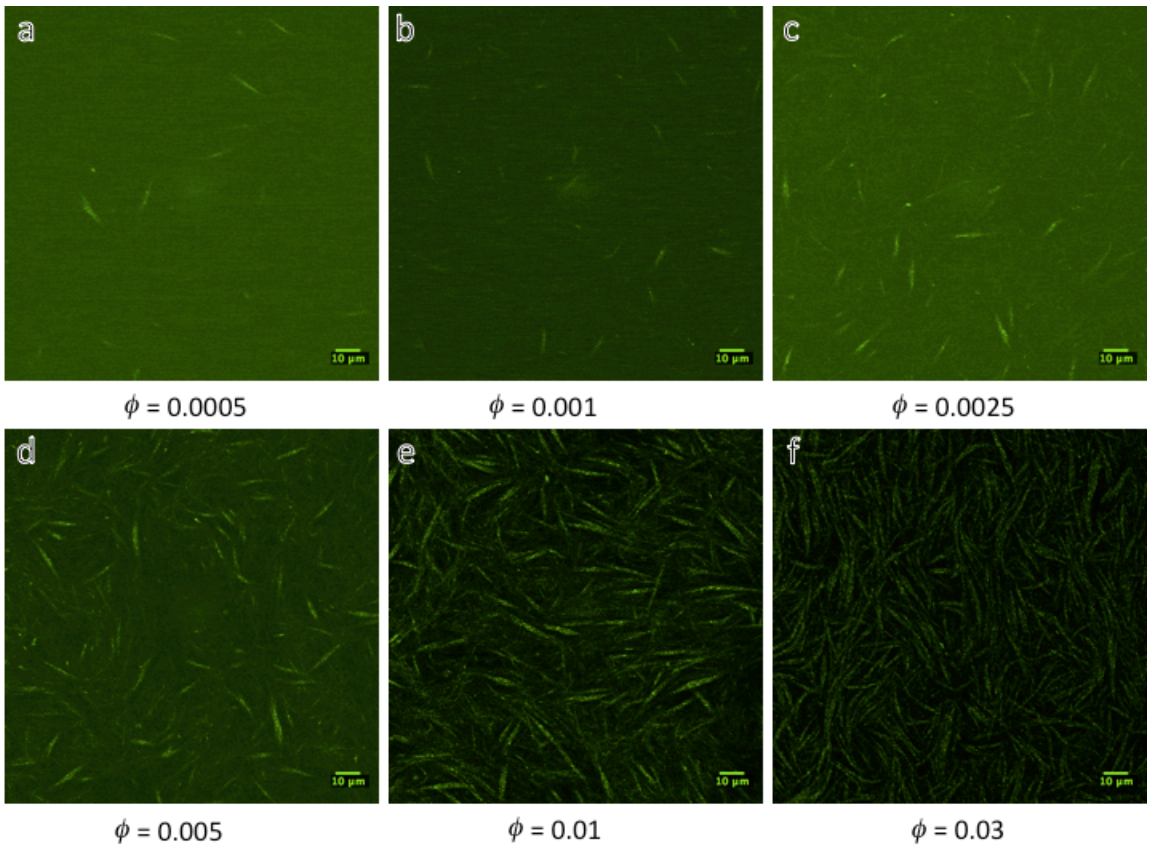

Figure 4.1: Representative 2D confocal micrographs of a rod suspension as a function of increasing rod volume fraction, ϕ, for a rod suspension with aspect ration, r = 212. (a) ϕ=0.0005, (b) ϕ=0.001, (c) ϕ=0.0025, (d) ϕ=0.005, (e) ϕ=0.01(f) ϕ=0.03.

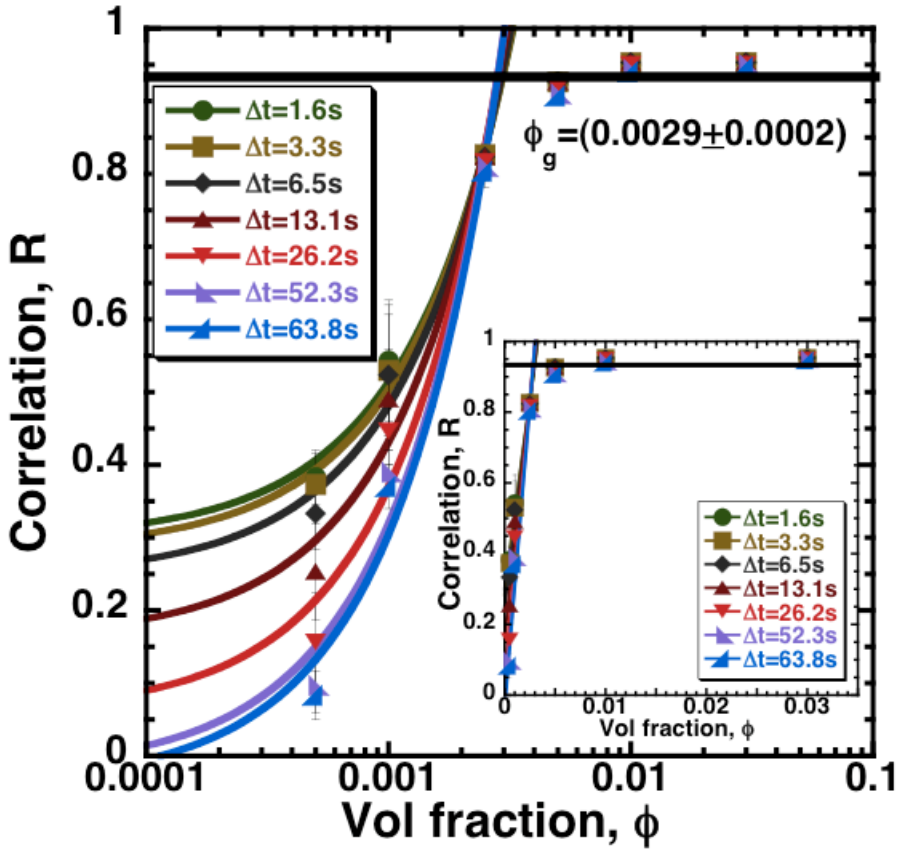

Figure 4.2: Change of Correlation coefficient, R with volume fraction, ϕ as a function of increasing time intervals between images for a rod suspension with aspect ratio, r =212.

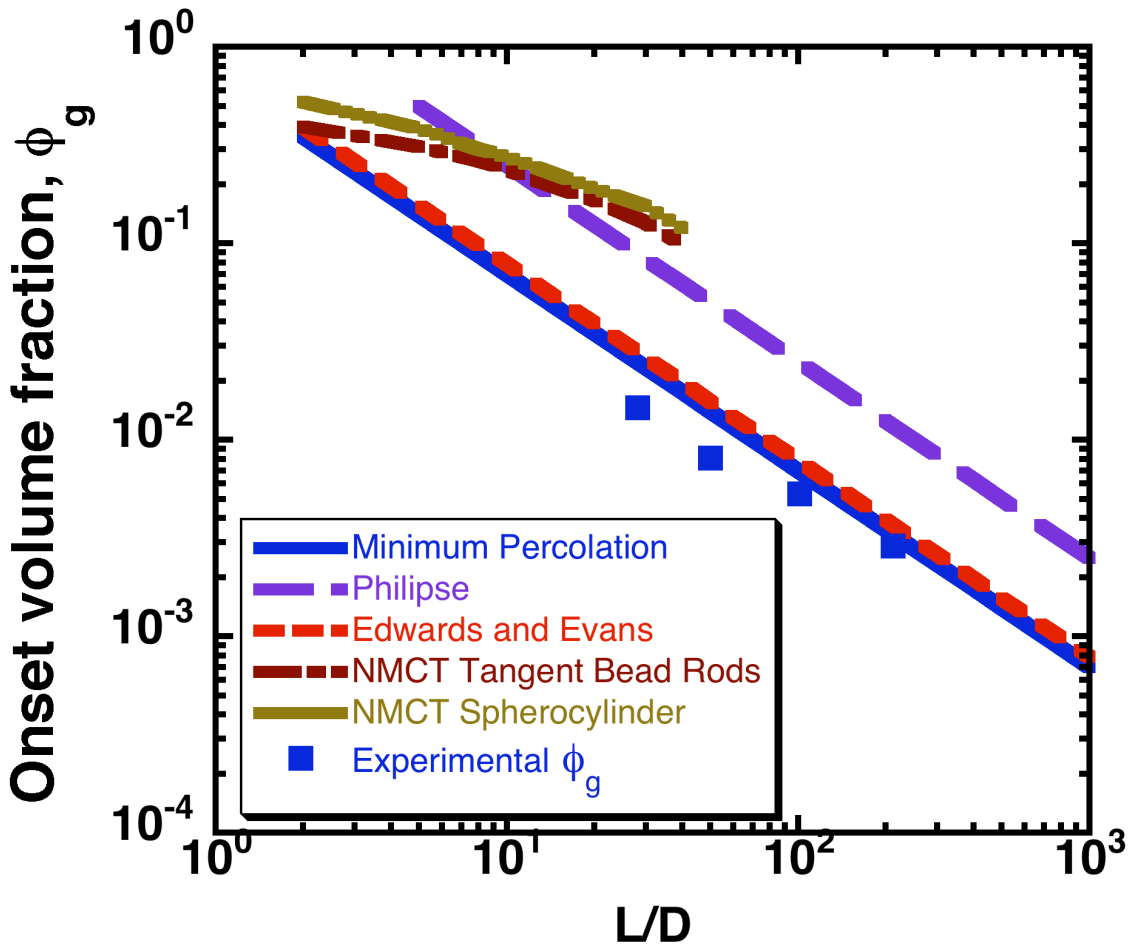

Figure 4.3: Plot of onset volume fraction Vs aspect ratio that compares our experimental values with existing rod theory predictions. The solid square symbols are the arrest volume fractions obtained via confocal microscopy and image processing. The top two dashed lines are the ideal glass transition volume fractions for spherocylinders and tangent bead rods obtained from NMCT theory. The dashed upper line is a prediction by Philipse et al., for an arrest volume fraction where one first sees arrest in a rod suspension due to no sideways translation movement possible. The lower solid line is the minimum percolation volume fraction of random homogenous rod network. The dashed lower line is the Edwards and Evans prediction for an arrest volume fraction for a highly entangled rod system where rotational diffusion of rods is seriously constrained. Error bars in this figure are less than the size of the datum points.

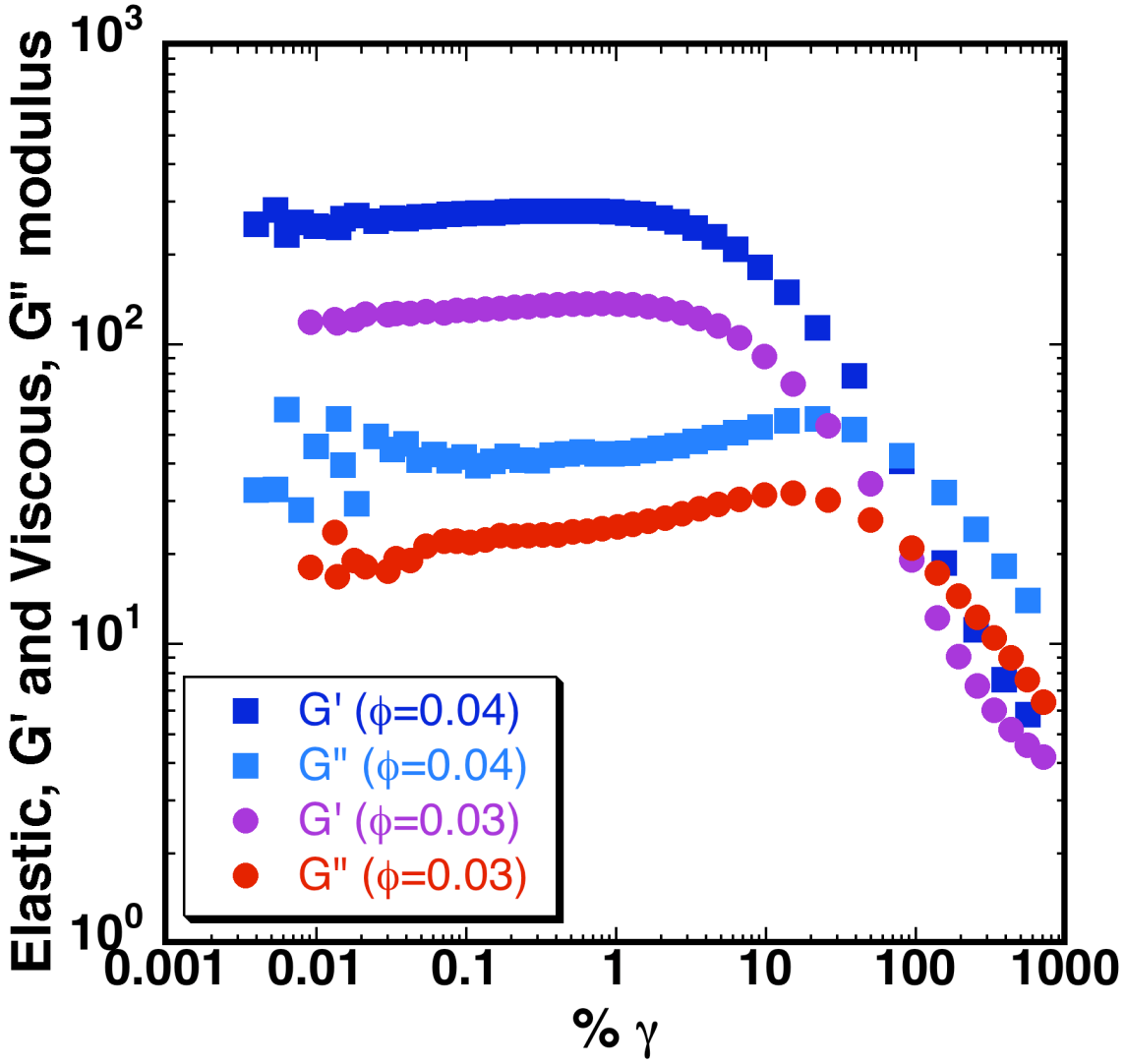

Figure 4.4: Elastic (G') and Viscous moduli (G") as a function of percent strain at an angular frequency of 6.28Hz.

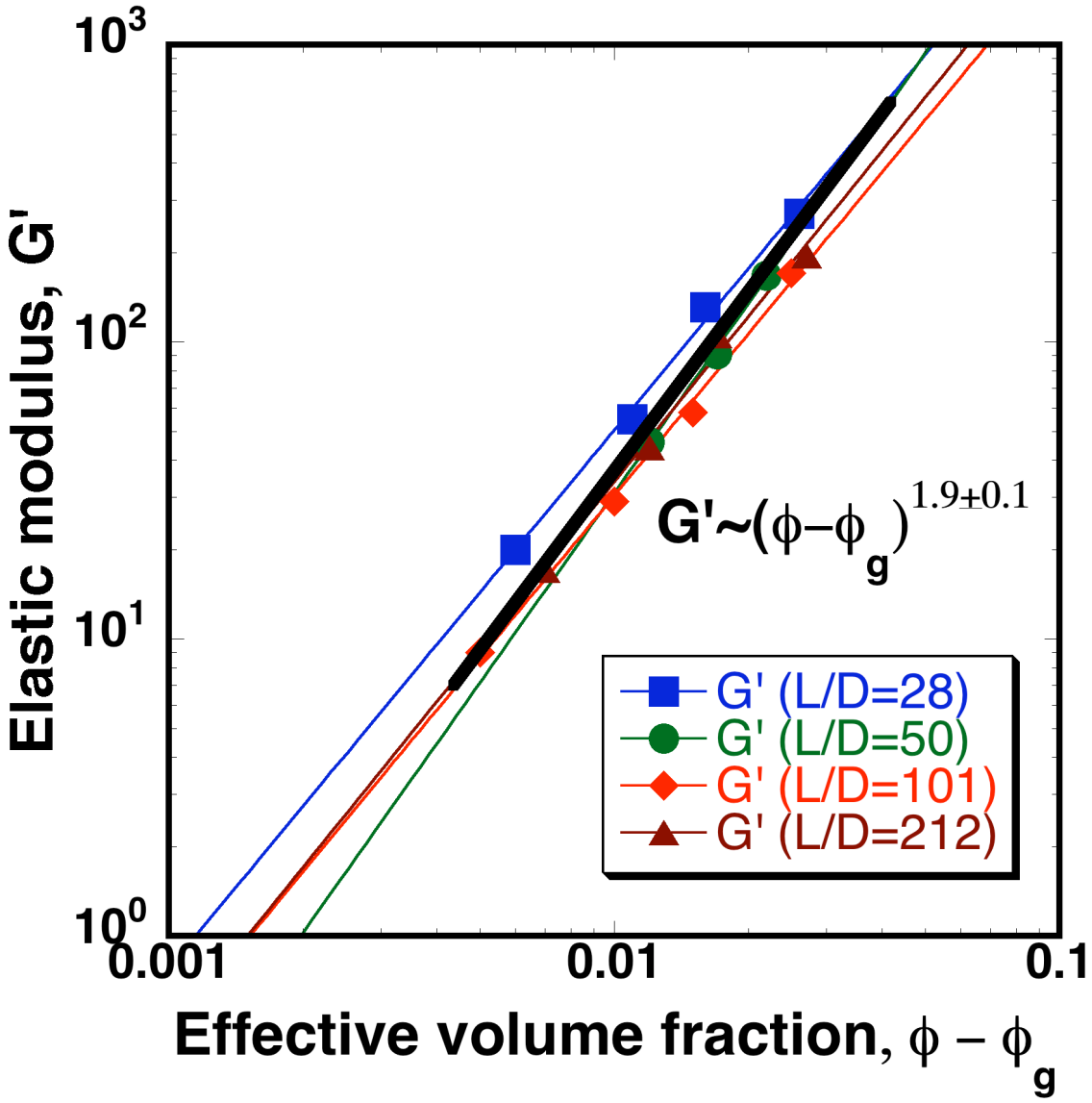

Figure 4.5: Elastic modulus obtained from the plateau region of G' Vs % strain curves (shown in Fig. 4.4) plotted as a function of effective volume fraction, (ϕ-ϕ_g).

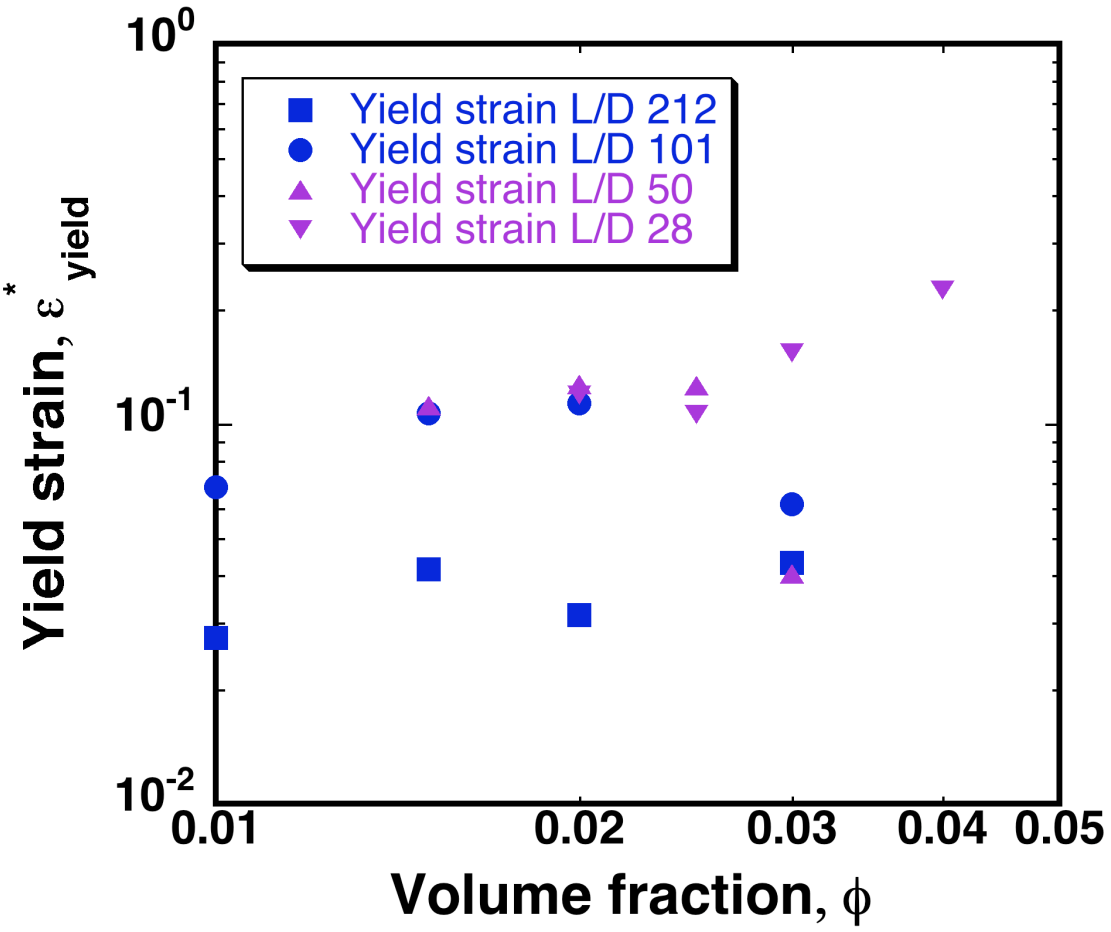

Figure 4.6: Volume fraction dependence of yield strain for the different aspect ratios studied.

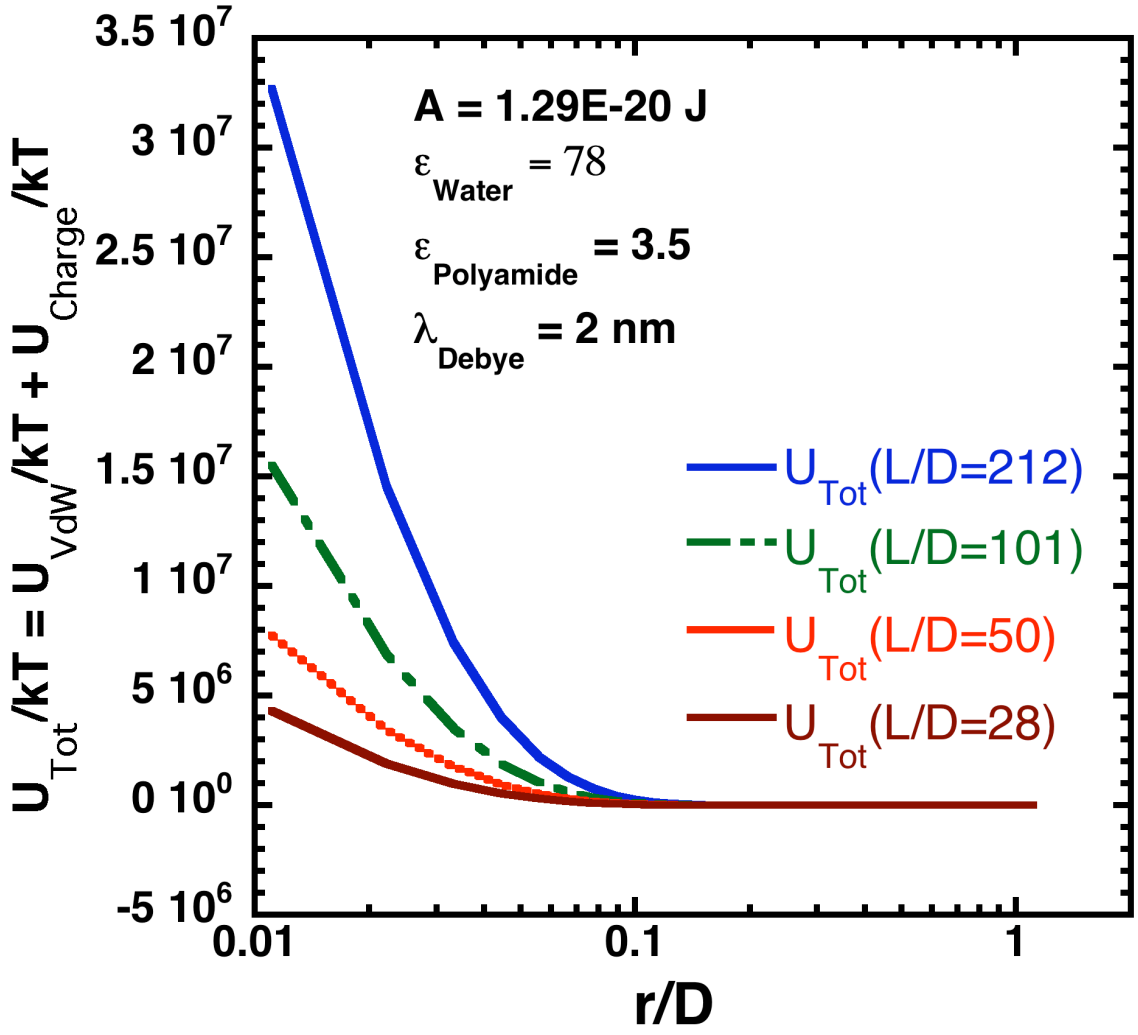

Figure 4.7: Total interaction potential, $U_{Tot}(r)/k_BT$ between two parallel polyamide rods plotted as a function of interaxial distance between the rods. The surface charge density on the rods, σ=0.00179 C/m^2 used for calculating the electrostatic interactions was estimated from the zeta potential measurement. The zeta potential was measured using a Zetasizer Nano series (Malvern, United Kingdom. The non-retarded Hamaker constant for the polyamide rods was estimated from Lifshitz theory to be 1.29E-20 J. The Debye length used is 2 nm.

T (°C)	R =L/d
62	28±2
87	50±3
92	101±6
96	212±12

Table 4.1: Aspect ratios of all the rod suspensions synthesized and used in the study, as taken from measurements in Wilkins et al[29]., and confirmed by reflection CLSM imaging.

r =L/d	ϕ_g
28±2	0.0146±0.0007
50±3	0.0081±0.0003
101±6	0.0053±0.0001
212±12	0.0029±0.0002

Table 4.2: Onset volume fraction, ϕ_g obtained from Confocal microscopy for all the aspect ratios studied.

4.7 References

1. Edwards, S. F.; Evans, K. E., Dynamics of highly entangled rod-like molecules. *Journal of the Chemical Society-Faraday Transactions Ii* **1982,** 78, 113-121.

2. Lewis, J. A., Colloidal processing of ceramics. *Journal of the American Ceramic Society* **2000,** 83, (10), 2341-2359.

3. Hasegawa, N.; Kawasumi, M.; Kato, M.; Usuki, A.; Okada, A., Preparation and mechanical properties of polypropylene-clay hybrids using a maleic anhydride-modified polypropylene oligomer. *Journal of Applied Polymer Science* **1998,** 67, (1), 87-92.

4. Arnoldussen, T. C.; Rossi, E. M., Materials for magnetic recording. *Annual Review of Materials Science* **1985,** 15, 379-409.

5. Inaba, H.; Ejiri, K.; Abe, N.; Masaki, K.; Araki, H., The advantages of the thin magnetic layer on a metal particulate tape. *Ieee Transactions on Magnetics* **1993,** 29, (6), 3607-3612.

6. Lima, M. M. D.; Borsali, R., Rodlike cellulose microcrystals: Structure, properties, and applications. *Macromolecular Rapid Communications* **2004,** 25, (7), 771-787.

7. Nishinari, K., Rheological and related studies on industrially important polysaccharides and proteins. *Journal of Central South University of Technology* **2007,** 14, 498-504.

8. Hong, L.; Anthony, S. M.; Granick, S., Rotation in suspension of a rod-shaped colloid. *Langmuir* **2006,** 22, (17), 7128-7131.

9. Magnin, A.; Piau, J. M., Application of freeze-fracture technique for analyzing the structure of lubricant greases. *Journal of Materials Research* **1989,** 4, (4), 990-995.

10. Velikov, K. P.; van Dillen, T.; Polman, A.; van Blaaderen, A., Photonic crystals of shape-anisotropic colloidal particles. *Applied Physics Letters* **2002,** 81, (5), 838-840.

11. Mohraz, A.; Moler, D. B.; Ziff, R. M.; Solomon, M. J., Effect of monomer geometry on the fractal structure of colloidal rod aggregates. *Physical Review Letters* **2004,** 92, (15), 155503.

12. Wierenga, A.; Philipse, A. P.; Lekkerkerker, H. N. W.; Boger, D. V., Aqueous dispersions of colloidal boehmite: Structure, dynamics, and yield stress of rod gels. *Langmuir* **1998,** 14, (1), 55-65.

13. Vigolo, B.; Coulon, C.; Maugey, M.; Zakri, C.; Poulin, P., An experimental approach to the percolation of sticky nanotubes. *Science* **2005,** 309, (5736), 920-923.

14. Mohraz, A.; Solomon, M. J., Direct visualization of colloidal rod assembly by confocal microscopy. *Langmuir* **2005,** 21, (12), 5298-5306.

15. Duggal, R.; Pasquali, M., Dynamics of individual single-walled carbon nanotubes in water by real-time visualization. *Physical Review Letters* **2006,** 96, (24), 246104.

16. Mohraz, A.; Solomon, M. J., Gelation and internal dynamics of colloidal rod aggregates. *Journal of Colloid and Interface Science* **2006,** 300, (1), 155-162.

17. Shetty, A. M.; Wilkins, G. M. H.; Nanda, J.; Solomon, M. J., Multiangle Depolarized Dynamic Light Scattering of Short Functionalized Single-Walled Carbon Nanotubes. *Journal of Physical Chemistry C* **2009,** 113, (17), 7129-7133.

18. Fan, Z. H.; Advani, S. G., Rheology of multiwall carbon nanotube suspensions. *Journal of Rheology* **2007,** 51, (4), 585-604.

19. Solomon, M. J.; Boger, D. V., The rheology of aqueous dispersions of spindle-type colloidal hematite rods. *Journal of Rheology* **1998,** 42, (4), 929-949.

20. Letz, M.; Schilling, R.; Latz, A., Ideal glass transitions for hard ellipsoids. *Physical Review E* **2000,** 62, (4), 5173-5178.

21. Philipse, A. P.; Verberkmoes, A., Statistical geometry of caging effects in random thin-rod structures. *Physica a-Statistical Mechanics and Its Applications* **1997,** 235, (1-2), 186-193.

22. Yatsenko, G.; Schweizer, K. S., Glassy dynamics and kinetic vitrification of isotropic suspensions of hard rods. *Langmuir* **2008,** 24, (14), 7474-7484.

23. Theenhaus, T.; Allen, M. P.; Letz, M.; Latz, A.; Schilling, R., Dynamical precursor of nematic order in a dense fluid of hard ellipsoids of revolution. *European Physical Journal E* **2002,** 8, (3), 269-274.

24. Yatsenko, G.; Schweizer, K. S., Ideal vitrification, barrier hopping, and jamming in fluids of modestly anisotropic hard objects. *Physical Review E* **2007,** 76, (4), 041506.

25. Yatsenko, G.; Schweizer, K. S., Ideal glass transitions, shear modulus, activated dynamics, and yielding in fluids of nonspherical objects. *Journal of Chemical Physics* **2007,** 126, (1), 014505.

26. Schilling, T.; Jungblut, S.; Miller, M. A., Depletion-induced percolation in networks of nanorods. *Physical Review Letters* **2007,** 98, (10), 108303.

27. Trappe, V.; Sandkuhler, P., Colloidal gels - low-density disordered solid-like states. *Current Opinion in Colloid & Interface Science* **2004,** 8, (6), 494-500.

28. Solomon, M. J.; Spicer, P. T., Microstructural regimes of colloidal rod suspensions, gels and glasses. *Soft Matter* **2010,** 6, (7), 1391-1400.

29. Wilkins, G. M. H.; Spicer, P. T.; Solomon, M. J., Colloidal System To Explore Structural and Dynamical Transitions in Rod Networks, Gels, and Glasses. *Langmuir* **2009,** 25, (16), 8951-8959.

30. Mukhija, D.; Solomon, M. J., Translational and rotational dynamics of colloidal rods by direct visualization with confocal microscopy. *Journal of Colloid and Interface Science* **2007,** 314, (1), 98-106.

31. Chinga, G.; Syverud, K., Quantification of paper mass distributions within local picking areas. *Nordic Pulp & Paper Research Journal* **2007,** 22, (4), 441-446.

32. Berne, B. J.; Pecora, R., *Dynamic Light Scattering*. J Wiley, New York: 1976.

33. Koumakis, N.; Schofield, A. B.; Petekidis, G., Effects of shear induced crystallization on the rheology and ageing of hard sphere glasses. *Soft Matter* **2008,** 4, (10), 2008-2018.

34. Solomon, M. J.; Varadan, P., Dynamic structure of thermoreversible colloidal gels of adhesive spheres. *Physical Review E* **2001,** 63, (5), 051402.

35. Vanmegen, W.; Underwood, S. M.; Pusey, P. N., Dynamics of hard spherical colloids from the fluid to the glass. *Journal of the Chemical Society-Faraday Transactions* **1991,** 87, (3), 395-401.

36. Derec, C.; Ducouret, G.; Ajdari, A.; Lequeux, F., Aging and nonlinear rheology in suspensions of polyethylene oxide-protected silica particles. *Physical Review E* **2003,** 67, (6), 061403.

37. Helgeson, M. E.; Wagner, N. J.; Vlassopoulos, D., Viscoelasticity and shear melting of colloidal star polymer glasses. *Journal of Rheology* **2007,** 51, (2), 297-316.

38. Mason, T. G.; Lacasse, M. D.; Grest, G. S.; Levine, D.; Bibette, J.; Weitz, D. A., Osmotic pressure and viscoelastic shear moduli of concentrated emulsions. *Physical Review E* **1997,** 56, (3), 3150-3166.

39. Senff, H.; Richtering, W.; Norhausen, C.; Weiss, A.; Ballauff, M., Rheology of a temperature sensitive core-shell latex. *Langmuir* **1999,** 15, (1), 102-106.

40. Hill, R. J., Elastic Modulus of Microfibrillar Cellulose Gels. *Biomacromolecules* **2008,** 9, (10), 2963-2966.

41. Philipse, A. P., The random contact equation and its implications for (colloidal) rods in packings, suspensions, and anisotropic powders. *Langmuir* **1996,** 12, (5), 1127-1133.

42. Larson, R. G., *The Structure and Rheology of Complex Fluids*. New York: Oxford University Press: 1999.

43. Russel, W. B.; D.A., S.; Schowalter, W. R., *Colloidal Dispersions*. Cambridge University Press: 1989.

44. Israelachvilli, J. N., *Intermolecular and Surface forces: With applications to colloidal and biological systems*. 1985.

45. Brenner, S. L.; McQuarri.Da, Theory of electrostatic interaction between parallel cylindrical polyelectrolytes. *Journal of Colloid and Interface Science* **1973,** 44, (2), 298-317.

46. Brenner, S. L.; Parsegia.Va, Physical method for deriving electrostatic interaction between rod-like polyions at all mutual angles. *Biophysical Journal* **1974,** 14, (14), 327-334.

47. Ohshima, H., Electrostatic interaction between two parallel cylinders. *Colloid and Polymer Science* **1996,** 274, (12), 1176-1182.

48. Ohshima, H., Surface charge density surface potential relationship for a cylindrical particle in an electrolyte solution. *Journal of Colloid and Interface Science* **1998,** 200, (2), 291-297.

49. Hough, L. A.; Islam, M. F.; Hammouda, B.; Yodh, A. G.; Heiney, P. A., Structure of semidilute single-wall carbon nanotube suspensions and gels. *Nano Letters* **2006,** 6, (2), 313-317.

50. van der Linden, E.; Parker, A., Elasticity due to semiflexible protein assemblies near the critical gel concentration and beyond. *Langmuir* **2005,** 21, (21), 9792-9794.

51. Sahimi, M.; Arbabi, S., Mechanics of disordered solids .2. percolation on elastic networks with bond-bending forces. *Physical Review B* **1993,** 47, (2), 703-712.

CHAPTER 5
CONCLUSIONS AND FUTURE WORK

5.1 Conclusions

In this thesis we have developed novel experimental techniques to characterize microstructure in complex fluids and we have been successful in relating the microstructure to rheological performance of complex fluids. In this chapter we summarize the key findings of this study.

In Chapter 2, the problem of PEO aggregation in aqueous solution was investigated and its role in turbulent drag reduction was quantified by using a novel experimental design, which involved a unique chaotropic/inorganic salt and simultaneous dynamic light scattering/fluid dynamics methodology to study dilute PEO aggregate flow properties. The DLS relaxation spectra of high molar mass dilute aqueous PEO solutions showed a unique scaling for the relaxation rate with a power law exponent of there. This scaling was found consistent with internal fluctuations of a large polymer aggregate coil. Addition of an inorganic ($MgSO_4$) or chaotropic salt (GuS) decreased the power law scaling exponent of the relaxation rate from three to two. This shift of the power law scaling exponent from three (indicative of aggregate dynamics) to two (characteristic of polymer center-of-mass diffusion) showed that these salts are effective de-aggregation agents for PEO. Further it was also shown that such modulation of aggregate structure in PEO is directly related to its drag reduction performance in fluid flow applications. These results have improved our fundamental understanding of the behavior of dilute PEO

solutions in flow by demonstrating the effect of salt on aggregate structure and by linking aggregate structure to flow behavior of PEO.

In Chapter 3, we showed that Multi- angle depolarized dynamic light scattering (MA-DDLS) can be used as a potential tool to characterize single walled carbon nanotubes (SWCNTs). Multi-angle DDLS is shown to be a simple, non-invasive tool for determination of the length and diameter of SWCNTs. The length and diameter of the nanotubes were determined from independent translational and rotational diffusion coefficient measurements in the dilute limit, with considerable advantages relative to other sizing techniques such as atomic force microscopy and transmission electron microscopy. The method developed is of considerable merit since it reduces the need to use time-consuming microscopy based methods. The bounds of applicability of the MA-DDLS method were also discussed.

In Chapter 4, CLSM and rheology was used to characterize the microstructure and dynamics of a model rod system. An image processing method based on image correlation of spatial pixel intensity values was developed to characterize the change in rod suspension dynamics from liquid to glassy as the rod volume fraction was increased. The glass transition volume fractions obtained were found to be highly aspect ratio dependent and were found to be lower than the scaling and simulation predictions for aspect ratio dependent percolation. Such deviations of the polyamide rods from hard rod behavior were attributed to the flexibility of the rods and/or potential interactions between rods. Rheological experiments revealed a unique power law dependence for the elastic modulus with volume fraction. The scaling exponent obtained was also found to be independent of the aspect ratio of the rod. The power law exponent obtained via

rheology was explained on the basis of a 3D percolation theory where the major contribution to rod elasticity comes from bending of the rods. These results can broadly be applied for developing complex fluid stabilization strategies, which play a key role in consumer products such as shampoo, detergents, gels etc. Another merit of this work is that these experimental data can be used for validation of existing rod network or gel theories.

5.2 Future Work

In Chapter 2, a lower bound on the size of PEO aggregates was placed and this was found to be around 740 nm and a DLS device that can probe $q << 1.33\ \mu m^{-1}$ or $\theta << 6°$ was suggested, where q and θ are the wave vector and scattering angle respectively. The way forward to improve this estimate would be a nice extension for the work done in Chapter 2. Current DLS instruments do not have the capability to probe polymer dynamics at such low scattering angles or wave vectors. Thus this would require that a small angle dynamic light scattering device be built which can probe such small wave vectors. In a sufficiently small angle limit the DLS spectra of dilute PEO solutions would be consistent with centre of mass diffusion of multi-molecule aggregates with an effective hydrodynamic size that is many times greater than the hydrodynamic response of a single molecule of PEO[1]. Therefore a small angle dynamic light scattering device would have the capability to probe centre of mass diffusion of large aggregate coils such as of those of PEO. Such small angle DLS instruments have recently become available where the polymer dynamics can be measured at angles as low as 0.4°[2, 3]. The device relies on measuring autocorrelation functions by resolving the time dependence of the speckle

pattern on a CCD camera[2]. These correlations once measured can then be analyzed using the CONTIN algorithm[4] to give an effective coil size for the PEO aggregate.

In Chapter 2 the MA-DDLS has been successfully applied to short functionalized monodisperse carbon nanotubes. The data analysis procedure used in Chapter 2 assumed that the single walled carbon nanotubes (SWCNTs) used are rigid. This was a reasonable assumption since a recent study has shown that SWCNTs up to about 1 μm in length can be treated as rigid[5]. But often carbon nanotubes used for several applications are longer (several μms in length) and also the distribution of lengths may not be monodisperse. The MA-DDLS method should be extended to longer carbon nanotubes in a future study. For longer rods, it would require that the equations used for modeling the polarized and depolarized correlation functions be modified to include the effects of finite flexibility and polydispersity[6, 7].

In chapter 3 the change in microstructure and dynamics in a model rod system was studied both as a function of aspect ratio and volume fraction. There might be other parameters, which were not investigated in this study such as the interaction potential between the rods, which might have considerable effect on arrested dynamics of rod suspensions. The effect of interaction potential on glassy dynamics of rod suspensions would be an interesting future study. The interaction potential between the rods can be varied by a polymer induced depletion interaction[8] and the effect of this on glass transition volume fractions, ϕ_g, would greatly improve fundamental understanding of rod network formation. Also the effect of stiffness on our measurements is uncertain at this point. This uncertainty would require a future study where the persistent length of the rods could be measured. In this regard a recent technique developed by Duggal et al.,

would be handy. The method relies on estimating shape fluctuations of rods in solvents to estimate their persistent lengths[5].

5.3 References

1. Shetty, A. M.; Solomon, M. J., Aggregation in dilute solutions of high molar mass poly(ethylene) oxide and its effect on polymer turbulent drag reduction. *Polymer* **2009,** 50, (1), 261-270.

2. Cipelletti, L.; Weitz, D. A., Ultralow-angle dynamic light scattering with a charge coupled device camera based multispeckle, multitau correlator. *Review of Scientific Instruments* **1999,** 70, (8), 3214-3221.

3. Ferri, F., Use of a charge coupled device camera for low-angle elastic light scattering. *Review of Scientific Instruments* **1997,** 68, (6), 2265-2274.

4. Provencher, S. W., Contin - a general-purpose constrained regularization program for inverting noisy linear algebraic and integral-equations. *Computer Physics Communications* **1982,** 27, (3), 229-242.

5. Duggal, R.; Pasquali, M., Dynamics of individual single-walled carbon nanotubes in water by real-time visualization. *Physical Review Letters* **2006,** 96, (24), 246104.

6. Mansfield, M. L.; Douglas, J. F., Transport properties of rodlike particles. *Macromolecules* **2008,** 41, (14), 5422-5432.

7. Pecora, R., *Dynamic Light Scattering: Applications of Photon Correlation Spectroscopy.* Plenum Press, New York and London: 1985.

8. Wilkins, G. M. H.; Spicer, P. T.; Solomon, M. J., Colloidal System To Explore Structural and Dynamical Transitions in Rod Networks, Gels, and Glasses. *Langmuir* **2009,** 25, (16), 8951-8959.